Photocatalytic activity of nanostructured TiO_2/carbon-nanotube composites for near-UV to visible water treatment

Rita Ruivo Neves Marques

Dissertation presented for the Ph.D. degree in the

Doctoral Program in Chemical and Biological Engineering at the

Faculty of Engineering, University of Porto, Portugal

Supervisors: Joaquim Luís Bernardes Martins de Faria

Adrián Manuel Tavares da Silva

Cláudia Sofia Castro Gomes da Silva

LCM – Laboratory of Catalysis and Materials
Laboratório Associado LSRE/LCM
Departamento de Engenharia Química
Faculdade de Engenharia
Universidade do Porto
Portugal

May 2014

Sempre chegamos ao sítio aonde nos esperam.

[José Saramago]

Abstract

Scientific research is deeply committed to water remediation all over the world, with actual applications even at underdeveloped countries providing primary solutions with practical results. Heterogeneous photocatalysis has proven effective especially under real sunlight exposure conditions. Pure TiO_2 is the most commonly used photocatalyst although it does not absorb efficiently visible light, thus affording only scarce and partial UV usage of the sunlight radiation reaching earth surface.

The original contribution of this work to knowledge in the domain of heterogeneous photocatalysis technology consists on the development of TiO_2 based photocatalysts with enhanced response towards near-UV to visible radiation, using carbon nanotubes (CNTs), both single (SWCNTs) and multi-walled (MWCNTs), with their surfaces chemically modified by the inclusion of oxygen functionalities.

The resulting oxygen moieties promote the interaction of the carbon phase with the semiconductor TiO_2 phase, in particular by means of carboxylic acids and phenols, shifting the absorption edge of the metal oxide to the visible region of the spectrum. Controlled creation of oxygen groups in the surface of the CNTs was performed through hydrothermal oxidation with nitric acid and compared with the most commonly used boiling acid methods.

The degree of oxygen functionalization was analyzed by Temperature Programmed Desorption (TPD) and correlated through exponential functions with HNO_3 concentration. Along with the reaction temperature these two features are key to control the process. When the modification on the graphitic nanostructure of CNTs was analyzed by Raman spectroscopy a correlation with HNO_3 concentration was found, which was in a good agreement with TPD characterization. Comparison with the traditional boiling acid method shows that the hydrothermal approach is a competitive solution with equivalent level of surface functionalization using much lower amounts of oxidizing agent and reducing amorphous carbon deposits on the CNTs surface. However, boiling oxidation provided higher amounts of carboxylic acid functionalities, namely on MWCNTs surface, which are of particular interest for the synthesis of TiO_2 based composite materials for photocatalytic applications.

Photocatalytic oxidative degradation of aqueous caffeine, chosen as model compound for the assessment of catalytic activity, was studied by testing composites prepared with different loads of MWCNTs and different TiO_2 powders. The activity of the semiconductors could be enhanced in combination with the carbon phase, in particular with CNTs previously functionalized by nitric acid boiling oxidation bonded to the commercial TiO_2 purchased from Sigma-Aldrich (SA). Films prepared with these composites and deposited in thin glass slides were tested for the degradation of caffeine reaching higher photocatalytic activity than those prepared with the benchmark P25, representing a good promise for industrial applications.

A photocatalytic setup for pollutant abatement was built. The apparatus was developed, assembled and validated through optical characterization and photodegradation studies. Optical accessories like an optical window, a biconvex lens and optical filters were applied to provide optimum irradiation usage by focusing the light beam over the photocatalytic reactor in the desired range of wavelengths. An optimum configuration was defined based on caffeine photodegradation using suspensions of benchmark P25 (Evonik/Degussa). The current setup is set to study photocatalytic oxidation reactions in aqueous systems, either with suspensions or supported catalysts under different irradiating conditions with optimized usage of the emitted electromagnetic radiation in the near-UV to visible range.

Resumo

A pesquisa científica está profundamente comprometida com a questão do tratamento da água em todo o mundo, com aplicações reais que fornecem resultados práticos usando métodos muito rudimentares, sobretudo em países subdesenvolvidos. A fotocatálise heterogénea tem-se mostrado eficaz, nomeadamente em situações de forte exposição à luz solar. O dióxido de titânio (TiO_2) é o catalisador mais frequentemente utilizado neste processo apesar da sua baixa eficiência na absorção de radiação visível, conduzindo a um aproveitamento apenas parcial de uma pequena quantidade da radiação Ultra-Violeta (UV) que chega à superfície da terra, proveniente do Sol.

A contribuição original deste trabalho para o conhecimento no domínio da tecnologia associada à fotocatálise heterogénea consiste no desenvolvimento de fotocatalisadores à base de TiO_2 com elevada fotoeficiência sob ação da radiação electromagnética na gama do UV-próximo ao visível, usando para o efeito nanotubos de carbono (CNTs), quer de parede simples (SWCNT), quer de parede múltipla (MWCNT), sendo a sua superfície previamente modificada pela inclusão de grupos funcionais contendo oxigénio.

Estes grupos oxigenados promovem a interacção entre a fase de carbono e a fase do semicondutor TiO_2, em particular através dos grupos ácido carboxílico e fenólico, deslocando a banda de absorção do óxido metálico para a região do visível do espectro electromagnético. A geração controlada de grupos oxigenados na superfície dos CNTs foi realizada através de um método hidrotérmico usando ácido nítrico (HNO_3) e comparada com os métodos mais frequentemente utilizados que consistem na oxidação com ácido nítrico fervente.

O grau de funcionalização nos CNT foi analisado por desorção a temperatura programada (TPD) e correlacionado através de funções matemáticas exponenciais com a concentração de ácido nítrico. Juntamente com a temperatura de reacção, estes dois são parâmetros chave no controlo do processo. Foram também estabelecidas correlações matemáticas para a dependência do grau de modificação observado na estrutura grafítica dos CNT (analisada à escala nanométrica por

espectroscopia de Raman) em função da concentração de HNO_3. Os resultados obtidos mostraram ser concordantes com a caracterização obtida por TPD. Ao comparar com o método tradicional de oxidação com HNO_3 fervente, foi possível concluir que o tratamento hidrotérmico representa uma solução competitiva proporcionando um grau de funcionalização equivalente, mas faz uso de quantidades muito inferiores de agente oxidante, e reduz os depósitos de carbono amorfo na superfície dos CNTs. No entanto, a oxidação pelo método de HNO_3 fervente resulta numa maior densidade de grupos ácido carboxílico, nomeadamente na superfície de MWCNT, que são de particular interesse para a síntese de compósitos com TiO_2 para aplicações fotocatalíticas.

A cafeína foi escolhida como composto modelo para o estudo da actividade dos fotocatalisadores preparados. A sua degradação por oxidação fotocatalítica foi estudada com compósitos preparados com diferentes quantidades de MWCNT e TiO_2 de diferentes naturezas. A actividade dos semicondutores aumentou quando combinada com a fase de carbono, em particular quando foram usados CNTs previamente funcionalizados pelo método de HNO_3 fervente e um TiO_2 comercial (Sigma-Aldrich). Filmes destes compósitos foram preparados, depositados em lamelas de vidro, e testados na degradação da cafeína tendo-se observado uma eficiência fotocataítica superior àquela obtida com filmes do TiO_2 comercial de referência P25 (Evonik/Degussa), o que representa uma solução promissora para aplicações industriais.

Na fase final do trabalho foi construído um sistema fotocatalítico para a degradação de poluentes em fase líquida. O sistema foi desenvolvido, montado e validado através de caracterização óptica e de estudos de fotodegradação. Com o objectivo de fazer uma utilização optimizada da fonte luminosa na gama de radiação desejada, foram usados acessórios ópticos para minimizar os efeitos de dispersão e melhor dirigir o feixe de luz sobre o reactor fotocatalítico. A melhor configuração foi definida com base nos estudos de degradação da cafeína com suspensões do fotocatalisador comercial de referência P25. O sistema que foi desenvolvido está preparado para a realização de estudos de degradação fotocatalítica em sistemas aquosos, seja em suspensões ou com catalisadores suportados, sob diferentes condições de irradiação, com o uso optimizado da radiação electromagnética emitida na região do UV-visível.

Agradecimentos

A realização deste trabalho foi possível com a contribuição de várias pessoas a quem gostaria de agradecer.

Em especial ao meu orientador, o Professor Doutor Joaquim Faria, pela supervisão deste trabalho, pela ajuda na discussão científica e, algumas vezes, filosófica dos meus resultados. Também pelo exemplo de espírito de equipa e pela honesta amizade.

Aos meus co-orientadores, o Doutor Adrián Silva e a Doutora Cláudia Silva, pelo empenho incondicional no meu trabalho e por todos os ensinamentos humanos que vão muito para além da investigação científica e que tanto para ela contribuem.

Ao Professor Doutor José Luís Figueiredo por ter disponibilizado todos os recursos técnicos do Laboratório de Catálise e Materiais, do qual é director.

A todos os meus colegas de laboratório, em especial à Maria José Sampaio e ao Ricardo Segundo, com quem partilhei muito mais do que ciência nestes últimos anos. Também à Luísa Pastrana-Martínez, à Maria José Sampaio e à Raquel Rocha pela partilha de resultados complementares que ajudaram à discussão deste trabalho.

Ao Doutor Polycarpos Falaras do *Institute of Advanced Materials* em Atenas (NCSR Demokritos), pela colaboração na caracterização dos meus materiais e respectiva discussão científica.

Ao Doutor Goran Dražić, do *Jožef Stefan Institute* em Ljubljana, pela ajuda na realização das análises de HRTEM. Ao Professor Pedro Tavares do Departamento de Química da UTAD pela realização e ajuda na discussão de resultados das análises de XRD.

À Fundação para a Ciência e a Tecnologia pelo financiamento através da bolsa SFRH/BD/65425/2009.

Aos meus amigos, em especial à Ana Marques pela constância inabalável.

Finalmente, à minha mãe e ao meu pai, Judite e Fernando, ao meu irmão João e à minha avó Lucília. Por tudo, sempre!

Table of Contents

List of Figures

List of Tables

Glossary

Most Used Acronyms

AOP	Advanced Oxidation Process
BL	Biconvex lens
CB	Conduction Band
CCFs	Carboxylated Carbonaceous Fragments
CCVD	Catalytic Chemical Vapor Deposition
CNT	Carbon Nanotubes
DRIFT	Diffuse Reflectance Infra-Red Fourier Transformed
DRUV	Diffuse Reflectance UV-Vis
DSC	Differential Scanning calorimetry
FWCNT	Few-Walled Carbon Nanotubes
FWHM	Full With at Half Maximum
HOMO	Highest Occupied Molecular Orbit
HPLC	High Performance Liquid Chromatography
KM	Kubelka-Munk units
LP	Long pass optical filter
LUMO	Lowest Unoccupied Molecular Orbit
MWCNT	Multi-Walled Carbon Nanotubes
MS	Mass spectrometry
NIR	Near-Infrared
OM	Organic Molecule
OW	Optical window
PSD	Pore Size Distributions
QSDFT	Quenched Solid Density Functional Theory
R	Photo-reactor
SA	Sigma-Aldrich
SC	Semiconductor Catalyst

SEM	Scanning Electron Microscopy
SG	TiO_2 prepared by a Sol-Gel method
SWCNT	Single-Walled Carbon Nanotubes
TEM	Transmission Electron Microscopy
TGA	Thermogravimetric Analysis
TPD	Temperature Programmed Desorption
UV	Ultra Violet
UV-Vis	Ultra Violet Visible
VB	Valence Band
WL	Weight Loss
XRD	X-Ray Diffraction

Part I

Thesis Motivation

1 State of the art

Water treatment is an environmental issue well documented and vastly discussed throughout the scientific community in the European Union with very well defined objectives and targets to the next fifteen years. Semiconductor photocatalysis is a highly competitive Advance Oxidation Process for water remediation in spite of a limited industrial implementation. Titanium dioxide (TiO_2) has been widely used as photocatalyst, with Ultra-Violet photons with energy above 3.2 eV generating highly reactive surface excited electrons and holes which are responsible for the subsequent redox conversion of the organic pollutants through the photocatalytic process. However, considering that the solar spectrum at earth's surface (air mass 1.0) consists only of 3-6% of UV radiation, the natural band gap of neat TiO_2 represents a drawback when the sunlight is used in photocatalytic applications. Advances in the development of visible active photocatalysts by modifying TiO_2, namely with carbon nanotubes (CNTs), are significant. Modifications on the surface of CNTs, to improve the contact with the semiconductor phase, are achieved by the introduction of oxygen species and different methods have been tested at different conditions. Deep knowledge on the consequences of CNTs modification at molecular level is missing to better understand and develop a good TiO_2 photocatalyst based interphase interaction between the two components. Synergistic cooperation with the semiconductor phase by enhancing its absorption of light towards longer wavelengths has been reported for TiO_2/CNT photocatalysts. However, industrial implementation requires operation in continuous mode, which implies the usage of immobilized catalysts instead of the aqueous suspensions normally reported. The latter require further separation steps with increasing economic costs. The development of thin photocatalytic films with an optimized usage of sunlight for water treatment in a well-designed photocatalytic system operating in continuous mode is the final goal of the current research. To understand the motivation of this work, the goals will be framed in basis of an updated bibliography revision and the more important accounts outlined here.

1.1 Environmental concerns in Europe: Water pollution

Water pollution is one of the five main issues of European environmental concerns [1, 2]. Over the past 50 years, Europe has been affected by increasing conflicts due to ecological issues and human water requirements inherent to modern standards of living. In terms of water abstraction, the highest demands go for urban consumption (households and industry connected to the public water supply system), industry, agriculture and energy. Recently, the European Environment Agency (EEA) published *The European environment - state and outlook 2010* (SOER 2010) in which is reported the forecast of water demand to the year 2030 [3]. Concerning global water abstraction, agriculture currently accounts for about 3100 billion m^3 per year and, with no efficiency gains, will increase to 4500 billion m^3 by 2030. During this period, industrial abstraction is forecasted to nearly double and domestic abstraction to increase by 50%, as shown in Figure 1.1. Given the available supplies, the current water abstractions and those projected for 2030, accounting with the low historic rate of efficiency improvement in agricultural and industrial water use of ca. 1% per year, a huge deficit of 60% is estimated for the year 2030 in Europe.

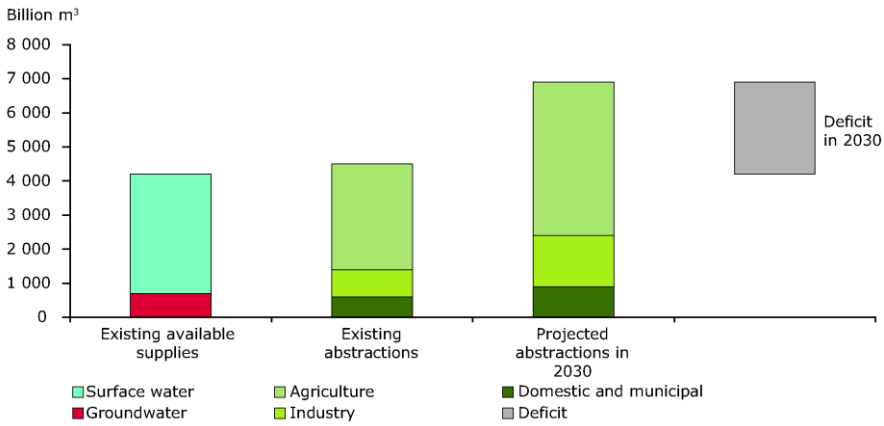

Figure 1.1 – Forecast of global water demand in Europe for the year 2030 [3].

Within the thematic 'freshwater quality' boarded in SOER 2010, one of the key messages goes for the expensiveness of removing pollution. In fact, remediation actions, in the context of urban environment, air pollution, land usage or water resources, requires large amounts of energy and chemicals resulting in further unavoidable generation of wastes. Controlling pollutants at source verily reduces the need for treatment by decreasing discharge to fresh waters. However, in a pragmatic

view, given the low improvement on efficient water use observed through the last years, the practical and imperative answer relies on efficient water remediation solutions minimizing energy and chemicals demands to make up for the disquieting abovementioned deficit, meanwhile aspiring for a progressively and more conscious usage and maintenance of water resources.

Large amount of water is consumed for industrial purposes and consequently high volumes of industrial wastewaters are produced containing a wide variety of harmful contaminants thus requiring complex wastewater treatments in sequential stages. From agriculture activities the key pollutants are nutrients, pesticides, sediment and fecal microbes whereas a high amount of pharmaceuticals and personal care products are detected in urban wastewaters. European water legislation started in 1975 by defining standards for rivers and lakes used for drinking water abstraction, and strict targets are nowadays defined on the discharge of harmful substances to water courses [1]. The EU Commission Services have recently launched a directive defining new Environmental Quality Standards (EQS) [4] which complemented with the 2012 Commission proposal on priority substances (COM(2011)876) and the First list of Priority substances Decision 2455/2001/EC support relevant information to develop legislation on the hazardous priority substances [5].

Biological routes in wastewater treatment are easily implemented with a low cost investment. However some drawbacks are inherent to these processes such as large production of sludge where certain contaminants are still present. It is also known that biological treatments are not suitable for wastewaters with a high organic load and that there are organic molecules, which are refractory to microorganisms activity. At variance, chemical treatments are able to solve many environmental scenarios by converting the primary pollutants into biodegradable organic compounds or by achieving complete mineralization depending of the desired level of depuration. Integration of biological and chemical treatments strongly depends on the wastewater characteristics, concentrations and desired outputs, representing an optimized solution for water remediation. Practical results achieved by combining Advanced Oxidation Processes (AOPs) with bioreactors are widely reported and recently reviewed [6-10]. Namely, within the most studied AOPs, semiconductor photocatalysis is a strong competitive technology operating at ambient temperature and pressure with the possibility of using natural sunlight as irradiation source which resumes a fairly clean technology giving answer to the abovementioned requirements to face EU difficulties in water remediation [11-14].

1.2 Semiconductor photocatalysis: an Advanced Oxidation Process for wastewater treatment

Advanced oxidation processes (AOPs) are chemical routes to oxidize organic or inorganic oxidizable species through a reaction mechanism involving the production of hydroxyl radicals ($HO^{\bullet}$). These oxidizing agents are characterized by their high reactivity and low selectivity, which are very competitive attributes to solve a wide range of pollution scenarios. AOPs comprise different possibilities like chemical oxidation (O_3, O_3/H_2O_2, Fenton), photochemical oxidation (UV/O_3, UV/H_2O_2) and photocatalytic oxidation processes (UV/TiO_2, photo-Fenton) [11, 15-18]. Heterogeneous photocatalysis is earning a growing relevance amongst several oxidation techniques, due to the last advances in light related technologies [19-21]. One of the main reasons is the ability of achieving complete mineralization of many organic pollutants at mild conditions of temperature and pressure with resource to a low energy-consuming water treatment technology. It has been successfully used on environmental applications with simulated and real effluents [22-28]. It is based on the photo-induced generation of electrical charges when a semiconductor material is illuminated with photons of energy equal to or greater than its characteristic band gap.

1.2.1 Reaction mechanism in heterogeneous photocatalysis

Since the semiconductor catalyst (SC) is irradiated ($h\nu$) with higher energy than that of the band gap, the electrons are excited from the valence band (VB, Highest Occupied Molecular Orbital - HOMO) to the conduction band (CB, Lowest Unoccupied Molecular Orbital - LUMO) generating electron-hole (e^-/h^+) pairs (eq. 1). These agents will get involved in a sequence of redox reactions producing highly oxidizing species like hydroxyl radicals ($HO^{\bullet}$) and superoxide radicals ($O_2^{\bullet -}$) [29, 30]. In aerated conditions, the molecular oxygen is adsorbed in the surface of the semiconductor acting as an electron acceptor (eq. 2) with formation of superoxide radicals. On the other hand, adsorbed water molecules and hydroxyl anions act as electron donors leading to the formation of hydroxyl radicals (eqs. 3 and 4).

$$\mathbf{SC} \xrightarrow{\mathbf{h\nu}} \mathbf{SC}(\mathbf{e_{CB}^-} + \mathbf{h_{VB}^+}) \quad (1)$$

$$\mathbf{SC}(\mathbf{e_{CB}^-}) + (\mathbf{O_2})_{\mathbf{ads}} \rightarrow \mathbf{SC} + (\mathbf{O_2^{\bullet -}}) \quad (2)$$

$$\mathbf{SC}(\mathbf{h_{VB}^+}) + (\mathbf{H_2O})_{\mathbf{ads}} \rightarrow \mathbf{SC} + (\mathbf{HO^{\bullet}})_{\mathbf{ads}} + (\mathbf{H^+})_{\mathbf{ads}} \quad (3)$$

$$\mathbf{SC}(\mathbf{h_{VB}^+}) + (\mathbf{OH^-})_{\mathbf{ads}} \rightarrow \mathbf{SC} + (\mathbf{HO^{\bullet}})_{\mathbf{ads}} \quad (4)$$

Once generated, the highly oxidizing $HO^{\bullet}$ radicals will react with the organic molecule (OM) adsorbed in the catalyst surface, which structure will breakdown into intermediate compounds that can be totally mineralized to CO_2 and H_2O (eq. 5).

$$\mathbf{OM_{ads}} + \mathbf{(HO^{\bullet})_{ads}} \rightarrow \mathbf{intermediates} \rightarrow \mathbf{CO_2} + \mathbf{H_2O} \quad (5)$$

Titanium dioxide has been the most studied semiconductor in photocatalysis. In 1921, C. Renz accounted for the first report with relation to this topic by describing the partial reduction of TiO_2 upon illumination using sunlight in the presence of glycerol [31].

1.2.2 Titanium dioxide photocatalyst

Titanium dioxide (TiO_2) has been widely used as photocatalyst, due to its chemical stability, relatively low toxicity and affordable cost or easy synthesis, and because this material is a very powerful oxidant when excited under Ultra Violet (UV) or near-UV to Visible (Vis) irradiation [16, 18, 29, 31-36]. Photons with energy above 3.2 eV generate highly reactive surface excited electrons and holes which are responsible for the subsequent oxidation of the organic pollutants through the previously described photocatalytic process by the formation of the hydroxyl and superoxide radicals or by direct oxidation with photogenerated holes [34]. Photocatalytically active TiO_2 powders can be easily synthesized by means of the sol-gel method, materials with distinct properties being obtained by varying the synthesis conditions [33, 35, 37-39]. This preparation technique involves the use of a metal alkoxide as a precursor, which is dissolved in an alcohol. The alkoxide is hydrolyzed and then the condensation of the polymeric chains takes place. The resulting gel is allowed to dry under ambient or supercritical conditions forming a xerogel or an aerogel, respectively. Further calcination helps to eliminate the remaining solvent and, at different calcination temperatures, distinct crystalline phases can be attained. Very homogeneous materials are obtained using the sol-gel synthesis procedure and the possibility to include other phases in the TiO_2 matrix is an additional advantage [40-45].

The most reported three polymorphs of TiO_2 that can be found in nature are anatase, rutile and brookite, which crystal structures are represented in **Error! Reference source not found.**. The commercial TiO_2 most used in photocatalytic applications is AEROXIDE® TiO_2 P25 (Evonik Degussa Corporation) which is constituted by a mixture of anatase and rutile crystalline phases in a 4:1 mass ratio plus a certain

amount of amorphous TiO_2 [46]. The photoefficiency of a certain material is attributed not just to the crystalline phase composition. It must be pointed out that thin films of amorphous TiO_2 have also shown to be photocatalytic active [47]. Other characteristics like particle size are also relevant in the catalytic performance [32, 37, 38, 48, 49].

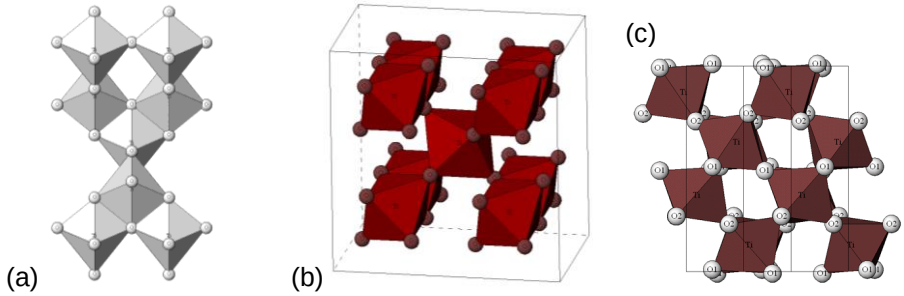

Figure 1.2 – Crystal structures of anatase (a) rutile (b) and brookite (c). (images available in Crystal Structure Gallery, National Institute of Advanced Industrial Science and Technology (AIST) [50]).

Industrial implementation of solar-driven photocatalytic processes is dependent on how efficiently the photocatalysts can use the solar light. The major challenge in this field is to increase the spectral sensitivity of photocatalysts to visible light, which is the largest fraction of the solar irradiation spectrum. Due to the characteristic bandgap energy of bare TiO_2 as being 3.2 eV, the electronic transitions needed to generate the e^-/h^+ pairs can only be promoted when this material is irradiated with UV light of high energy. The UV region of the electromagnetic spectrum covers wavelengths from 100 to 400 nm and is divided into three bands: UVC (100-280 nm), UVB (280-315 nm) and UVA (315-400 nm) [51]. UV radiation is merely a small fraction of the total light at the Earth's surface, mainly composed of UVA with a small UVB component and no UVC because, as sunlight passes through the atmosphere, all UVC and approximately 90% of UVB radiation are absorbed by ozone, water vapour, oxygen and carbon dioxide [52, 53]. For visible irradiance there is no agreement on the limits for its range. Some scientific sources confine it from 380 to 760 nm and others from 400 to 760 nm. Near-UV is referred to wavelengths from 300 to 400 nm [51]. The range of near-UV to visible radiation (300-760 nm) is commonly used in photocatalytic studies to simulate solar driven photocatalysis. In conclusion, the natural bandgap of neat TiO_2 represents a drawback in solar light-driven photocatalytic applications [54]. The development of TiO_2-based catalysts with an overall narrower bandgap, allowing the use of longer wavelengths to initiate the

reaction, is thus a current issue of research aiming at the possible reduction of the operating costs by better exploiting sunlight.

1.3 Improving the photo-efficiency of the semiconductor TiO_2

In order to extend light absorption towards wavelengths in the visible range, TiO_2 has been modified following different approaches which are recently revised in the literature [19, 55-57]. Modifications are carried out namely by doping or loading the TiO_2 structure with other elements, either metal or non-metal species [23, 57-65], by dye-sensitization [57], by forming composites with other oxides [66] or with different carbon phases like activated carbons, graphene, fullerenes or carbon nanotubes [19, 56, 67-71].

The photo-efficiency of a certain material also generally depends on crystalline phase composition, particle size, surface area, particle morphology and distribution of hydroxyl groups [48, 49, 72].

Recently, high emphasis has been given to synergies created between TiO_2 and carbon materials, in particular with carbon nanotubes (CNTs) upon photo-excitation of the resulting composite catalysts [19, 56]. The effect caused by the introduction of carbon nanotubes in the photo-activation mechanism of TiO_2/CNT composites is further discussed in Section 1.3.1.

1.3.1 TiO_2/CNT composites and photo-activation mechanism

Composites based on TiO_2 and CNTs are reported to possess enhanced photocatalytic response under both UV and visible light irradiation for the oxidative degradation of many different organic pollutants [42, 56, 71, 73-76]. Due to their electric conductivity, CNTs can promote e^- diffusion, reduce e^-/h^+ recombination and act as photosensitizers and dispersing agents for TiO_2 particles, being possible to take advantage of CNTs properties to prepare more efficient photocatalysts. However, this is not always the case, since it has been found that for the molecules with stronger electron-withdrawing (deactivating) groups, such as 4-nitrophenol, the combination of CNTs with TiO_2 is not favourable for the photocatalytic degradation process [76].

For instance, Yao et al. [74] who have studied the photocatalytic degradation of phenol with TiO_2/CNT powders concluded that the composites prepared with 100 nm

anatase and single-walled CNTs exhibited enhanced and selective photocatalytic oxidation of phenol in comparison to pure anatase or P25 particles. The results are explained based on an optimal arrangement between phases for a weight ratio of CNTs to TiO_2 of ca. 20%, stabilizing charge separation and reducing charge recombination, this ratio being identified as optimal in many other works with TiO_2/CNT [56, 71, 75, 76].

In fact, TiO_2/CNTs are believed to take benefit of the CNTs capacity of absorbing visible light to initiate the reaction mechanism, leading to the generation of the so reactive oxidant species [42, 77, 78]. The enhanced response in the visible range of the spectrum for these composites is represented in Figure 1.3.

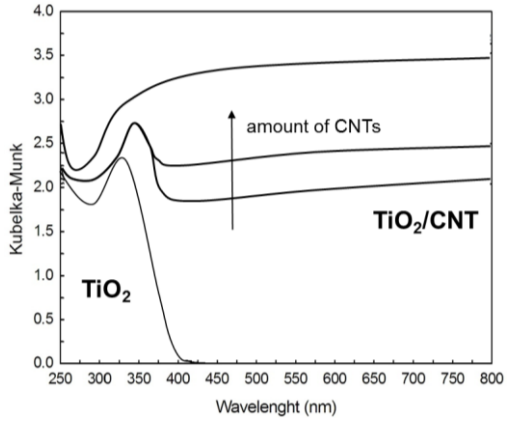

Figure 1.3 – TiO_2 light absorption enhancement when in composite form with CNTs.

Moreover than the proved shift towards longer wavelengths it is reported that the light absorption increases with the amount of CNTs in the respective composite [42, 76].

Two of the proposed mechanisms described in literature that are believed to operate in a sensitized photoreaction with TiO_2/CNT composites are partially represented in the schemes of Figure 1.4 and Figure 1.5. It must be noticed that the schemes do not show all the reactions involved, but just intend to illustrate the generation of the superoxide (a) and hydroxyl (b) oxidizing agents.

The mechanism represented in Figure 1.4 and resumed in eqs. 5-9 begins with the absorption of visible light by CNTs, with the excited electrons being transferred to the CB of TiO_2. If the diffusion of the e^-/h^+ pairs to the photocatalyst surface is more effective than

e^-/h^+ recombination and molecular oxygen present in the reaction medium is abundant, it will be reduced by the excited e^- at the surface of TiO_2 to form the superoxide radical.

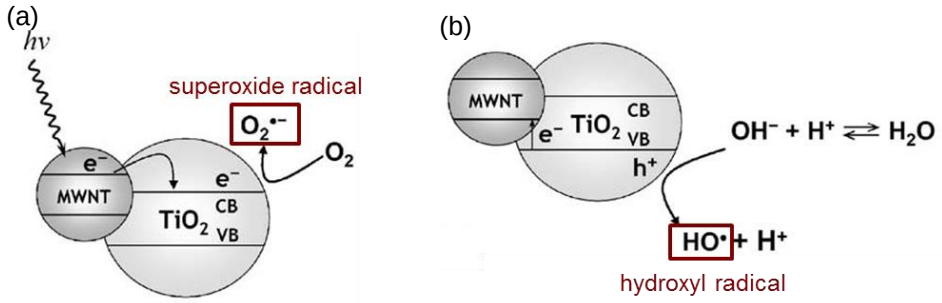

Figure 1.4 – CNTs acting as photosensitizers in the composite catalyst: (a) following photon absorption, an electron is injected into the CB of TiO_2 semiconductor; (b) the electron is back-transferred to CNTs with the formation of a hole in the VB of TiO_2 semiconductor and reduction of the so formed hole by adsorbed OH^- (adapted from [42]).

On the other hand, electrons on the VB of TiO_2 can migrate to the surface of CNTs generating positive holes, which will oxidize the hydroxide anions to form hydroxyl radicals. The organic molecules (OM) will be then decomposed by radicals attack. The main steps involved are summarized in the following equations:

$$\mathbf{TiO_2/CNT} \xrightarrow{\mathbf{h\nu}} \mathbf{TiO_2/CNT(e^-_{CB} + h^+_{VB})} \quad (5)$$

$$\mathbf{TiO_2/CNT(e^-_{CB} + h^+_{VB})} \rightarrow \mathbf{TiO_2(e^-_{CB})/CNT(h^+_{VB})} \quad (6)$$

$$\mathbf{TiO_2(e^-_{CB})} + \mathbf{(O_2)_{ads}} \rightarrow \mathbf{TiO_2} + \mathbf{(O_2^{\bullet-})} \quad (7)$$

$$\mathbf{TiO_2(h^+_{VB})} + \mathbf{(OH^-)_{ads}} \rightarrow \mathbf{TiO_2} + \mathbf{(HO^\bullet)_{ads}} \quad (8)$$

$$\mathbf{(HO^\bullet)_{ads}} + \mathbf{OM} \rightarrow \mathbf{intermediates} \rightarrow \mathbf{CO_2} + \mathbf{(H_2O)_{ads}} \quad (9)$$

On the other hand, if the irradiated light is of enough energy to be absorbed by TiO_2, the electronic transitions will be promoted and the excited electrons will migrate to the CB generating h^+ in the VB. The formation of the hydroxyl radicals can occur either due to h^+

reduction by the adsorbed water or by OH^- oxidation, as shown in Figure 1.5. In the same way, the so-formed oxidizing agents will initiate the photo-degradation of organic pollutants through sequential redox reactions.

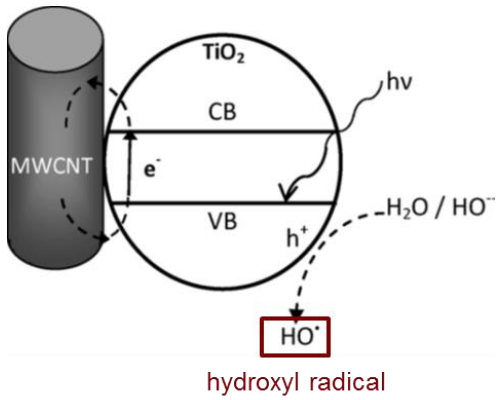

Figure 1.5 – Simplified representation of the interaction between TiO_2 and the CNTs and the way $HO^{\bullet}$ may be formed following e^-/h^+ pair generation (adapted from [77]).

These composites are usually used in powder form as slurries which is a very common procedure when compared with systems implementing immobilized catalysts, due to the large amount of catalyst per reactor volume in the first case, minimizing mass transfer limitations.

However, slurry operation at industrial scale requires final separation of the catalyst incurring in additional costs and precluding the possibility of reaction in continuous mode. To surpass this drawback, thin films have been developed to operate in adequate photo-reactors overcoming the disadvantage of the post separation step for suspensions, but mostly TiO_2 films are reported with very scarce information on the development of TiO_2/CNT composite films with enhanced photo-activity for water remediation [73, 79-91]. At laboratorial scale, operating with catalysts in powder form is useful for screening experiments with the aim to select the most efficient materials to be further immobilized on support surfaces. Different techniques have been applied to prepare photocatalytic films, such as spin coating, dip coating, liquid phase deposition or doctor blade [73, 82, 83, 86-88, 92-94]. Doctor blade method is a very simple technique for mass production of thin films with good uniformity and reproducible properties [95] which has been recently applied to prepare TiO_2/CNT composites for photocatalytic applications [73, 83].

At the present moment, it is of high relevance the development of TiO_2/CNT composite films with an intimate interaction between the semiconductor and the carbon phase, for achieving high yields of charge separation and ensuring efficient charge carriers interchange upon photo-excitation with near-UV to visible radiation. The ultimate goal is the development of efficient catalysts for solar-driven applications at industrial scale. Having a deep knowledge about the TiO_2/CNT interphase interaction is of great importance and has been scarcely studied. In most cases the photocatalytic efficiencies are assessed based on empirical observations rather than on well-established scientific arguments.

The synergy commonly observed between TiO_2 and CNTs must be object of comprehensive studies by understanding in detail CNTs properties and the possible modifications to better achieve a consistent interphase resulting in photocatalytic composites with high efficiency response under near-UV to visible light irradiation.

1.3.2 Carbon nanotubes and surface chemistry modification

Carbon nanotubes are structures of particular interest due to their unique properties, such as high mechanical resistance and exceptional thermal stability under oxidizing atmosphere conditions [96, 97]. Ideal CNTs are made of one (Single-Walled Carbon Nanotubes, SWCNTs) or more (Multi-Walled Carbon Nanotubes, MWCNTs) graphene sheets with hexagonal display of sp^2 hybridized carbon atoms. Depending on the way in which the graphene layers are rolled up, CNTs have either metallic or semi-conductive properties [98]. The successful synthesis of MWCNTs by Iijima in 1991 [99] opened a prolific domain of new research. Rapidly was realized that single-shell structures were required to better understand their properties and two years later the synthesis of SWCNTs by arc-discharge was reported by both Iijima and Ichihashi [100] and Bethune et al. [101] . A few years later in 1996, Thess et al. produced metallic and highly uniform SWCNTs in yields of more than 70 % by condensation of a laser-vaporized carbon–nickel–cobalt mixture [102]. Recent developments in the mass production of MWCNTs, which has gradually evolved from the bench to the large-scale manufacturing, rendered them the material of choice for large volume applications, in contrast to the prototype SWCNTs, whose scale-up has lagged behind because of their significantly higher cost [103-109]. In particular, commercial MWCNTs are mostly produced by catalytic chemical vapor deposition (CCVD) for large scale production [110, 111], whose structural properties may be significantly impaired by the soot-like amorphous carbon emerging as pyrolysis by-

product [112] and inherent defects in the graphitic tube shells due to the relatively low growth temperature [113].

CNTs have been widely used in general catalytic applications [114] and numerous studies have been oriented to their use as support materials in catalysis, namely in hydrogenation reactions, hydrocarbon decomposition or development of fuel cell electrocatalysts [97, 115]. Several other applications have been reviewed encompassing a broad range of potential products from conductive, high-strength composites and lithium-ion battery electrodes to energy storage, sensors and field emission displays [115-118].

Several properties, which were studied for ideal CNTs, depending mainly on their diameter and chirality, are also strongly affected by the presence of defects such as pentagons, heptagons, vacancies or dopant species [119]. Potential applications have been investigated by introducing defects and modifying the surface chemistry of CNTs [115, 120-124]. Depending on the required application, several chemical agents can be hosted at the surface of CNTs like alkali metals [125-127], salen complexes [128, 129], amines to form polyaniline composites [130, 131], gold nanoparticles for sensitive determination of nitrite [132] or biomedical applications [133] and S-containing groups to improve the catalytic performance of CNTs on the oxidation of organic pollutants [134]. Nevertheless, since CNTs are considered as almost inert substrates, they are previously subjected to oxidizing treatments and, depending on the conditions and the oxidizing agents used, is possible to obtain modifications on the surface chemistry and in the structural integrity at distinct levels [130, 134-144]. Despite the marked progress in purification of CNTs [145], controlled functionalization of their hydrophobic and chemically inert surface remains a major challenge for practical deployment, especially for MWCNTs that, being on the verge of commercialization, attract particular interest [109].

To accomplish an effective interaction between TiO_2 and CNTs, modifications on the surface chemistry of the carbon phase are required. This is usually achieved through chemical treatments, often by using nitric acid (HNO_3) resulting in the introduction of surface groups like carboxylic and phenolic functionalities, which are believed to participate in the covalent anchorage of TiO_2 [146].

The chemical surface modification of carbon materials using nitric acid (HNO_3) is not a recent topic [147-155]. It has been performed over distinct carbon materials like activated carbons [153, 154], carbon xerogels [156-158], graphite [159] or ordered mesoporous carbons [160, 161]. Liquid phase oxidation with HNO_3 is the most

prevalent process for the purification of as-grown CNTs by selectively removing amorphous carbon and residual metal catalyst impurities [114, 145, 162], as a pre-treatment to provide CNTs with a homogeneous surface [163] and has been studied for the selective removal of small diameter metallic SWCNTs [164, 165]. Functionalization through HNO_3 oxidation results on the opening of the tube caps and the modification of the surface chemistry of the CNTs by the covalent attachment of oxygen-containing groups, i.e. carboxylic acids and anhydrides, phenols, carbonyl quinones, and lactones, preferentially takes place at the tube ends and CNTs side-walls [121, 166-168], following a sequential oxidation path that sets out at the highly reactive defect sites of CNTs [169]. These hydrophilic surface groups may drastically promote the CNTs' dispersability in various solvents and their colloidal stability [170-172], enhance the CNTs' interfacial coupling with polymer matrices for the development of advanced nanocomposites [173], while simultaneously serving as anchoring sites for further chemical functionalization and processing [174], resulting in much higher reactive substrates than the pristine CNTs.

HNO_3 treatments have been extensively used at very high concentrations using boiling methods [135, 155, 175], which are very efficient for the introduction of a high density of oxygen-containing groups. However, severe degradation effects, accompany the results especially for SWCNTs, including material's loss, tube shortening as well as the formation of structural defects and carbonaceous debris [155, 162, 164, 176]. The formation of exfoliated carboxylated carbonaceous fragments (CCFs) via the nitric acid over-oxidation of SWCNTs and subsequent base washing, arose considerable concerns as to the process effectiveness, which could undermine the nanotubes' dispersability in different host matrices [177-182]. Due to the occurrence of own SWCNT's consumption, particular attention has been given to the binding of the created oxygen functionalities to the CCFs amorphous structures [177-180]. Base washing or more severe oxidant conditions can clean CNT's surface from CCFs but there are still a significant fraction of oxygen functionalities that remains directly covalently bonded to the CNT's atoms. Although MWCNTs were found to be more resistant to oxidation than SWCNTs [178], similar detrimental effects including the formation of oxidation debris by nitric acid reflux were also identified [135, 138, 183-186], which could largely compromise their performance for example in catalytic [187] or electrochemical applications [188]. The underlying reaction mechanism resulting from the interplay of the various abovementioned effects has been the subject of several investigations [99, 162, 164, 170, 177-180, 189-192].

Even though significant insights on the diverse HNO_3 oxidation pathways have been recently provided by the combination of thorough experimental and theoretical investigations [169], kinetic control of the CNTs surface functionalization by the oxidation duration and/or reaction temperature remains a challenging task [178], justifying the high interest in the development of controllable purification/functionalization processes of CNTs [112, 193, 194]. It is worth mentioning that usually boiling methods are not applied in a controlled mode, since there are no correlations between the degree of functionalization and the conditions used. Given the relevance of the functionalization step in the preparation of different carbon based materials for numerous applications, the development of methods for the controlled modification of their surface chemistry is required.

To probe the functional groups created at CNTs surface different techniques have been performed, namely acid base titration, X-ray photoelectron spectroscopy, infrared and Raman vibrational spectroscopies, temperature programmed desorption (TPD), thermogravimetric analysis (TGA) together with electron microscopy [195, 196], however an accurate characterization based on type and amount of surface groups cannot be provided by single spectroscopic or microscopic investigations. As reported earlier in literature, with respect to the mechanism of the oxidation process over SWCNTs, sequential stages are proposed involving defect generating and defect consuming steps [162], which highlight the need of detailed investigations at atomic scale concerning structure and electronic surface modifications. In particular, resonance Raman spectroscopy has afforded quantitative analysis of stacking order, finite crystallite size and defect structure of nanographitic materials unveiling unique information on their electronic and vibrational properties hardly accessible by other techniques, which establishes a highly competitive position as a powerful tool for the characterization of CNTs [197-200]. Despite the widespread use of Raman spectroscopy on the characterization of functionalized SWCNTs through the activation of defect induced Raman modes [201, 202] and the high sensitivity of the first order phonon modes of SWCNTs to charge transfer [190, 203], complementary experimental data on the defect density and textural characterization is missing [204].

1.4 Objectives and thesis outline

The following topics are recognized as of outmost importance and there are currently under intense research and discussion: i) controlled functionalization of CNTs for the introduction of oxygen functionalities on their surface; ii) deep knowledge on the

subsequent structural modifications to better chose the adequate method for each carbon nanotube structure; iii) characterization and quality development of the interphase interaction in TiO_2/CNT composites; iv) progress in the synthesis of TiO_2/CNT films and their photocatalytic activity assessment in comparable conditions with those performed for the respective powders.

The present work aims at increasing the knowledge on the development of TiO_2 based photocatalytic composites with improved light response in the near-UV to visible range of the electromagnetic spectrum for water remediation. The selected approach consisted in the combination of TiO_2 with CNTs with an adequate modified surface with oxygen functionalities, aiming at the formation of improved bonding between both phases. The designed materials should be able to promote the oxidation of emerging pollutants or priority substances defined by the EU Commission Services, under solar radiation in continuous mode at industrial scale.

The manuscript is organized in VI Parts divided by 9 Chapters. This current introductory revision described the thesis motivation and corresponds to Part I as being the state of the art of the topic. Part II includes Chapters 2 and 3 and consists on the description of the Experimental Setups and Analytical techniques used to obtain the experimental results. Part III includes Chapters 4 and 5 where the chemical surface modification of different carbon nanotubes structures is carried out and deeply characterized. The photoactivity of the developed and characterized TiO_2/CNT composites is discussed on the Chapter 6, which composes Part IV. A customized photocatalytic setup was assembled for the assessment of photocatalytic composites and corresponds to Chapter 7 on Part V. Part VI includes Chapters 8 and 9 with the final remarks and future work, respectively.

The bibliography revision relative to Chapters 4 to 7 is condensed in Part I. Before each particular Chapter a brief note is given to frame the developed achievements within that part of the work. Inside each Chapter the results and discussion are firstly presented. Complementary experimental details are given at the end of each chapter in order to provide for the specifics, which are beyond the general descriptions given within the Chapters 2 and 3 of Part II Experimental Section.

In brief, Chapter 4 is dedicated to the controlled modification of the surface chemistry of SWCNTs and identification of the desired generated oxygen functionalities together with a detailed characterization of the following structural modifications due to the applied hydrothermal HNO_3 oxidation.

Chapter 5 stands for the modification of the surface chemistry of MWCNT structures through the same previously mentioned hydrothermal methodology and compared with the results achieved for the SWCNTs treated on Chapter 4 and with other MWCNT nanostructures with different diameter and length. Comparison with the common HNO_3 boiling acid method is discussed.

In Chapter 6, several TiO_2/CNT are characterized after being prepared based on different TiO_2 powders with one of them synthesized in the laboratory. Pristine and previously modified CNTs were used, with high amounts of identified and quantified oxygen functionalities. The photocatalysts were tested for the oxidative degradation of the emerging pollutant caffeine as suspensions in a photoimmersion reactor. Selected composites were further tested in a small cylindrical photo-reactor deposited in thin glass slides.

Finally, in Chapter 7 a photocatalytic system was assembled to perform consistent experiments on water treatment studies with catalysts either in powder or film form. The system was well characterized and improved with optical accessories for a better usage of the light source and to create different spectral conditions for complete studies. Characterization was validated with photocatalytic experimental results and optimal conditions are proposed.

The thesis culminates with final remarks in Chapter 8 with an integrated view of the obtained results and with some guidelines suggested as future work encouraging the progress ahead to briefly achieve an effective and real scientific response for the urgent need of water treatment at industrial scale through heterogeneous photocatalysis with the promising TiO_2/CNT composites, facing the well-known concerns in nowadays Europe.

1.5 References

[1] Introduction to the new EU Water Framework Directive. 25/04/2014 [cited 10/05/2014]; Available from: http://ec.europa.eu/environment/water/water-framework/info/intro_en.htm

[2] European waters — assessment of status and pressures. Copenhagen: European Environment Agency (EEA); 2012.

[3] The European environment — state and outlook 2010 (SOER 2010). Copenhagen: European Environment Agency (EEA); 2010.

[4] Directive 2008/105/EC of the European Parliament and of the Council. Official Journal of the European Union: Strasbourg 2008.

[5] Priority substances supporting information and documentation. 25/04/2014 [cited 10/05/2014]; Available from: http://ec.europa.eu/environment/water/water-dangersub/lib_pri_substances.htm

[6] Scott JP, Ollis DF. Integration of chemical and biological oxidation processes for water treatment: review and recommendations. Environ Prog. 1995; 14 (2):88-103.

[7] Tabrizi GB, Mehrvar M. Integration of advanced oxidation technologies and biological processes: Recent developments, trends, and advances. J Environ Sci Health Part A-Toxic/Hazard Subst Environ Eng. 2004; 39 (11-12):3029-81.

[8] Oller I, Malato S, Sánchez-Pérez JA. Combination of Advanced Oxidation Processes and biological treatments for wastewater decontamination—A review. Sci Total Environ. 2011; 409 (20):4141-66.

[9] Augugliaro V, Litter M, Palmisano L, Soria J. The combination of heterogeneous photocatalysis with chemical and physical operations: A tool for improving the photoprocess performance. J Photochem Photobiol C-Photochem Rev. 2006; 7 (4):127-44.

[10] Homem V, Santos L. Degradation and removal methods of antibiotics from aqueous matrices – A review. J Environ Manage. 2011; 92 (10):2304-47.

[11] Sin JC, Lam SM, Mohamed AR, Lee KT. Degrading endocrine disrupting chemicals from wastewater by tiO 2 photocatalysis: A review. Int J Photoenergy. 2012; 2012.

[12] Ahmed S, Rasul MG, Martens WN, Brown R, Hashib MA. Heterogeneous photocatalytic degradation of phenols in wastewater: A review on current status and developments. Desalination. 2010; 261 (1-2):3-18.

[13] Chiron S, Fernandez-Alba A, Rodriguez A, Garcia-Calvo E. Pesticide chemical oxidation: State-of-the-art. Water Res. 2000; 34 (2):366-77.

[14] Malato S, Fernández-Ibáñez P, Maldonado MI, Blanco J, Gernjak W. Decontamination and disinfection of water by solar photocatalysis: Recent overview and trends. Catal Today. 2009; 147 (1):1-59.

[15] Chong MN, Jin B, Chow CWK, Saint C. Recent developments in photocatalytic water treatment technology: A review. Water Res. 2010; 44 (10):2997-3027.

[16] Gogate PR, Pandit AB. A review of imperative technologies for wastewater treatment I: Oxidation technologies at ambient conditions. Adv Environ Res. 2004; 8 (3-4):501-51.

[17] Gogate PR, Pandit AB. A review of imperative technologies for wastewater treatment II: Hybrid methods. Adv Environ Res. 2004; 8 (3-4):553-97.

[18] Andreozzi R, Caprio V, Insola A, Marotta R. Advanced oxidation processes (AOP) for water purification and recovery. Catal Today. 1999; 53 (1):51-9.

[19] Di Paola A, García-López E, Marcì G, Palmisano L. A survey of photocatalytic materials for environmental remediation. J Hazard Mater. 2012; 211-212:3-29.

[20] Prihod'ko RV, Soboleva NM. Photocatalysis: Oxidative processes in water treatment. Journal of Chemistry. 2013; Article number 168701.

[21] Ohtani B. Revisiting the fundamental physical chemistry in heterogeneous photocatalysis: Its thermodynamics and kinetics. Phys Chem Chem Phys. 2014; 16 (5):1788-97.

[22] Silva AMT, Nouli E, Xekoukoulotakis NP, Mantzavinos D. Effect of key operating parameters on phenols degradation during H_2O_2-assisted TiO_2 photocatalytic treatment of simulated and actual olive mill wastewaters. Appl Catal B-Environ. 2007; 73 (1-2):11-22.

[23] Silva AMT, Silva CG, Dražić G, Faria JL. Ce-doped TiO_2 for photocatalytic degradation of chlorophenol. Catal Today. 2009; 144 (1-2):13-8.

[24] Silva AMT, Nouli E, Carmo-Apolinário AC, Xekoukoulotakis NP, Mantzavinos D. Sonophotocatalytic/H_2O_2 degradation of phenolic compounds in agro-industrial effluents. Catal Today. 2007; 124 (3-4):232-9.

[25] Kositzi M, Antoniadis A, Poulios I, Kiridis I, Malato S. Solar photocatalytic treatment of simulated dyestuff effluents. Sol Energy. 2004; 77 (5):591-600.

[26] Jelic A, Michael I, Achilleos A, Hapeshi E, Lambropoulou D, Perez S, et al. Transformation products and reaction pathways of carbamazepine during photocatalytic and sonophotocatalytic treatment. J Hazard Mater. 2013; 263:177-86.

[27] Arslan I, Balcioğlu IA, Bahnemann DW. Advanced chemical oxidation of reactive dyes in simulated dyehouse effluents by ferrioxalate-Fenton/UV-A and TiO2/UV-A processes. Dyes Pigment. 2000; 47 (3):207-18.

[28] Ali AH, Kapoor S, Kansal SK. Studies on the photocatalytic decolorization of pararosanilne chloride dye and its simulated dyebath effluent. Desalin Water Treat. 2011; 25 (1-3):268-75.

[29] Faria JL. The heterogeneous photocatalytic process. In: Pereira MM, Figueiredo JL, Faria JL, eds. Catalysis from Theory to Application - An Integrated Course. Coimbra: Coimbra University Press 2008, p. 479-94.

[30] Herrmann JM. Photocatalysis fundamentals revisited to avoid several misconceptions. Appl Catal B-Environ. 2010; 99 (3-4):461-8.

[31] Fujishima A, Zhang X, Tryk DA. TiO2 photocatalysis and related surface phenomena. Surf Sci Rep. 2008; 63 (12):515-82.

[32] Silva CG, Faria JL. Effect of key operational parameters on the photocatalytic oxidation of phenol by nanocrystalline sol-gel TiO_2 under UV irradiation. J Mol Catal A: Chem. 2009; 305 (1-2):147-54.

[33] MacWan DP, Dave PN, Chaturvedi S. A review on nano-TiO 2 sol-gel type syntheses and its applications. J Mater Sci. 2011; 46 (11):3669-86.

[34] Herrmann JM. Heterogeneous photocatalysis: an emerging discipline involving multiphase systems. Catal Today. 1995; 24 (1–2):157-64.

[35] Isley SL, Penn RL. Titanium Dioxide Nanoparticles: Effect of Sol−Gel pH on Phase Composition, Particle Size, and Particle Growth Mechanism. J Phys Chem C. 2008; 112 (12):4469-74.

[36] Fujishima A, Zhang X, Tryk DA. Heterogeneous photocatalysis: From water photolysis to applications in environmental cleanup. Int J Hydrog Energy. 2007; 32 (14):2664-72.

[37] Arconada N, Durán A, Suárez S, Portela R, Coronado JM, Sánchez B, et al. Synthesis and photocatalytic properties of dense and porous TiO2-anatase thin films prepared by sol-gel. Appl Catal B-Environ. 2009; 86 (1-2):1-7.

[38] Kolen'ko YV, Garshev AV, Churagulov BR, Boujday S, Portes P, Colbeau-Justin C. Photocatalytic activity of sol–gel derived titania converted into nanocrystalline powders by supercritical drying. J Photochem Photobiol A-Chem. 2005; 172 (1):19-26.

[39] Montoya IA, Viveros T, Domínguez JM, Canales LA, Schifter I. On the effects of the sol-gel synthesis parameters on textural and structural characteristics of TiO2. Catal Lett. 1992; 15 (1-2):207-17.

[40] Jang JS, Ji SM, Bae SW, Son HC, Lee JS. Optimization of CdS/TiO_2 nano-bulk composite photocatalysts for hydrogen production from Na_2S/Na_2SO_3 aqueous electrolyte solution under visible light (λ ≥ 420 nm). J Photochem Photobiol A-Chem. 2007; 188 (1):112-9.

[41] Poznyak SK, Talapin DV, Kulak AI. Structural, optical, and photoelectrochemical properties of nanocrystalline TiO_2-In_2O_3 composite solids and films prepared by sol-gel method. J Phys Chem B. 2001; 105 (21):4816-23.

[42] Wang W, Serp P, Kalck P, Faria JL. Visible light photodegradation of phenol on MWNT-TiO_2 composite catalysts prepared by a modified sol-gel method. J Mol Catal A: Chem. 2005; 235 (1-2):194-9.

[43] Wang W, Silva CG, Faria JL. Photocatalytic degradation of Chromotrope 2R using nanocrystalline TiO_2/activated-carbon composite catalysts. Appl Catal B-Environ. 2007; 70 (1-4):470-8.

[44] Yoshida M, Prasad PN. Sol−Gel-Processed SiO2/TiO2/Poly(vinylpyrrolidone) Composite Materials for Optical Waveguides. Chem Mater. 1996; 8 (1):235-41.

[45] Abdelaal MY, Mohamed RM. Novel Pd/TiO2 nanocomposite prepared by modified sol-gel method for photocatalytic degradation of methylene blue dye under visible light irradiation. J Alloys Compd. 2013; 576:201-7.

[46] Ohtani B, Prieto-Mahaney OO, Li D, Abe R. What is Degussa (Evonic) P25? Crystalline composition analysis, reconstruction from isolated pure particles and photocatalytic activity test. J Photochem Photobiol A-Chem. 2010; 216 (2-3):179-82.

[47] Eufinger K, Poelman D, Poelman H, De Gryse R, Marin GB. Photocatalytic activity of dc magnetron sputter deposited amorphous TiO_2 thin films. Appl Surf Sci. 2007; 254 (1):148-52.

[48] Zhang Z, Wang C-C, Zakaria R, Ying JY. Role of Particle Size in Nanocrystalline TiO2-Based Photocatalysts. J Phys Chem B. 1998; 102 (52):10871-8.

[49] Silva CG, Faria JL. Anatase vs.rutile efficiency on the photocatalytic degradation of clofibric acid under near UV to visible irradiation. Photochem Photobiol Sci. 2009; 8 (5):705-11.

[50] Crystal Structure Gallery. [cited 10/05/2014]; Available from: https://staff.aist.go.jp/nomura-k/english/itscgallary-e.htm

[51] Space Environment (natural and artificial) - Process for determining solar irradiances (ISO 21348). ISO copyright office: Switzerland 2007.

[52] Global Solar UV Index. 2014 [cited 10/05/2014]; Available from: http://www.who.int/uv/publications/globalindex/en/

[53] Properties of sunlight. Terrestrial Solar Radiation. Atmospheric Effects. [cited 10/05/2014]; Available from: http://pveducation.org/pvcdrom/properties-of-sunlight/atmospheric-effects

[54] Mills AL, Soo-Keun. Semiconductor photocatalysis. In: Parsons S, ed. Advanced Oxidation Processes for Water and Wastewater Treatment. London: IWA Publishing 2004, p. 137-66.

[55] Daghrir R, Drogui P, Robert D. Modified TiO2 for environmental photocatalytic applications: A review. Ind Eng Chem Res. 2013; 52 (10):3581-99.

[56] Cao Q, Yu Q, Connell DW, Yu G. Titania/carbon nanotube composite (TiO2/CNT) and its application for removal of organic pollutants. Clean Technol Environ Policy. 2013; 15 (6):871-80.

[57] Park H, Park Y, Kim W, Choi W. Surface modification of TiO2 photocatalyst for environmental applications. J Photochem Photobiol C-Photochem Rev. 2013; 15 (1):1-20.

[58] Ohno T, Akiyoshi M, Umebayashi T, Asai K, Mitsui T, Matsumura M. Preparation of S-doped TiO_2 photocatalysts and their photocatalytic activities under visible light. Appl Catal A-Gen. 2004; 265 (1):115-21.

[59] Klosek S, Raftery D. Visible light driven V-doped TiO_2 photocatalyst and its photooxidation of ethanol. J Phys Chem B. 2001; 105 (14):2815-9.

[60] Braun A, Akurati KK, Fortunato G, Reifler FA, Ritter A, Harvey AS, et al. Nitrogen Doping of TiO2 Photocatalyst Forms a Second eg State in the Oxygen 1s NEXAFS Pre-edge. J Phys Chem C. 2009; 114 (1):516-9.

[61] Chen D, Jiang Z, Geng J, Wang Q, Yang D. Carbon and nitrogen co-doped TiO_2 with enhanced visible-light photocatalytic activity. Ind Eng Chem Res. 2007; 46 (9):2741-6.

[62] Dozzi MV, Selli E. Doping TiO2 with p-block elements: Effects on photocatalytic activity. J Photochem Photobiol C-Photochem Rev. 2013; 14 (1):13-28.

[63] Michalow KA, Logvinovich D, Weidenkaff A, Amberg M, Fortunato G, Heel A, et al. Synthesis, characterization and electronic structure of nitrogen-doped TiO2 nanopowder. Catal Today. 2009; 144 (1–2):7-12.

[64] Devi LG, Kavitha R. A review on non metal ion doped titania for the photocatalytic degradation of organic pollutants under UV/solar light: Role of photogenerated charge carrier dynamics in enhancing the activity. Appl Catal B-Environ. 2013; 140-141:559-87.

[65] Zaleska A. Doped-TiO2: A review. Recent Pat Engin. 2008; 2 (3):157-64.

[66] Akurati KK, Vital A, Dellemann J-P, Michalow K, Graule T, Ferri D, et al. Flame-made WO3/TiO2 nanoparticles: Relation between surface acidity, structure and photocatalytic activity. Appl Catal B-Environ. 2008; 79 (1):53-62.

[67] Leary R, Westwood A. Carbonaceous nanomaterials for the enhancement of TiO2 photocatalysis. Carbon. 2011; 49 (3):741-72.

[68] Morales-Torres S, Pastrana-Martínez LM, Figueiredo JL, Faria JL, Silva AMT. Design of graphene-based TiO2 photocatalysts-a review. Environmental Science and Pollution Research. 2012; 19 (9):3676-87.

[69] Morales-Torres S, Pastrana-Martínez LM, Figueiredo JL, Faria JL, Silva AMT. Graphene oxide-P25 photocatalysts for degradation of diphenhydramine pharmaceutical and methyl orange dye. Appl Surf Sci. 2013; 275:361-8.

[70] Zhang H, Lv X, Li Y, Wang Y, Li J. P25-graphene composite as a high performance photocatalyst. ACS Nano. 2010; 4 (1):380-6.

[71] Marques RRN, Sampaio MJ, Carrapiço PM, Silva CG, Morales-Torres S, Dražić G, et al. Photocatalytic degradation of caffeine: Developing solutions for emerging pollutants. Catal Today. 2013; 209:108-15.

[72] Araña J, Doña-Rodríguez JM, Portillo-Carrizo D, Fernández-Rodríguez C, Pérez-Peña J, González Díaz O, et al. Photocatalytic degradation of phenolic compounds with new TiO2 catalysts. Appl Catal B-Environ. 2010; 100 (1-2):346-54.

[73] Sampaio MJ, Silva CG, Marques RRN, Silva AMT, Faria JL. Carbon nanotube–TiO2 thin films for photocatalytic applications. Catal Today. 2011; 161 (1):91-6.

[74] Yao Y, Li G, Ciston S, Lueptow RM, Gray KA. Photoreactive TiO2/Carbon Nanotube Composites: Synthesis and Reactivity. Environ Sci Technol. 2008; 42 (13):4952-7.

[75] Tian L, Ye L, Deng K, Zan L. TiO2/carbon nanotube hybrid nanostructures: Solvothermal synthesis and their visible light photocatalytic activity. J Solid State Chem. 2011; 184 (6):1465-71.

[76] Silva CG, Faria JL. Photocatalytic Oxidation of Phenolic Compounds by Using a Carbon Nanotube-Titanium Dioxide Composite Catalyst. ChemSusChem. 2010; 3 (5):609-18.

[77] Martínez C, Canle L M, Fernández MI, Santaballa JA, Faria J. Kinetics and mechanism of aqueous degradation of carbamazepine by heterogeneous photocatalysis using nanocrystalline TiO2, ZnO and multi-walled carbon nanotubes-anatase composites. Appl Catal B-Environ. 2011; 102 (3-4):563-71.

[78] Ouyang K, Xie S, Ma X. Photocatalytic activity of TiO2 supported on multi-walled carbon nanotubes under simulated solar irradiation. Ceram Int. 2013; 39 (7):7531-6.

[79] Dionysiou DD, Burbano AA, Suidan MT, Baudin I, Laîné J-M. Effect of Oxygen in a Thin-Film Rotating Disk Photocatalytic Reactor. Environ Sci Technol. 2002; 36 (17):3834-43.

[80] Kowalska E, Rau S. Photoreactors for Wastewater Treatment: A Review. Recent Pat Engin. 2010; 4 (3):242-66.

[81] Langlet M, Kim A, Audier M, Guillard C, Herrmann JM. Transparent photocatalytic films deposited on polymer substrates from sol–gel processed titania sols. Thin Solid Films. 2003; 429 (1–2):13-21.

[82] Sampaio MJ, Silva CG, Silva AM, Vilar VJ, Boaventura RA, Faria JL. Photocatalytic activity of Tio2-coated glass raschig rings on the degradation of phenolic derivatives under simulated solar light irradiation. Chem Eng J. 2013; 224 (1):32-8.

[83] Sampaio MJ, Marques RRN, Tavares PB, Faria JL, Silva AMT, Silva CG. Tailoring the properties of immobilized titanium dioxide/carbon nanotube composites

for photocatalytic water treatment. Journal of Environmental Chemical Engineering (JECE). 2013; 1 (4):945-53.

[84] Bosc F, Ayral A, Albouy P-A, Guizard C. A Simple Route for Low-Temperature Synthesis of Mesoporous and Nanocrystalline Anatase Thin Films. Chem Mater. 2003; 15 (12):2463-8.

[85] Koelsch M, Cassaignon S, Ta Thanh Minh C, Guillemoles JF, Jolivet JP. Electrochemical comparative study of titania (anatase, brookite and rutile) nanoparticles synthesized in aqueous medium. Thin Solid Films. 2004; 451–452 (0):86-92.

[86] Çamurlu HE, Kesmez O, Burunkaya E, Kiraz N, Yeşil Z, Asiltürk M, et al. Sol-gel thin films with anti-reflective and self-cleaning properties. Chem Pap. 2012; 66 (5):461-71.

[87] Wang J, Cai Q, Li H, Cui Y, Wang H. A review on TiO 2 nanotube film photocatalysts prepared by liquid-phase deposition. Int J Photoenergy. 2012; 2012.

[88] Akbarzadeh R, Umbarkar SB, Sonawane RS, Takle S, Dongare MK. Vanadia–titania thin films for photocatalytic degradation of formaldehyde in sunlight. Appl Catal A-Gen. 2010; 374 (1–2):103-9.

[89] Han H, Bai R. Effect of Thickness of Photocatalyst Film Immobilized on a Buoyant Substrate on the Degradation of Methyl Orange Dye in Aqueous Solutions under Different Light Irradiations. Ind Eng Chem Res. 2011; 50 (21):11922-9.

[90] Krýsa J, Novotná P, Kment Š, Mills A. Effect of glass substrate and deposition technique on the properties of sol gel TiO2 thin films. J Photochem Photobiol A-Chem. 2011; 222 (1):81-6.

[91] Yurdakal S, Loddo V, Palmisano G, Augugliaro V, Berber Hs, Palmisano L. Kinetics of 4-Methoxybenzyl Alcohol Oxidation in Aqueous Solution in a Fixed Bed Photocatalytic Reactor. Ind Eng Chem Res. 2009; 49 (15):6699-708.

[92] Pastrana-Martínez LM, Morales-Torres S, Papageorgiou SK, Katsaros FK, Romanos GE, Figueiredo JL, et al. Photocatalytic behaviour of nanocarbon-TiO2 composites and immobilization into hollow fibres. Appl Catal B-Environ. 2013; 142-143:101-11.

[93] Chen Y, Dionysiou DD. Bimodal mesoporous TiO2–P25 composite thick films with high photocatalytic activity and improved structural integrity. Appl Catal B-Environ. 2008; 80 (1–2):147-55.

[94] Seeley ZM, Bandyopadhyay A, Bose S. Titanium dioxide thin films for high temperature gas sensors. Thin Solid Films. 2010; 519 (1):434-8.

[95] Berni A, Mennig M, Schmidt H. Doctor Blade. In: Aegerter M, Mennig M, eds. Sol-Gel Technologies for Glass Producers and Users: Springer US 2004, p. 89-92.

[96] Dresselhaus MS, Dresselhaus G, Jorio A. Unusual Properties and Structure of Carbon Nanotubes. Ann Rev Mater Res. 2004; 34 (1):247-78.

[97] Serp P, Figueiredo JL. Carbon Nanotubes and Nanofibers in Catalysis. In: John Wiley & Sons I, ed. Carbon Materials for Catalysis. New Jersey: John Wiley & Sons, Inc. 2009, p. 309-72.

[98] Ouyang M, Huang J-L, Lieber CM. Fundamental Electronic Properties and Applications of Single-Walled Carbon Nanotubes. Acc Chem Res. 2002; 35 (12):1018-25.

[99] Iijima S. Helical microtubules of graphitic carbon. Nature. 1991; 354 (6348):56-8.

[100] Iijima S, Ichihashi T. Single-shell carbon nanotubes of 1-nm diameter. Nature. 1993; 363 (6430):603-5.

[101] Bethune DS, Klang CH, de Vries MS, Gorman G, Savoy R, Vazquez J, et al. Cobalt-catalysed growth of carbon nanotubes with single-atomic-layer walls. Nature. 1993; 363 (6430):605-7.

[102] Thess A, Lee R, Nikolaev P, Dai H, Petit P, Robert J, et al. Crystalline Ropes of Metallic Carbon Nanotubes. Science. 1996; 273 (5274):483-7.

[103] Eklund P AP, Blackmon R, Hart AJ, Kong J, Pradhan B, et al. WTEC international assessment of research and development of carbon nanotube manufacturing and applications. Technical Report.; 2007.

[104] Danafar F, Fakhru'l-Razi A, Salleh MAM, Biak DRA. Fluidized bed catalytic chemical vapor deposition synthesis of carbon nanotubes-A review. Chem Eng J. 2009; 155 (1-2):37-48.

[105] Dervishi E, Li Z, Xu Y, Saini V, Biris AR, Lupu D, et al. Carbon nanotubes: Synthesis, properties, and applications. Part Sci Technol. 2009; 27 (2):107-25.

[106] Prasek J, Drbohlavova J, Chomoucka J, Hubalek J, Jasek O, Adam V, et al. Methods for carbon nanotubes synthesis - Review. J Mater Chem. 2011; 21 (40):15872-84.

[107] See CH, Harris AT. A review of carbon nanotube synthesis via fluidized-bed chemical vapor deposition. Ind Eng Chem Res. 2007; 46 (4):997-1012.

[108] Terrones M. Science and Technology of the Twenty-First Century: Synthesis, Properties, and Applications of Carbon Nanotubes. Ann Rev Mater Res. 2003; 33:419-501.

[109] Lehman JH, Terrones M, Mansfield E, Hurst KE, Meunier V. Evaluating the characteristics of multiwall carbon nanotubes. Carbon. 2011; 49 (8):2581-602.

[110] Tessonnier J-P, Rosenthal D, Hansen TW, Hess C, Schuster ME, Blume R, et al. Analysis of the structure and chemical properties of some commercial carbon nanostructures. Carbon. 2009; 47 (7):1779-98.

[111] Kumar M, Ando Y. Chemical vapor deposition of carbon nanotubes: A review on growth mechanism and mass production. J Nanosci Nanotechnol. 2010; 10 (6):3739-58.

[112] Rinaldi A, Frank B, Su DS, Hamid SBA, Schlögl R. Facile Removal of Amorphous Carbon from Carbon Nanotubes by Sonication. Chem Mater. 2011; 23 (4):926-8.

[113] Behler K, Osswald S, Ye H, Dimovski S, Gogotsi Y. Effect of thermal treatment on the structure of multi-walled carbon nanotubes. J Nanopart Res. 2006; 8 (5):615-25.

[114] Serp P, Corrias M, Kalck P. Carbon nanotubes and nanofibers in catalysis. Applied Catalysis A: General. 2003; 253 (2):337-58.

[115] Pahmy RH, Mohamed AR. Utilization of carbon nanotubes as a support material in metal-based catalyst systems: Applications in catalysis. Recent Pat Engin. 2012; 6 (1):31-47.

[116] Endo M, Strano MS, Ajayan PM. Potential applications of carbon nanotubes. In: Jorio A, Dresselhaus G, Dresselhaus MS, eds. Carbon Nanotubes Advanced Topics in the Synthesis, Structure, Properties and Applications: Springer-Verlag Berlin Heidelberg 2008, p. 13-62.

[117] Schnorr JM, Swager TM. Emerging Applications of Carbon Nanotubes. Chem Mater. 2010; 23 (3):646-57.

[118] Baughman RH, Zakhidov AA, de Heer WA. Carbon Nanotubes--the Route Toward Applications. Science. 2002; 297 (5582):787-92.

[119] Charlier JC. Defects in carbon nanotubes. Acc Chem Res. 2002; 35 (12):1063-9.

[120] Banerjee S, Hemraj-Benny T, Wong SS. Covalent Surface Chemistry of Single-Walled Carbon Nanotubes. Adv Mater. 2005; 17 (1):17-29.

[121] Balasubramanian K, Burghard M. Chemically Functionalized Carbon Nanotubes. Small. 2005; 1 (2):180-92.

[122] De Volder MFL, Tawfick SH, Baughman RH, Hart AJ. Carbon nanotubes: Present and future commercial applications. Science. 2013; 339 (6119):535-9.

[123] Oriňáková R, Oriňák A. Recent applications of carbon nanotubes in hydrogen production and storage. Fuel. 2011; 90 (11):3123-40.

[124] Vairavapandian D, Vichchulada P, Lay MD. Preparation and modification of carbon nanotubes: Review of recent advances and applications in catalysis and sensing. Anal Chim Acta. 2008; 626 (2):119-29.

[125] Garcia J, Gomes HT, Serp P, Kalck P, Figueiredo JL, Faria JL. Carbon nanotube supported ruthenium catalysts for the treatment of high strength wastewater with aniline using wet air oxidation. Carbon. 2006; 44 (12):2384-91.

[126] Akuzawa N, Okano Y, Iwashita T, Matsumoto R, Soneda Y. Application of alkali metal-doped carbons for hydrogen recovery and isotope separation. J Nanosci Nanotechnol. 2011; 11 (10):9046-9.

[127] Li N, Lee G, Yang JW, Kim H, Yeom MS, Scheicher RH, et al. Noncovalent functionalization with alkali metal to separate semiconducting from metallic carbon nanotubes: A theoretical study. J Phys Chem C. 2013; 117 (8):4309-13.

[128] Baleizão C, Gigante B, Garcia H, Corma A. Vanadyl salen complexes covalently anchored to single-wall carbon nanotubes as heterogeneous catalysts for the cyanosilylation of aldehydes. J Catal. 2004; 221 (1):77-84.

[129] Zhang Y, Li J, Gao F, Kang F, Wang X, Ye F, et al. Electropolymerization and electrochemical performance of salen-type redox polymer on different carbon supports for supercapacitors. Electrochim Acta. 2012; 76:1-7.

[130] Lafuente E, Callejas MA, Sainz R, Benito AM, Maser WK, Sanjuán ML, et al. The influence of single-walled carbon nanotube functionalization on the electronic properties of their polyaniline composites. Carbon. 2008; 46 (14):1909-17.

[131] Liao Y, Li XG, Hoek EMV, Kaner RB. Carbon nanotube/polyaniline nanofiber ultrafiltration membranes. J Mater Chem A. 2013; 1 (48):15390-6.

[132] Afkhami A, Soltani-Felehgari F, Madrakian T, Ghaedi H. Surface decoration of multi-walled carbon nanotubes modified carbon paste electrode with gold nanoparticles for electro-oxidation and sensitive determination of nitrite. Biosens Bioelectron. 2014; 51:379-85.

[133] Wang S, Li L, Jin H, Yang T, Bao W, Huang S, et al. Electrochemical detection of hepatitis B and papilloma virus DNAs using SWCNT array coated with gold nanoparticles. Biosens Bioelectron. 2013; 41 (1):205-10.

[134] Rocha RP, Silva AMT, Romero SMM, Pereira MFR, Figueiredo JL. The role of O- and S-containing surface groups on carbon nanotubes for the elimination of organic pollutants by catalytic wet air oxidation. Appl Catal B-Environ. 2014; 147:314-21.

[135] Datsyuk V, Kalyva M, Papagelis K, Parthenios J, Tasis D, Siokou A, et al. Chemical oxidation of multiwalled carbon nanotubes. Carbon. 2008; 46 (6):833-40.

[136] Reyhani A, Mortazavi SZ, Nozad Golikand A, Moshfegh AZ, Mirershadi S. The effect of various acids treatment on the purification and electrochemical hydrogen storage of multi-walled carbon nanotubes. J Power Sources. 2008; 183 (2):539-43.

[137] Pereira MFR, Figueiredo JL, Órfão JJM, Serp P, Kalck P, Kihn Y. Catalytic activity of carbon nanotubes in the oxidative dehydrogenation of ethylbenzene. Carbon. 2004; 42 (14):2807-13.

[138] Solhy A, Machado BF, Beausoleil J, Kihn Y, Gonçalves F, Pereira MFR, et al. MWCNT activation and its influence on the catalytic performance of Pt/MWCNT catalysts for selective hydrogenation. Carbon. 2008; 46 (9):1194-207.

[139] Tedim J, Gonçalves F, Pereira MFR, Figueiredo JL, Moura C, Freire C, et al. Preparation and characterization of poly[Ni(salen)(crown receptor)]/multi-walled carbon nanotube composite films. Electrochim Acta. 2008; 53 (23):6722-31.

[140] Liu J, Rinzler AG, Dai H, Hafner JH, Bradley RK, Boul PJ, et al. Fullerene Pipes. Science. 1998; 280 (5367):1253-6.

[141] Kuznetsova A, Popova I, Yates JT, Bronikowski MJ, Huffman CB, Liu J, et al. Oxygen-Containing Functional Groups on Single-Wall Carbon Nanotubes: NEXAFS and Vibrational Spectroscopic Studies. J Am Chem Soc. 2001; 123 (43):10699-704.

[142] Liu M, Yang Y, Zhu T, Liu Z. A General Approach to Chemical Modification of Single-Walled Carbon Nanotubes with Peroxy Organic Acids and Its Application in Polymer Grafting. J Phys Chem C. 2007; 111 (6):2379-85.

[143] Laudenbach J, Gebhardt B, Syrgiannis Z, Hauke F, Hirsch A, Maultzsch J. Raman bands of nano-graphene flakes on carbon nanotubes after oxidation. Phys Status Solidi B. 2013; 250 (12):2687-91.

[144] Likodimos V, Steriotis TA, Papageorgiou SK, Romanos GE, Marques RRN, Rocha RP, et al. Controlled surface functionalization of multiwall carbon nanotubes by HNO3 hydrothermal oxidation. Carbon. 2014; 69:311-26.

[145] Hou P-X, Liu C, Cheng H-M. Purification of carbon nanotubes. Carbon. 2008; 46 (15):2003-25.

[146] Wang Q, Yang D, Chen D, Wang Y, Jiang Z. Synthesis of anatase titania-carbon nanotubes nanocomposites with enhanced photocatalytic activity through a nanocoating-hydrothermal process. J Nanopart Res. 2007; 9 (6):1087-96.

[147] Noh JS, Schwarz JA. Effect of HNO3 treatment on the surface acidity of activated carbons. Carbon. 1990; 28 (5):675-82.

[148] Papirer E, Dentzer J, Li S, Donnet JB. Surface groups on nitric acid oxidized carbon black samples determined by chemical and thermodesorption analyses. Carbon. 1991; 29 (1):69-72.

[149] Bandosz TJ, Jagiello J, Schwarz JA. Comparison of methods to assess surface acidic groups on activated carbons. Anal Chem. 1992; 64 (8):891-5.

[150] Otake Y, Jenkins RG. Characterization of oxygen-containing surface complexes created on a microporous carbon by air and nitric acid treatment. Carbon. 1993; 31 (1):109-21.

[151] Fanning PE, Vannice MA. A DRIFTS study of the formation of surface groups on carbon by oxidation. Carbon. 1993; 31 (5):721-30.

[152] Vinke P, van der Eijk M, Verbree M, Voskamp AF, van Bekkum H. Modification of the surfaces of a gasactivated carbon and a chemically activated carbon with nitric acid, hypochlorite, and ammonia. Carbon. 1994; 32 (4):675-86.

[153] Menéndez JA, Illán-Gómez MJ, y León CAL, Radovic LR. On the difference between the isoelectric point and the point of zero charge of carbons. Carbon. 1995; 33 (11):1655-7.

[154] Moreno-Castilla C, Ferro-Garcia MA, Joly JP, Bautista-Toledo I, Carrasco-Marin F, Rivera-Utrilla J. Activated Carbon Surface Modifications by Nitric Acid, Hydrogen Peroxide, and Ammonium Peroxydisulfate Treatments. Langmuir. 1995; 11 (11):4386-92.

[155] Hu H, Zhao B, Itkis ME, Haddon RC. Nitric Acid Purification of Single-Walled Carbon Nanotubes. J Phys Chem B. 2003; 107 (50):13838-42.

[156] Apolinário ÂC, Silva AMT, Machado BF, Gomes HT, Araújo PP, Figueiredo JL, et al. Wet air oxidation of nitro-aromatic compounds: Reactivity on single- and multi-component systems and surface chemistry studies with a carbon xerogel. Appl Catal B-Environ. 2008; 84 (1–2):75-86.

[157] Gomes HT, Machado BF, Ribeiro A, Moreira I, Rosário M, Silva AMT, et al. Catalytic properties of carbon materials for wet oxidation of aniline. J Hazard Mater. 2008; 159 (2–3):420-6.

[158] Silva AMT, Machado BF, Figueiredo JL, Faria JL. Controlling the surface chemistry of carbon xerogels using HNO3-hydrothermal oxidation. Carbon. 2009; 47 (7):1670-9.

[159] Seredych M, Tamashausky AV, Bandosz TJ. Surface features of exfoliated graphite/bentonite composites and their importance for ammonia adsorption. Carbon. 2008; 46 (9):1241-52.

[160] Calvillo L, Lázaro MJ, García-Bordejé E, Moliner R, Cabot PL, Esparbé I, et al. Platinum supported on functionalized ordered mesoporous carbon as electrocatalyst for direct methanol fuel cells. J Power Sources. 2007; 169 (1):59-64.

[161] Salgado JRC, Quintana JJ, Calvillo L, Lazaro MJ, Cabot PL, Esparbe I, et al. Carbon monoxide and methanol oxidation at platinum catalysts supported on ordered mesoporous carbon: the influence of functionalization of the support. Phys Chem Chem Phys. 2008; 10 (45):6796-806.

[162] Zhang J, Zou H, Qing Q, Yang Y, Li Q, Liu Z, et al. Effect of Chemical Oxidation on the Structure of Single-Walled Carbon Nanotubes. J Phys Chem B. 2003; 107 (16):3712-8.

[163] Park T-J, Banerjee S, Hemraj-Benny T, Wong SS. Purification strategies and purity visualization techniques for single-walled carbon nanotubes. J Mater Chem. 2006; 16 (2):141-54.

[164] Yang C-M, Park JS, An KH, Lim SC, Seo K, Kim B, et al. Selective Removal of Metallic Single-Walled Carbon Nanotubes with Small Diameters by Using Nitric and Sulfuric Acids. J Phys Chem B. 2005; 109 (41):19242-8.

[165] Komatsu N, Wang F. A comprehensive review on separation methods and techniques for single-walled carbon nanotubes. Materials. 2010; 3 (7):3818-44.

[166] Kundu S, Wang Y, Xia W, Muhler M. Thermal Stability and Reducibility of Oxygen-Containing Functional Groups on Multiwalled Carbon Nanotube Surfaces: A Quantitative High-Resolution XPS and TPD/TPR Study. J Phys Chem C. 2008; 112 (43):16869-78.

[167] Wepasnick KA, Smith BA, Schrote KE, Wilson HK, Diegelmann SR, Fairbrother DH. Surface and structural characterization of multi-walled carbon nanotubes following different oxidative treatments. Carbon. 2011; 49 (1):24-36.

[168] Marques RRN, Machado BF, Faria JL, Silva AMT. Controlled generation of oxygen functionalities on the surface of Single-Walled Carbon Nanotubes by HNO3 hydrothermal oxidation. Carbon. 2010; 48 (5):1515-23.

[169] Gerber I, Oubenali M, Bacsa R, Durand J, Gonçalves A, Pereira MFR, et al. Theoretical and Experimental Studies on the Carbon-Nanotube Surface Oxidation by Nitric Acid: Interplay between Functionalization and Vacancy Enlargement. Chem-Eur J. 2011; 17 (41):11467-77.

[170] Tchoul MN, Ford WT, Lolli G, Resasco DE, Arepalli S. Effect of Mild Nitric Acid Oxidation on Dispersability, Size, and Structure of Single-Walled Carbon Nanotubes. Chem Mater. 2007; 19 (23):5765-72.

[171] Smith B, Wepasnick K, Schrote KE, Cho H-H, Ball WP, Fairbrother DH. Influence of Surface Oxides on the Colloidal Stability of Multi-Walled Carbon Nanotubes: A Structure−Property Relationship. Langmuir. 2009; 25 (17):9767-76.

[172] Kim SW, Kim T, Kim YS, Choi HS, Lim HJ, Yang SJ, et al. Surface modifications for the effective dispersion of carbon nanotubes in solvents and polymers. Carbon. 2012; 50 (1):3-33.

[173] Coleman JN, Khan U, Blau WJ, Gun'ko YK. Small but strong: A review of the mechanical properties of carbon nanotube–polymer composites. Carbon. 2006; 44 (9):1624-52.

[174] Karousis N, Tagmatarchis N, Tasis D. Current Progress on the Chemical Modification of Carbon Nanotubes. Chem Rev. 2010; 110 (9):5366-97.

[175] Andrade NF, Martinez DST, Paula AJ, Silveira JV, Alves OL, Souza Filho AG. Temperature effects on the nitric acid oxidation of industrial grade multiwalled carbon nanotubes. J Nanopart Res. 2013; 15 (7).

[176] Bergeret Cl, Cousseau J, Fernandez V, Mevellec J-Y, Lefrant S. Spectroscopic Evidence of Carbon Nanotubes' Metallic Character Loss Induced by Covalent Functionalization via Nitric Acid Purification. J Phys Chem C. 2008; 112 (42):16411-6.

[177] Salzmann CG, Llewellyn SA, Tobias G, Ward MAH, Huh Y, Green MLH. The Role of Carboxylated Carbonaceous Fragments in the Functionalization and Spectroscopy of a Single-Walled Carbon-Nanotube Material. Adv Mater. 2007; 19 (6):883-7.

[178] Yu H, Jin Y, Peng F, Wang H, Yang J. Kinetically Controlled Side-Wall Functionalization of Carbon Nanotubes by Nitric Acid Oxidation. J Phys Chem C. 2008; 112 (17):6758-63.

[179] Worsley KA, Kalinina I, Bekyarova E, Haddon RC. Functionalization and Dissolution of Nitric Acid Treated Single-Walled Carbon Nanotubes. J Am Chem Soc. 2009; 131 (50):18153-8.

[180] Price BK, Lomeda JR, Tour JM. Aggressively Oxidized Ultra-Short Single-Walled Carbon Nanotubes Having Oxidized Sidewalls. Chem Mater. 2009; 21 (17):3917-23.

[181] Romanos GE, Likodimos V, Marques RRN, Steriotis TA, Papageorgiou SK, Faria JL, et al. Controlling and Quantifying Oxygen Functionalities on Hydrothermally and Thermally Treated Single-Wall Carbon Nanotubes. J Phys Chem C. 2011; 115 (17):8534-46.

[182] Del Canto E, Flavin K, Movia D, Navio C, Bittencourt C, Giordani S. Critical Investigation of Defect Site Functionalization on Single-Walled Carbon Nanotubes. Chem Mater. 2010; 23 (1):67-74.

[183] Rosca ID, Watari F, Uo M, Akasaka T. Oxidation of multiwalled carbon nanotubes by nitric acid. Carbon. 2005; 43 (15):3124-31.

[184] Verdejo R, Lamoriniere S, Cottam B, Bismarck A, Shaffer M. Removal of oxidation debris from multi-walled carbon nanotubes. Chem Commun. 2007; (5):513-5.

[185] González-Guerrero AB, Mendoza E, Pellicer E, Alsina F, Fernández-Sánchez C, Lechuga LM. Discriminating the carboxylic groups from the total acidic sites in oxidized multi-wall carbon nanotubes by means of acid–base titration. Chem Phys Lett. 2008; 462 (4–6):256-9.

[186] Wang Z, Shirley MD, Meikle ST, Whitby RLD, Mikhalovsky SV. The surface acidity of acid oxidised multi-walled carbon nanotubes and the influence of in-situ generated fulvic acids on their stability in aqueous dispersions. Carbon. 2009; 47 (1):73-9.

[187] Rinaldi A, Zhang J, Frank B, Su DS, Abd Hamid SB, Schlögl R. Oxidative Purification of Carbon Nanotubes and Its Impact on Catalytic Performance in Oxidative Dehydrogenation Reactions. ChemSusChem. 2010; 3 (2):254-60.

[188] Ambrosi A, Pumera M. Amorphous Carbon Impurities Play an Active Role in Redox Processes of Carbon Nanotubes. J Phys Chem C. 2011; 115 (51):25281-4.

[189] Zhang M, Yudasaka M, Iijima S. Diameter Enlargement of Single-Wall Carbon Nanotubes by Oxidation. J Phys Chem B. 2004; 108 (1):149-53.

[190] Zhou W, Vavro J, Nemes NM, Fischer JE, Borondics F, Kamarás K, et al. Charge transfer and Fermi level shift in *p*-doped single-walled carbon nanotubes. Phys Rev B. 2005; 71 (20):205423.

[191] Forrest GA, Alexander AJ. A Model for the Dependence of Carbon Nanotube Length on Acid Oxidation Time. J Phys Chem C. 2007; 111 (29):10792-8.

[192] Dementev N, Feng X, Borguet E. Fluorescence Labeling and Quantification of Oxygen-Containing Functionalities on the Surface of Single-Walled Carbon Nanotubes. Langmuir. 2009; 25 (13):7573-7.

[193] Moraitis G, Špitalský Z, Ravani F, Siokou A, Galiotis C. Electrochemical oxidation of multi-wall carbon nanotubes. Carbon. 2011; 49 (8):2702-8.

[194] Ming J, Wu Y, Yu Y, Zhao F. Steaming multiwalled carbon nanotubesvia acid vapour for controllable nanoengineering and the fabrication of carbon nanoflutes. Chem Commun. 2011; 47 (18):5223-5.

[195] Boehm HP. Surface oxides on carbon and their analysis: a critical assessment. Carbon. 2002; 40 (2):145-9.

[196] Itkis ME, Perea DE, Jung R, Niyogi S, Haddon RC. Comparison of Analytical Techniques for Purity Evaluation of Single-Walled Carbon Nanotubes. J Am Chem Soc. 2005; 127 (10):3439-48.

[197] Dresselhaus MS, Dresselhaus G, Saito R, Jorio A. Raman spectroscopy of carbon nanotubes. Phys Rep. 2005; 409 (2):47-99.

[198] Pimenta MA, Dresselhaus G, Dresselhaus MS, Cancado LG, Jorio A, Saito R. Studying disorder in graphite-based systems by Raman spectroscopy. Phys Chem Chem Phys. 2007; 9 (11):1276-90.

[199] Dresselhaus MS, Jorio A, Hofmann M, Dresselhaus G, Saito R. Perspectives on carbon nanotubes and graphene Raman spectroscopy. Nano Lett. 2010; 10 (3):751-8.

[200] Cançado LG, Hartschuh A, Novotny L. Tip-enhanced Raman spectroscopy of carbon nanotubes. J Raman Spectrosc. 2009; 40 (10):1420-6.

[201] Fantini C, Pimenta MA, Strano MS. Two-Phonon Combination Raman Modes in Covalently Functionalized Single-Wall Carbon Nanotubes. J Phys Chem C. 2008; 112 (34):13150-5.

[202] Maciel IO, Anderson N, Pimenta MA, Hartschuh A, Qian H, Terrones M, et al. Electron and phonon renormalization near charged defects in carbon nanotubes. Nat Mater. 2008; 7 (11):878-83.

[203] Kavan L, Kalbáč M, Zukalová M, Dunsch L. Electrochemical Doping of Chirality-Resolved Carbon Nanotubes. J Phys Chem B. 2005; 109 (42):19613-9.

[204] Graupner R. Raman spectroscopy of covalently functionalized single-wall carbon nanotubes. J Raman Spectrosc. 2007; 38 (6):673-83.

Part II

Experimental Setups and Analytical Techniques

2 Experimental Setups

Different setups were used to perform the experimental studies involved on the modification of carbon nanotubes surface chemistry through liquid nitric acid oxidation and on photocatalytic reactions in liquid phase to assess the catalytic activity of the prepared TiO_2/CNT composites. The experimental setups and the corresponding procedures performed in the present study are described in this section.

2.1 Experimental Setups used for CNTs functionalization

The surface of the CNTs was modified through oxidation with nitric acid by applying a recently proposed approach through hydrothermal activation, tested previously over carbon xerogels [1]. The description of this methodology is described below and, for comparison with the commonly used boiling acid methods, boiling oxidation was also tested at much higher nitric acid concentrations.

2.1.1 CNTs hydrothermal functionalization with HNO_3

Hydrothermal functionalization of pristine CNTs followed an experimental procedure performed in a 160 mL autoclave (Parr Instruments, USA Mod. 4564) equipped with a temperature controller and a turbine-type agitation system (Figure 2.1). Aqueous solutions of HNO_3 with variable concentrations (0 - 0.30 mol L^{-1}), prepared from HNO_3 65 wt %, were used at temperatures of 393 and 473 K. An amount of CNTs (0.2 or 0.5 g) was added to 75 mL of a HNO_3 aqueous solution with the desired concentration, the vessel was sealed and the solution was flushed with nitrogen for 5 min to remove dissolved oxygen. At that time, the system was pressurized with 0.5 MPa of nitrogen and heated up to the desired temperature at autogeneous pressure under continuous stirring at 300 rpm. After 2 h of operation, the CNTs were recovered, washed several times with distilled water until a neutral pH of the rinsing water and dried overnight at 393 K. A blank experiment was also performed using distilled water instead of nitric acid.

Figure 2.1 – Autoclave and temperature controller used in the functionalization of CNTs.

2.1.2 CNTs boiling oxidation with HNO_3

In a typical activation run, the CNTs were immersed in 150 mL of a HNO_3 solution with a concentration of 7.0 or 10 mol L^{-1}. A round bottom flask equipped with a condenser was used and the suspension was heated to boiling temperature and kept under magnetic stirring for 3 h. After cooling, the suspension was washed up until a neutral pH of the rinsing water was attained and the recovered nanotubes were dried overnight at 393 K.

2.2 Experimental Setups used for photocatalytic studies

The setups used to study catalysts activity, either in powder or film form, are here described. Two type of photo-reactors and light sources were tested in different conditions.

2.2.1 Immersion reactor

The first photocatalytic experiments were carried out in an immersion reactor with 5 main units: the immersion lamp placed inside a quartz housing, a glass cooling jacket, the photocatalytic reactor, the magnetic stirrer and the gas feed, as shown in Figure 2.2.

(a)  (b) 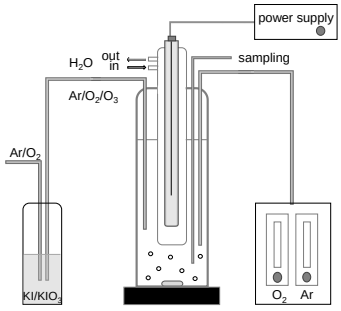

Figure 2.2 – Photocatalytic immersion reactor setup picture (a) and scheme (b).

The lamp in use was an UV-vis Heraeus TQ 150 medium pressure mercury vapour lamp located axially and held in a quartz immersion tube with the more intense lines at 254, 313, 365, 436, 546 and 578 nm (Figure 2.3). The use of the DURAN 50® glass

jacket allows to cool by water circulation to maintain a constant temperature, acting also as an optical cut-off of UVB and UVC radiation. The resulting emission lines are represented in Figure 2.3 a, as confirmed by the irradiance spectrum measured with a UV-vis spectroradiometer USB2000+, OceanOptics, USA, shown in Figure 2.3 b.

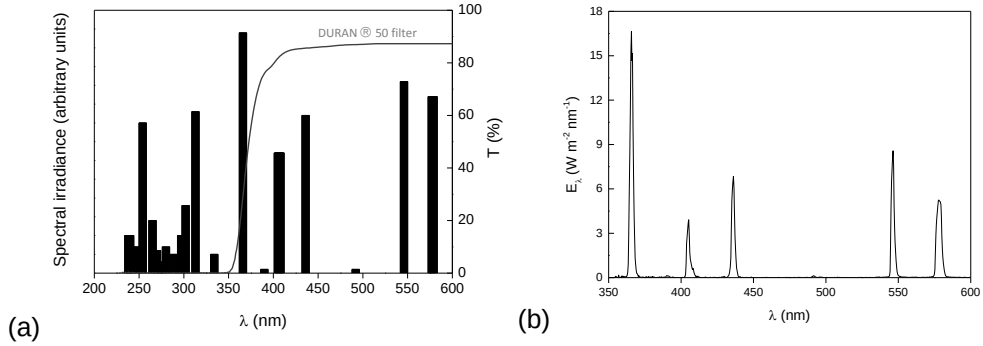

Figure 2.3 – Spectral irradiance of the TQ 150 lamp:
(a) data provided by the manufacturer and cut-off effect of DURAN® filter
(b) emission lines recorded in the laboratory at a distance of 7 cm from the irradiation source through a borosilicate glass filter.

In a typical experiment the reactor is charged with a fixed amount of catalyst in powder form and with 250 mL of the organic solution, under magnetic stirring, being continuously bubbled with oxygen diluted in argon. After a dark phase, which is performed until the adsorption-desorption equilibrium of the organic on the surface of the catalyst is reached, the light is turned on and the suspension starts to be illuminated.

2.2.2 Reactor with external light source

Photocatalytic experiments using supported catalysts deposited over thin glass slides in the form of films, were performed in a borosilicate reactor with a cylindrical configuration, as shown in Figure 2.4 a. The thin glass round slides can be carefully placed on the top of the reactor cover and fixed with a Viton® O-ring. The reaction setup is composed by the same main components as the one previously described for the reactions using powder catalysts, namely the emission lamp with the irradiation characteristics specified in Section 2.2.1, but in this case placed in an external position, as illustrated in Figure 2.4 b. The TQ150 medium pressure mercury

vapour lamp, located inside the glass cooling jacket, illuminates the cylindrical photo-reactor placed over the magnetic stirrer and fed with O_2.

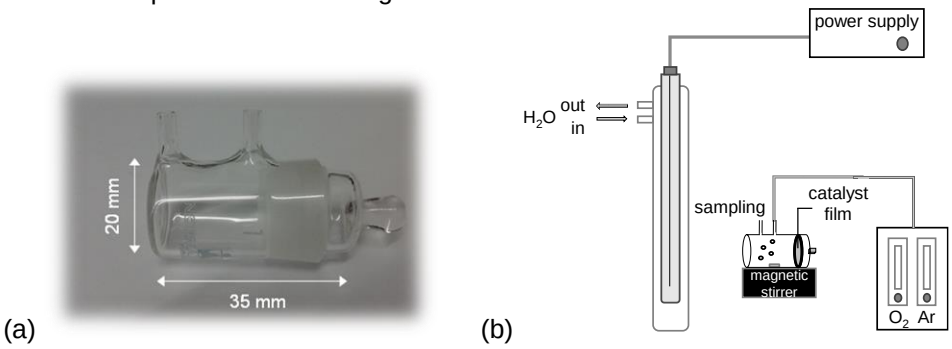

(a) (b)

Figure 2.4 – Photocatalytic cylindrical reactor (a) and setup scheme (b).

In a typical experiment, the photo-reactor is sealed with the catalyst film fixed at the top of the reactor cover and the magnetic bar inside and filled with 7 mL of the contaminant aqueous solution through one of the top openings. The reactor is then positioned over the magnetic stirrer and the gas feed is turned on flowing through the top opening closer to the cap and the other one is used for sampling (see Figure 2.4). For all the reactions performed in the abovementioned configurations, the dark period necessary to establish adsorption-desorption equilibrium is studied for each couple of catalyst/organic compound, until the concentration of the last is constant and the corresponding instant considered as t = 0 for the photocatalytic reactions, when the irradiation is turned on. At this time, in order to determine the organic concentration in solution, the first sample is withdrawn and is then considered as the initial concentration (C_0) after dark adsorption for further calculations of conversion results. An experiment in the absence of catalyst is also performed, to be considered as the blank experiment, in order to calculate the contribution from direct photolysis. The gas feed is used to provide oxygen in solution which acts as electron acceptor.

Samples were periodically withdrawn, centrifuged and analyzed by High Performance Liquid Chromatography (HPLC) at the conditions described in Section 3.2.1 of the following Chapter 3.

2.3 References

[1] Silva AMT, Machado BF, Figueiredo JL, Faria JL. Controlling the surface chemistry of carbon xerogels using HNO3-hydrothermal oxidation. Carbon. 2009; 47 (7):1670-9.

3 Analytical Techniques

In this section there are described the procedures and conditions concerning the analytical techniques employed to determine the surface chemistry, thermal stability, morphology, structure and electronic properties of the solid materials and to perform product analysis to follow photo degradation experiments.

3.1 Materials characterization

3.1.1 Temperature Programmed Desorption (TPD)

The surface chemistry of the CNTs was quantified in terms of oxygen functional groups by TPD analysis using an AMI-200 Catalyst Characterization Instrument (Altamira Instruments) equipped with a quadrupole mass spectrometer (Ametek, Mod. Dymaxion). Each sample (0.1 g) was placed in a U-shaped quartz tube and heated at 5 K min^{-1} until reach the maximum temperature of 1273 K in an electrical furnace, under a constant flow of 25 cm^3 min^{-1} of helium, used as carrier gas. The amount of CO and CO_2 released was determined using the calibration performed at the end of each analysis and the experimental error was lower than 8%. Deconvolution of the obtained CO and CO_2 spectra allows quantifying the amount of each specific oxygen functionality which are desorbed at known temperature ranges.

3.1.2 Thermogravimetric Analysis (TGA)

Thermogravimetric studies were performed to investigate the thermal stability of selected materials and the amount of volatiles and ash content on CNTs. Both analyses were conducted in different equipments.

TGA was performed using a Mettler M3 balance to assess the fixed carbon and the ash content of pristine and functionalized CNTs. Firstly, humidity was removed at a constant temperature of 383 K under N_2. Then, the samples were heated at 25 K min^{-1} to the final temperature of 1173 K. The weight change observed during this stage allows the quantification of volatile compounds at the surface. When a constant weight was attained, the amount of fixed carbon was determined and the gas feed was turned to O_2 until a new stable weight was reached. At these conditions, the entire organic fraction of the sample is burned and the remaining material corresponds to the ash content.

Thermogravimetry with simultaneous differential scanning calorimetry (DSC) was conducted on a Setaram SETSYS Evolution 16/18, TGA/DSC analyzer. For each experiment, approximately 20 mg of the material was loaded on the sample crucible, the system was sealed, fed with 16 cm^3 min^{-1} air (purity 99.9%) and a temperature ramp (10 K min^{-1}) was applied. For simultaneous DSC measurements the system was pre-calibrated with a series of standards following the manufacturer's procedure.

3.1.3 Water vapor adsorption/desorption

Water vapor adsorption-desorption measurements were conducted on a microbalance (CI Electronics, UK) as a rapid indicative of the modification on CNTs surface after HNO_3 functionalization, regarding the creation of acidic surface groups where the water molecules are preferentially adsorbed. The mass of the samples and counterweight pans, the hooks, the counterweight material, and the hang chains of the microbalance assembly were on the order of 100 - 300 mg/item and were defined with an accuracy of ± 0.1%. The materials were appropriately selected to induce a symmetrical configuration to the balance setup in order to minimize buoyancy effects. The microbalance had a 0.1 μg stable resolution. Before each measurement, the samples were degassed under high vacuum (10^{-5} mbar) at 180 ºC.

3.1.4 Nitrogen adsorption isotherms (N_2 isotherms)

Materials specific surface area calculation based on the Brunauer-Emmett-Teller (BET) theory (S_{BET}) was determined by multipoint analysis of N_2 adsorption isotherms at 77 K in the relative pressure range from 0.05 to 0.3 using BET method, with a Quantachrome NOVA 4200e multi-station apparatus. Each sample was degassed under vacuum for 6 h at 573 K prior to analysis.

In some cases, N_2 adsorption-desorption measurements were carried out at 77 K in the relative pressure range of 10^{-5}-0.995 on a Quantachrome Autosorb-1-MP apparatus. Each sample (60-80 mg) was outgassed under high vacuum at 573 K overnight, prior to analysis.

Pore size distributions (PSDs) were obtained after using the Quenched Solid Density Functional Theory (QSDFT) N_2-carbon equilibrium transition kernel at 77 K of Quantachrome's Library.

3.1.5 Raman spectroscopy

Raman measurements were conducted to explore modifications on the graphitic structure of CNTs at nanoscale and were performed in backscattering configuration using a Renishaw inVia Reflex microscope with an Ar^+ ion laser (λ = 514.5 nm, E = 2.41 eV) and a high power near-infrared (NIR) diode laser (λ = 785 nm, E = 1.58 eV) as excitation sources. The laser light was focused on the samples using a long working distance (8 mm) 50 x (NA = 0.55) objective of a Leica DMLM microscope at

power density lower than 0.05 mW μm^{-2} for both laser lines, to avoid sample heating. The spectra were averaged over 5-10 randomly different spots for each sample, while the frequency shifts were calibrated by an internal Si reference. Spectral deconvolution was carried out by nonlinear least-squares fitting of the Raman peaks to a mixture of Lorentzian and Gaussian lineshapes.

3.1.6 Diffuse reflectance UV-Vis (DRUV) spectroscopy

Diffuse reflectance spectroscopy in the range of UV-Vis was performed to characterize catalysts absorption bands within electronic transitions are allowed. The spectra were collected on a Jasco V-560 UV-Vis spectrophotometer, equipped with an integrating sphere attachment (JASCO ISV-469), and transformed by the instrument software (JASCO) to equivalent absorption Kubelka-Munk units.

3.1.7 Diffuse reflectance infrared Fourier transformed (DRIFT) spectroscopy

Surface structure of the TiO_2 catalysts was assessed through vibrational DRIFT spectroscopy, which was performed in a Nicolet 510P FTIR Spectrometer equipped with a beam collector (Spectra Tech). The interferograms were converted to equivalent absorption units in the Kubelka-Munk scale by using the instrument software (OMNIC).

3.1.8 Electron microscopy

Morphology and phase dispersion on TiO_2/CNT composites was observed through both Scanning Electron Microscopy (SEM) performed in a FEI Quanta 400FEG ESEM/EDAX Genesis X4M instrument and Transmission Electron Microscopy (TEM) analysis in a JEOL 2010F analytical electron microscope, equipped with a Schottky field-emission gun.

3.1.9 X-ray diffraction (XRD)

Crystalline phase and crystallite size of TiO_2 particles was calculated based on XRD spectral analysis, which was carried out in a PANalytical X'Pert MPD equipped with a X'Celerator detector and secondary monochromator (Cu Kα λ = 0.154 nm, 50 kV, 40 mA; data recorded at a 0.017º step size, 100 s/step).

3.2 Product analysis

3.2.1 High Performance Liquid Chromatography (HPLC)

Concentration of organics degraded in photocatalytic experiments were followed through HPLC. The samples were previously centrifuged, in the case of powder suspensions, and analyzed using a Hitachi Elite LaChrom instrument equipped with a Diode Array Detector (L-2450), a Purospher Star RP-18 column (250 mm x 4.6 mm, 5 µm particles), and a solvent delivery pump (L-2130) at a fixed flow rate of 1 mL min^{-1}. At first, the column was equilibrated with a A:B (70:30) mixture of ultra-pure water (A) and methanol (B), followed by a linear gradient run to A:B (30:70) in 30 min, and finally with isocratic elution during 2 min.

3.2.2 UV-Vis spectroscopy

UV-Vis spectroscopy was conducted to monitor the concentration of some organics in liquid phase, which were being oxidized through photocatalytic degradation. The absorption spectra were recorded on a Jasco V-560 UV-Vis spectrophotometer.

Part III

Modification of CNTs surface chemistry

4 SWCNTs functionalization by hydrothermal oxidation

Controlled generation of oxygen functionalities by HNO_3 hydrothermal oxidation on the surface of single-walled carbon nanotubes and characterization of its chemically modified surface[1, 2]

The surface chemistry of single-walled carbon nanotubes (SWCNTs) is finely tailored by a HNO_3 hydrothermal method. The degree of oxygen functionalization is correlated with HNO_3 concentration through a mathematical function. Operating temperature and HNO_3 concentration are key parameters in the modification of the surface chemistry. Temperature programmed desorption, water adsorption/desorption, thermogravimetric studies, nitrogen adsorption isotherms and porosimetry analysis were the techniques used to determine the nature, concentration and acidic strength of different oxygen functionalities, which are introduced in a controlled mode. These results were correlated to Raman spectroscopy data that allowed identifying the marked evolution of the defect-activated phonon modes of SWCNTs (Institute of Advanced Materials, NCSR Demokritos, Greece). The SWCNTs functionalization procedure can be effectively controlled and quantified, and the optimum conditions can be defined in relation to the desired physicochemical properties and pore structure characteristics for specific applications.

[1] **Marques, R.R.N.**, Machado, B.F., Faria, J.L., Silva, A.M.T. (2010) Controlled generation of oxygen functionalities on the surface of single-walled carbon nanotubes by HNO_3 hydrothermal oxidation. Carbon, 48, 1515-1523.

[2] Romanos, G.E., Likodimos, V., **Marques, R.R.N.**, Steriotis, T.A., Papageorgiou, S.K., Faria, J.L., Figueiredo, J.L., Silva, A.M.T., Falaras, P. (2011) Controlling and Quantifying Oxygen Functionalities on Hydrothermally and Thermally Treated Single-Wall Carbon Nanotubes. The Journal of Physical Chemistry C, 115, 8534-8546.

4.1 Results and discussion

Recently, nitric acid hydrothermal oxidation was developed in our group as a controllable and mild functionalization method to tailor the surface chemistry of carbon xerogels [1] by the thermally activated generation of oxygen functional groups, whose density correlated analytically with the HNO_3 concentration. In the present work, the surface functionalization of commercial SWCNTs grown by catalytic chemical vapor deposition (CCVD) is drawn to tailor the introduction of oxygen functionalities using the same previously mentioned HNO_3 hydrothermal oxidation procedure, as described in detail in Section 2.1.1 of Chapter 2.

4.1.1 Identification of the nature of surface functionalities by water adsorption/desorption

At first glance, the results of water adsorption/desorption isotherms shown in Figure 4.1 illustrate that HNO_3 hydrothermal treatment truly modifies SWCNT's surface, since the range of water uptake is enhanced about three times. The presence of acidic surface groups with affinity to the water phase is in line with the high amount of water adsorbed, ca. 500 µmol/g as confirmed later by Temperature Programmed Desorption (TPD) quantification, on the surface of SWCNTs treated with the highest HNO_3 concentration of 0.3 mol L^{-1}, even after keeping the sample for 24 h under high vacuum (10^{-5} mbar) conditions.

The adsorption capacity could also be influenced by the filling of the micropores and the adsorption of water on nonacidic surface sites, however studies on water immersion calorimetry with carbon surfaces show that the enthalpy variation corresponding to the aforementioned interactions are minor compared to those between water molecules and oxygen groups such as carboxyls, lactones, quinones and carboxylic anhydrides [2]. Nevertheless, adsorption experiments with other probe molecules on CSI reference material (see Experimental section 4.3) lead to conclude that the contribution of micropores in the water adsorption of the CSI sample is negligible (results not shown).

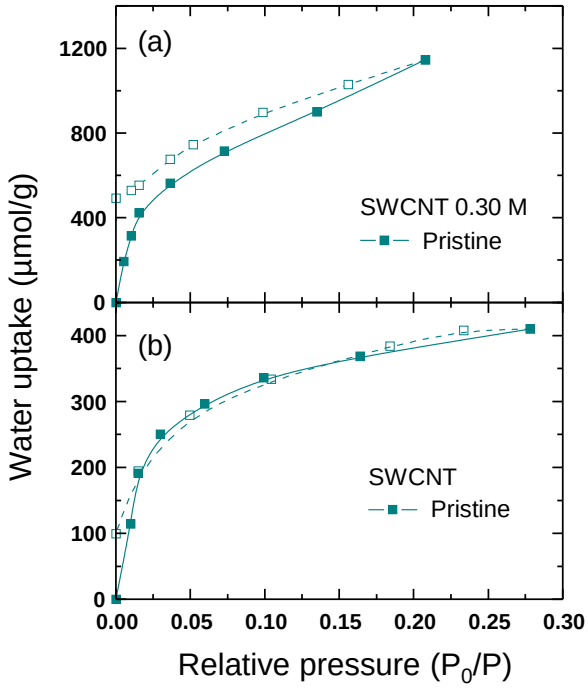

Figure 4.1 – Water vapor adsorption/desorption isotherms for the (a) SWCNTs treated with 0.3 mol L^{-1} of HNO_3 and (b) pristine SWCNTs samples. Full symbols: adsorption; open symbols: desorption.

Therefore, it can be inferred that water adsorption on the functionalized SWCNTs is highly specific, depending primarily on the degree of functionalization and can be used as a tool to quantify and, possibly, qualify oxygen surface functionalities on SWCNTs. In particular, the amount of water adsorbed upon completion of the monolayer can be related to the total content of the acidic surface groups, whereas the amount of water remaining adsorbed after evacuation can be associated with the most acidic ones among the different oxygen groups on the SWCNTs surface.

4.1.2 Identification and quantification of surface functionalities by Temperature Programmed Desorption

The distinct oxygen groups that are chemically bonded to the surface of CNTs upon oxidizing treatments, represented in Figure 4.2, can be decomposed upon heating at different temperatures and released as CO or CO_2 [3, 4].

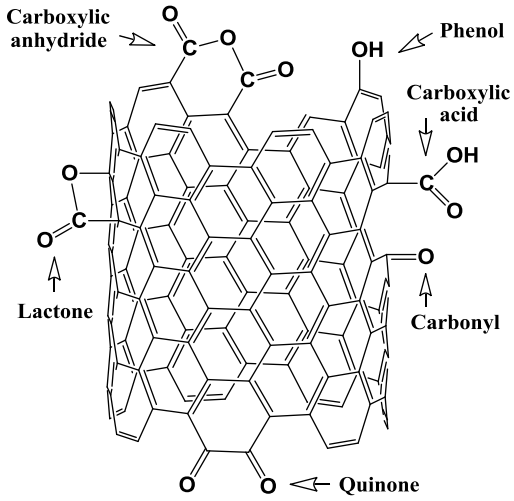

(a)

Figure 4.2 – Oxygen-containing functional groups: schematic representation.

In Figure 4.3 a and b are represented the TPD spectra corresponding to the groups evolved as CO and CO_2, respectively, from the surface of SWCNTs, pristine and treated under different HNO_3 concentrations at 473 K.

The amount of oxygen functionalities introduced on the surface of SWCNTs is strongly dependent on the concentration of HNO_3. Comparing the curves obtained for the pristine SWCNTs and for the blank test carried out with water instead of HNO_3, it is visible that no considerable amount of groups is present at the surface. This indicates that the introduction of oxygen-containing groups is totally ascribed to the presence of nitric acid instead of some effect of water at high temperatures. By increasing the oxidizing conditions, the amount of groups evolved as CO and CO_2 continuously increases. Both Figure 4.3 a and b suggest a good correlation between the concentration of the oxygen functionalities and the concentration of HNO_3. The measured concentrations of CO and CO_2 for both temperatures tested are gathered on Table 4.1.

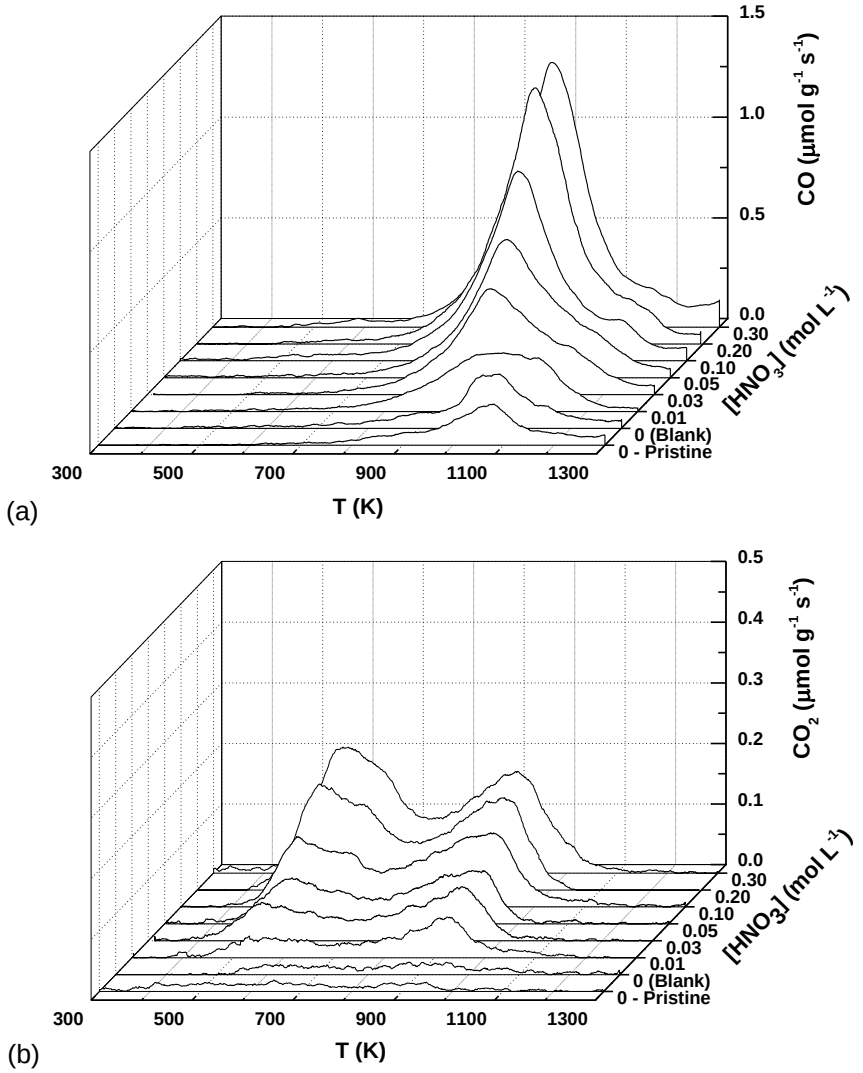

Figure 4.3 – TPD spectra for the pristine SWCNTs and treated under different HNO_3 concentrations at 473 K: (a) CO and (b) CO_2 release.

In the TPD spectra the amount of groups evolved as CO is considerably higher than that evolved as CO_2. Accordingly, the ratio CO/CO_2 was always higher than unity. This ratio generally decreases with increasing HNO_3 concentrations.

Table 4.1 – Total amount of CO and CO_2 calculated from the TPD spectra obtained for different HNO_3 concentrations (393 and 473 K).

$[HNO_3]$ (mol L^{-1})	393 K			473 K		
	CO (μmol g^{-1})	CO_2 (μmol g^{-1})	CO/CO_2	CO (μmol g^{-1})	CO_2 (μmol g^{-1})	CO/CO_2
Prist.SWCNT	545	90	6.0	545	90	6.0
0 (Blank)	756	75	10.1	714	89	8.1
0.01	661	125	5.3	1034	232	4.5
0.03	---	---	---	1541	350	4.4
0.05	705	109	6.5	1917	388	4.9
0.10	689	120	5.8	2407	586	4.1
0.20	781	173	4.5	3000	724	4.1
0.30	879	158	5.6	3148	907	3.5

To quantify the correlation between the amount of oxygen groups and the HNO_3 concentration used, the area under the spectrum was plotted against the HNO_3 concentration. In Figure 4.4 the two curves obtained for CO and CO_2 are represented. In addition, in order to test the influence of temperature on the functionalization process, the range of HNO_3 concentrations used at 473 K was also tested over pristine SWCNTs at 393 K and the results are shown in the same figure.

It becomes clear that the functionalization degree not only depends on the HNO_3 concentration but also on the temperature used. Surface groups are not introduced on SWCNTs at 393 K even at the highest HNO_3 concentrations tested. The present results suggest that activation energy is controlling the process, requiring a certain temperature to initiate the functionalization of SWCNTs. For the temperature of 473 K, the experimental data are well fitted by a single-exponential function, as shown in Figure 4.4.

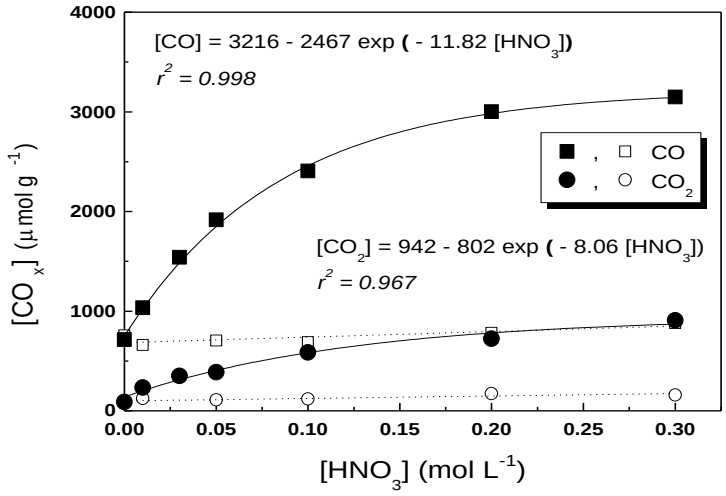

Figure 4.4 – Evolution of the amount of CO and CO_2 with HNO_3 concentration: open symbols – 393 K; solid symbols – 473 K (for mathematical correlations $[HNO_3]$ must be inserted in mol L^{-1} for a $[CO_x]$ in μmol g^{-1}).

Comparing the results obtained in this work with those previously obtained in our group for a carbon xerogel using the same functionalization method [1], a similar behavior is observed, suggesting that activation energy must be truly associated with the functionalization process. In that study a maximum functionalization degree is attained for 393 K but, when increasing the temperature for 473 K, the concentration of oxygen functionalities introduced on the surface of the carbon xerogel also increases and no plateau was observed for the highest HNO_3 concentrations.

By temperature deconvolution of the TPD spectrum for CO and CO_2 is possible to quantify the amount of oxygen functional groups present in the samples [3, 4]. It is relevant to point out that for the deconvolution process some assumptions are necessary according to the method reported in literature [4]. For instance, carboxylic anhydrides are supposed to decompose both as CO and CO_2. Once determined the peak parameters at which these groups were released as CO_2, an identical peak on the CO spectrum was defined. The concentration of each group is determined by calculating the area under the curve of the correspondent peak. As an example, Figure 4.5 a and b show the TPD spectra for the SWCNTs that were treated under the highest HNO_3 concentration (0.30 mol L^{-1}) and their respective deconvolution to obtain the distinct peaks from the decomposition of acidic carboxylic groups, carboxylic anhydrides, lactones, phenols and carbonyl/quinones.

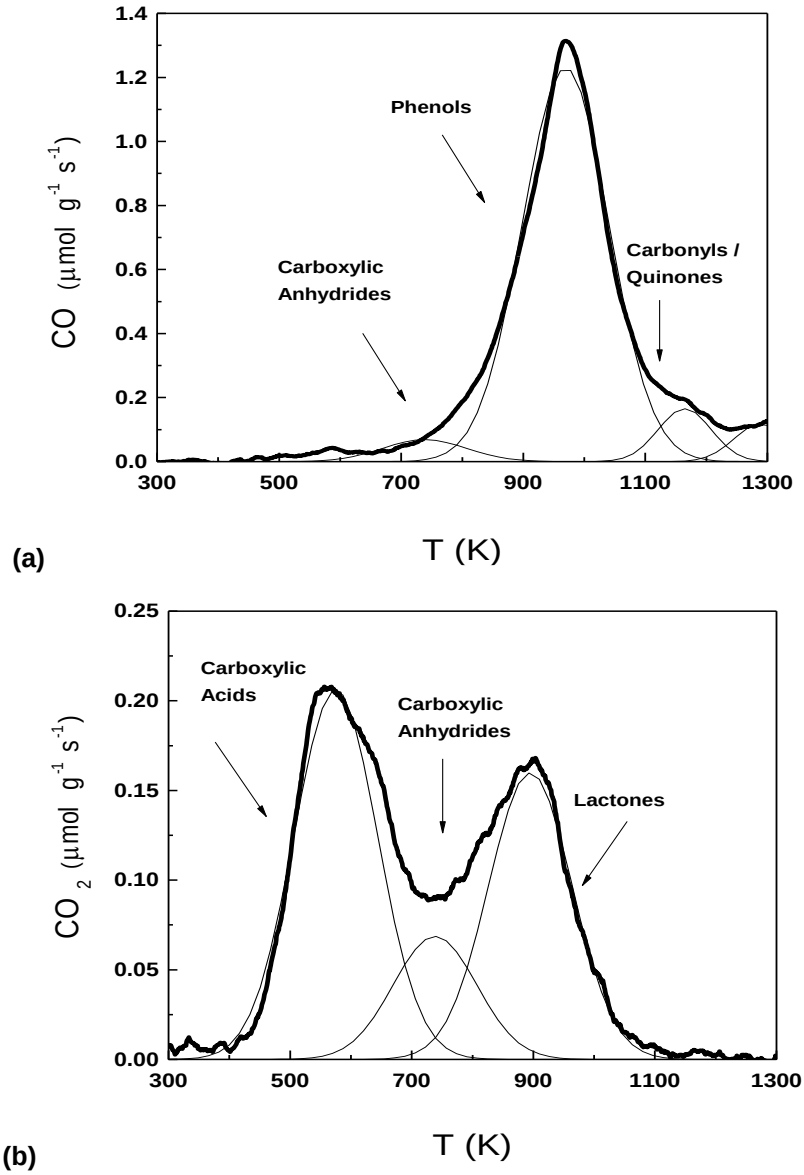

Figure 4.5 – Oxygen-containing functional groups: deconvolution of TPD-MS spectra for the SWCNTs treated with 0.3 mol L^{-1} of HNO_3 at 473 K (a) CO and (b) CO_2 spectra.

The main groups identified in the CO_2 spectra were carboxylic acids and lactones, while the most abundant functional groups determined from the CO spectra were phenols, indicating a high degree of hydroxylation upon hydrothermal HNO_3 oxidation. The concentrations determined for individual oxygen-containing functional groups on selected samples are shown in Table 4.2.

Table 4.2 – Quantification of oxygen functional groups by TPD-MS analysis as a function of the nitric acid concentration.

$[HNO_3]$ (mol L^{-1})	phenols (μmol g^{-1})	carbonyl/ quinones (μmol g^{-1})	carboxylic anhydrides (μmol g^{-1})	lactones (μmol g^{-1})	carboxylic acids (μmol g^{-1})
Prist.SWCNT	336	66	< 35	< 35	< 35
0.03	1074	376	127	160	126
0.10	1876	270	226	239	219
0.20	2524	262	312	326	360
0.30	2628	214	315	340	400

All the original TPD spectra curves (Figure 4.3) were deconvoluted using the same abovementioned approach and the release as CO and CO_2 is, respectively, represented as a function of the HNO_3 concentration in Figure 4.6 a and b.

For every HNO_3 concentration studied, the main groups identified on CO_2 spectra were carboxylic acids and lactones and the oxygen functions observed at the highest concentrations on the surface of SWCNTs were phenols, released as CO. Also carbonyls/quinones were identified on CO spectra, but in lower amounts. Carboxylic anhydrides were present in the lowest quantities, identified both on CO and CO_2 spectra.

As found for the total amount of groups at the surface of SWCNTs, an exponential function also fits the results obtained for the concentration of each single oxygen moiety (not shown). It is relevant to note that the concentration of all functionalities increase with HNO_3 concentration except for the carbonyl/quinones groups. The mechanism proposed in the literature reports that the formation of oxygen-containing surface groups seems to follow a progressive pathway starting with the creation of phenols (-OH) and carbonyl/quinones (C=O) being further developed into carboxylic functionalities (-COOH) if the material is exposed to oxidizing conditions for enough time to allow the conversion reaction [5-7]. Under our oxidizing conditions, the development of phenols is notorious and, the formation of carboxylic groups seems to result from the conversion of the carbonyl/quinones firstly created at the surface of the SWCNTs.

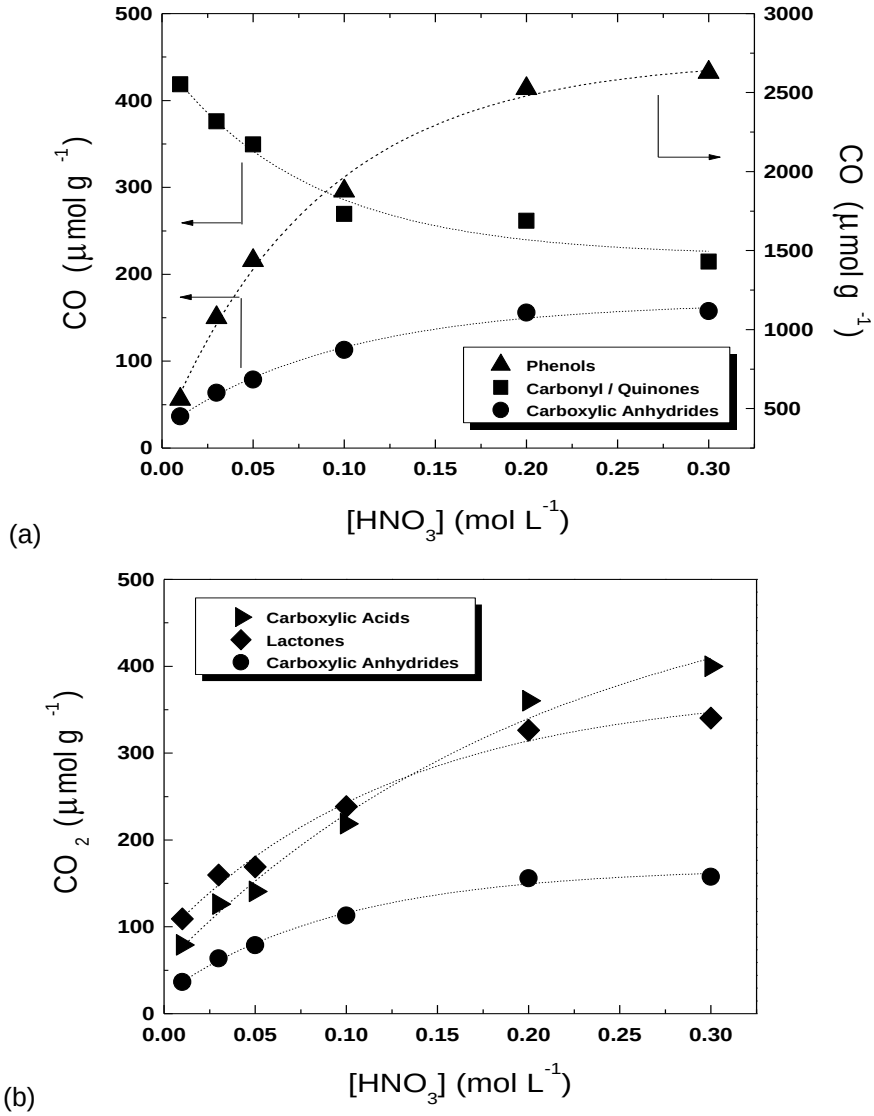

Figure 4.6 – Evolution of specific oxygen groups concentration created at the SWCNTs surface under HNO_3 treatment at 473 K, released as (a) CO and (b) CO_2.

The weight percentage of the amount of molecular oxygen released (% O_2) as CO and CO_2 was calculated based on the concentrations determined by TPD analysis. The results are gathered in Table 4.3 for 393 and 473 K.

Table 4.3 – Volatiles, ash content (determined by TGA) and % O_2 (determined by TPD) quantified for the pristine and treated SWCNT with different HNO_3 concentrations (393 and 473 K).

[HNO_3] (mol L^{-1})	393 K			473 K		
	% O_2 (wt. %)	% Volatiles	% Ash Content	% O_2 (wt. %)	% Volatiles	% Ash Content
Prist.SWCNT	1.2	7.0	6.9	1.2	7.0	6.9
0 (Blank)	1.4	10.2	6.6	1.4	9.3	8.6
0.01	1.5	10.0	6.1	2.4	10.2	5.5
0.03	---	---	---	3.6	12.3	4.5
0.05	1.5	9.3	7.0	4.3	13.3	3.1
0.10	1.5	12.1	6.3	5.7	15.8	3.3
0.20	1.8	---	---	7.1	18.5	3.1
0.30	1.9	12.9	6.3	7.9	19.2	3.4

The total amount of molecular O_2 is representative of the total concentration of oxygen groups introduced on the surface of SWCNTs. As expected, the trend of the O_2 released corroborates the TPD results. For the temperature of 393 K, no considerable surface modification was observed. On the other hand, at 473 K, the total amount of oxygen groups increases progressively with the HNO_3 concentration (Figure 4.7). Despite the poor surface chemistry of pristine SWCNTs with an O_2 concentration of 1.2 wt.%, the HNO_3 hydrothermal treatment is able to produce a considerable surface modification, introducing 7.9 wt.% of molecular O_2 at the strongest oxidizing conditions tested (0.3 mol L^{-1} of HNO_3).

Weight percentage of volatiles and ash content were determined by Thermogravimetric Analysis (TGA) and the results gathered in Table 4.3. The temperature of 393 K is insufficient to modify the surface of the CNTs and to remove the ash content present in the material. Since volatiles correspond mainly to the oxygen functionalities that are released during TGA, the results at 473 K are once again fitted to a single-exponential function and follow the same trend as found for the evolution of molecular oxygen (Figure 4.7). The difference observed between the

amount of volatiles and the molecular oxygen can be related to some nitrogen functionalities that contribute to the weight loss during TGA but are not measured as CO or as CO_2 during TPD analysis. At variance to what happened at 393 K, the HNO_3 treatment at 473 K was able to remove up to 50% of the ash content of pristine SWCNTs (Table 4.3). The ash content decreased from 6.9% for the original material to around 3.1-3.4% for SWCNTs treated with HNO_3 concentrations above 0.05 mol L^{-1}. Therefore, temperature and HNO_3 concentration are key parameters for the activation of the functionalization process as well as for the removal of the inorganic material that remains in the samples from the synthesis of SWCNTs, produced by CCVD.

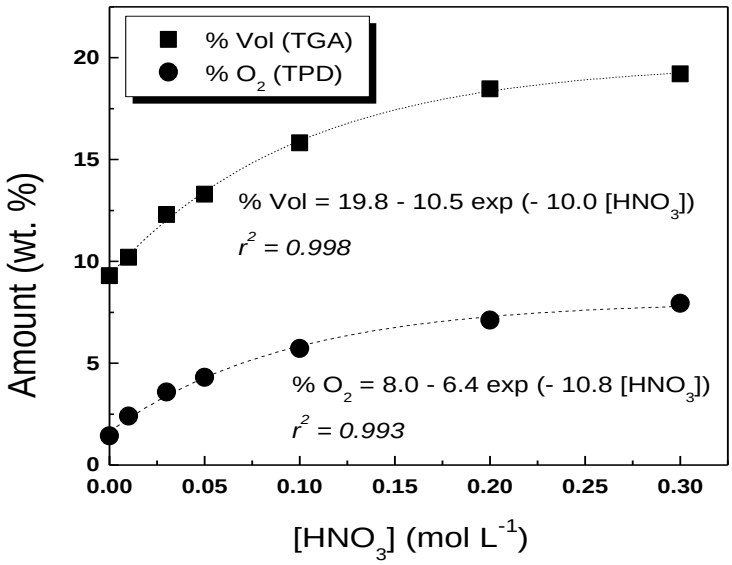

Figure 4.7 – Amount of volatiles (determined by TGA) and molecular O_2 (determined based on TPD spectra) present at the surface of SWCNT treated with different HNO_3 concentrations at 473 K (for mathematical correlations [HNO_3] must be inserted in mol L^{-1}).

When comparing SWCNTs with carbon xerogels in terms of functionalization by using the same method and experimental conditions, it is noticeable that the functionalization degree in terms of % O_2 is about 2.5 times higher for carbon xerogels (at a concentration of 0.3 mol L^{-1} HNO_3). As previously discussed, the difference observed may be ascribed to the structural properties of the materials.

CNTs are very well organized carbon materials with ordered graphite layers and thus poor reactive due to the high chemical stability. In this case, the introduction of oxygen functionalities proceeds over the defects that are introduced during HNO_3 hydrothermal treatment. On the other hand, carbon xerogels are structures with a totally distinct morphology, like a bulk material with a developed porosity. In this case, the carbon structure is not so organized like in CNTs, thus providing more sites for the attachment of the oxygen moieties. Therefore, the reactivity of carbon xerogels is supposed to be much higher than the one of CNTs, which can explain the difference on the functionalization degrees achieved with the current HNO_3 hydrothermal treatment. However, in both cases, the % O_2 is correlated with the HNO_3 concentration by an exponential function as presented for SWCNTs in Figure 4.7.

During each HNO_3 hydrothermal run, it was verified that the SWCNTs weight loss (WL) varied significantly with the conditions used. The WL is computed from the difference between the weight of SWCNTs introduced into the autoclave (0.2 g, in this case) and the final weight of the recovered material after the HNO_3 hydrothermal treatment, normalized to the initial weight in percentage. In Figure 4.8 the WL is represented as a function of HNO_3 concentration for both 393 and 473 K.

For the temperature of 393 K, the WL variation observed with increasing HNO_3 concentration is negligible. However, at 473 K the oxidizing conditions are such that the WL varies significantly with the used HNO_3 concentration (up to 50%). As observed for the amount of oxygen functionalities introduced on the surface of SWCNTs, an exponential function fits the WL experimental data, suggesting that both phenomena are related. In fact, during the acidic oxidation process, CNTs can collapse and form carboxylated carbonaceous fragments (CCFs). It is reported that the carboxylated functions produced by HNO_3 treatment are mainly on CCFs adsorbed on SWCNTs instead of directly covalently anchored to the surface of SWCNTs [8, 9]. Under strong enough oxidizing conditions these CCFs can be fully gasified to form CO_2, which can explain the verified WL.

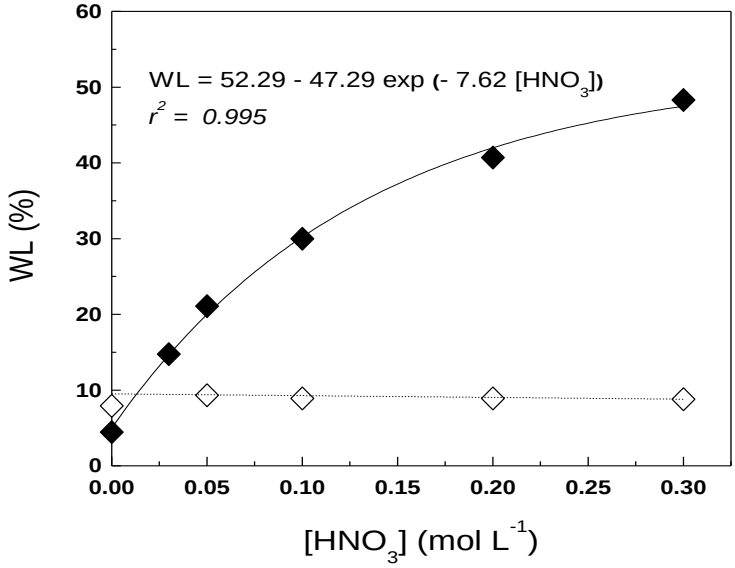

Figure 4.8 – Weight Loss observed after the HNO_3 treatment at different concentrations: open symbols – 398 K; solid symbols – 473 K (for mathematical correlations [HNO_3] must be inserted in mol L^{-1}).

In the case of the carbon xerogel, the reported WL during the same HNO_3 hydrothermal treatment did not exceed 10% under the same conditions [1]. Since the WL of the SWCNTs verified during the blank test (with water instead of HNO_3) was in the range of the measured values for the carbon xerogel (5-10%), it is believed that the mechanism undergone by both materials during the exposure to the HNO_3 oxidizing conditions for this same HNO_3 hydrothermal process is different. Therefore, there are many aspects in the HNO_3 hydrothermal treatment that influence the mechanism and the yield of oxygen functionalities introduced over their surface. Reaction temperature and HNO_3 concentrations are the key operation conditions to tune the functionalization of these carbon materials. In addition, when choosing a carbon material for a certain application that requires previous surface functionalization, the morphology is also a relevant issue since the reaction pathway appears to go in different ways.

Additional tests performed by loading the reactor with 0.5 g of SWCNTs instead of 0.2 g and using three different HNO_3 concentrations (0.03, 0.1 and 0.3 mol L^{-1}) lead to the CO and CO_2 concentrations gathered in Table 4.4, as along with the % O_2. As expected, for the groups released as CO and for the groups released as CO_2, the

amount of surface groups obtained with the same HNO_3 concentration is always lower for the load of 0.5 g.

Table 4.4 – Total amount of CO and CO_2 calculated from the TPD spectra and respective % O_2 as function of $[HNO_3]/m_{SWCNT}$ and HNO_3 concentration at 473 K.

$[HNO_3]$ (mol L^{-1})	m_{SWCNT} (g)	$[HNO_3] / m_{SWCNT}$ (mol L^{-1} g^{-1})	CO (μmol g^{-1})	CO_2 (μmol g^{-1})	CO/CO_2	% O_2 (wt. %)
0.03	0.5	0.06	1134	184	6.2	2.4
0.03	0.2	0.15	1541	350	4.4	3.7
0.10	0.5	0.20	1888	428	4.4	4.4
0.10	0.2	0.50	2407	586	4.1	5.9
0.30	0.5	0.60	2535	606	4.2	6.2
0.30	0.2	1.50	3148	907	3.5	8.4

In Figure 4.9 is plotted the percentage of the total amount of molecular oxygen determined by TPD (released as CO and CO_2) against $[HNO_3]/m_{SWCNT}$ for all the SWCNTs loads and HNO_3 concentrations studied at 473 K.

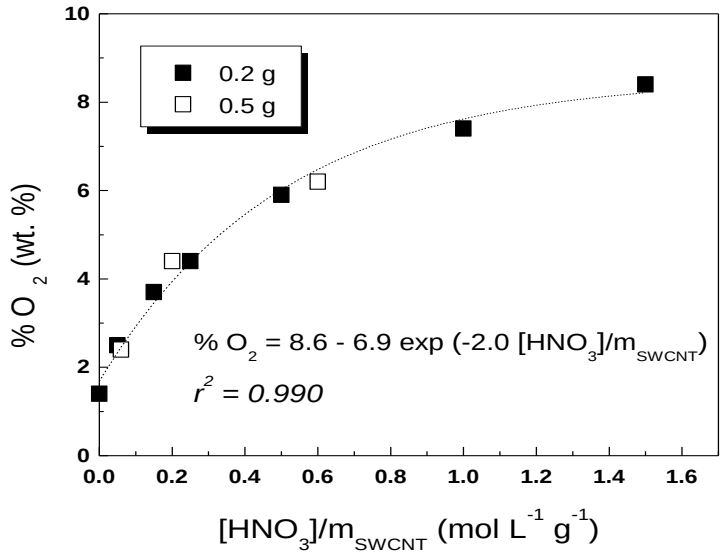

Figure 4.9 – Amount of molecular oxygen present as oxygen groups on the surface of SWCNTs treated at 473 K as a function of $[HNO_3]/m_{SWCNT}$.

As expected, the % O_2 is dependent on the $[HNO_3]/m_{SWCNT}$ ratio. In addition, since one single mathematical correlation fits quite well the data for both loads (0.2 g and 0.5 g), for a given $[HNO_3]/m_{SWCNT}$ ratio, the % O_2 seems to be independent with respect to the SWCNTs load (i.e., when the HNO_3 concentration increases proportionally to the SWCNTs load in order to maintain the $[HNO_3]/m_{SWCNT}$ ratio). Therefore, a mathematical correlation between the amount of oxygen groups which can be introduced at the surface of SWCNTs and the $[HNO_3]/m_{SWCNT}$ ratio is established. The functionalization degree can now be predicted not also for a fixed load of SWCNTs but for the whole range of $[HNO_3]/m_{SWCNT}$ studied, including several SWCNTs loads and HNO_3 concentrations. Thus, using the obtained mathematical correlations can accurately control the surface modification of SWCNTs by the HNO_3 hydrothermal method.

4.1.3 Structural modifications on hydrothermally treated SWCNTs: surface area and pore size distribution

The amount of oxygen-containing groups introduced on the surface of carbon xerogels was higher than that attained with the SWCNTs using the same temperature and HNO_3 concentrations. Moreover, the difference between the two materials increased with the HNO_3 concentration, for identical oxidizing conditions. This trend is intrinsically related on the distinct morphology of both carbon materials. It is worth noting that the concept of porosity is quite different when considering carbon xerogels or carbon nanotubes. Carbon xerogels present a type of porosity similar to that of well-known activated carbons. The available area for the introduction of the oxygen functionalities is on the micro, meso and macropores. The porosity of CNTs is usually associated to a bundle and not to a single carbon nanotube, since the graphite layers are non-porous. The porosity of a bundle of CNTs is the result of different contributions [10]: (i) the area available at the surface of the bundle, (ii) the existing area between distinct individual carbon nanotubes, which is called interstitial and (iii) the area inside the pores of the bundle, which corresponds to the inner cavities of the opened CNTs. The degree of functionalization must then always be compared taking into account the specific morphology of each material.

The N_2 adsorption–desorption isotherms of the pristine and treated SWCNTs at 473 K under four different HNO_3 concentrations are represented in Figure 4.10 and the respective BET surface areas were calculated from these isotherms.

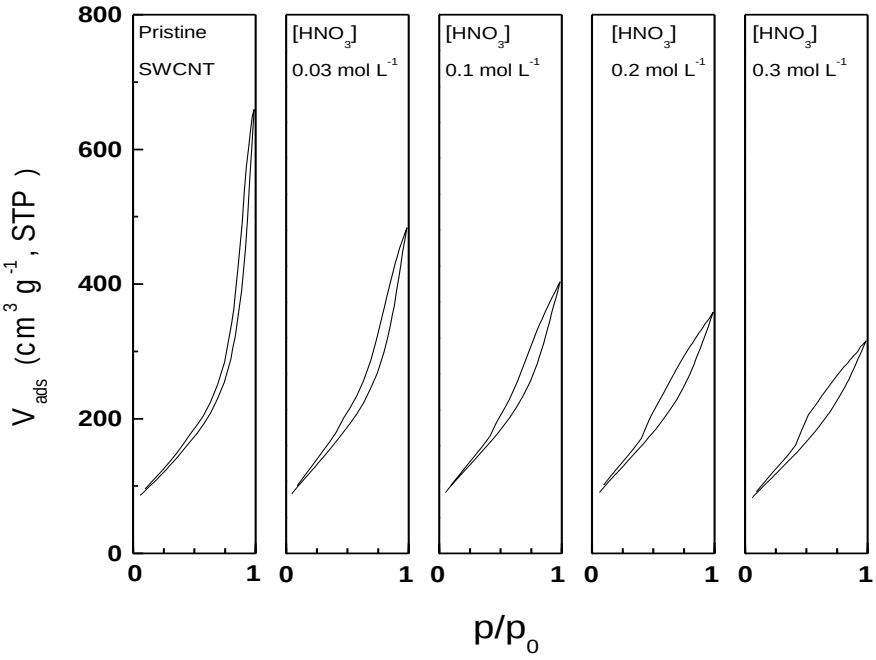

Figure 4.10 – Nitrogen adsorption isotherms for the original and treated SWCNT with different HNO_3 concentrations at 473 K.

The materials treated with different HNO_3 concentrations present similar BET surface areas varying less than 5% with relation to the original material (406 $m^2 g^{-1}$). In accordance with the IUPAC classification [11], the observed isotherms are classified as Type IV developing to Type I for the highest HNO_3 concentrations. It is known from the literature [12, 13] that the adsorption capacity of SWCNTs decreases with the presence of surface functional groups and structural defects. Figure 4.10 shows that the N_2 uptake at higher p/p_0 relative pressures decreases with the increase of the HNO_3 concentration used. This seems to be related to the amount of oxygen-containing groups and structural defects generated on the SWCNTs surface at high HNO_3 concentration.

Before determination of the N_2 adsorption isotherm the samples are degassed for 6 h at 573 K under vacuum. In order to confirm that oxygen groups are still present on the SWCNTs surface after the degasification procedure, reducing the adsorption capacity, the TPD spectra were compared for the SWCNTs treated with 0.2 mol L^{-1} of HNO_3 before and after N_2 adsorption isotherm analysis. Only 3% of oxygen functionalities were removed during the procedure used to determine N_2 adsorption

isotherms, confirming that the surface groups can be responsible by the observed decrease on the N_2 uptake.

Esteves et al. [13] developed a procedure to obtain information about the surface area and the porosity of SWCNTs bundles. Type I isotherms are related with the filling up of the tubes with adsorbate while the other types of isotherms are associated with adsorption on the external surface of the bundles. Accordingly, the results presented in Figure 4.10 lead to the conclusion that the hydrothermal treatment has a significant influence on the external surface of SWCNTs and little or no effect on their internal surface.

When the acidic treatment was carried out over carbon xerogels [1], the area increased about 30% when high HNO_3 concentrations were used and this was ascribed to the development of the microporosity during the functionalization process. In the case of the carbon xerogel, the introduction of the oxygen-containing groups took place over all the available surface area, whereas for CNTs the defects created at the surface of the graphite layers are the single positions which present some chemical reactivity to form the desired functionalities.

Therefore, the nature of the carbon material should be taken into account when predicting the functionalization degree to be achieved with the HNO_3 hydrothermal treatment.

The pore size distributions (PSDs) obtained by Quenched Solid Density Functional Theory (QSDFT) of the pristine and functionalized SWCNT samples are presented in Figure 4.11. All PSDs reveal a “dual” pore system consisting of micropores (pore widths 0.7 - 0.9 nm) and a rather broad distribution of mesopores. This bimodal pore texture is consistent with the interstitial space between individual nanotubes (micropores), while the mesopores originate from the packing of the nanotube bundles (mesopores). A straightforward observation on the effect of acid treatment on the pore structure is that upon oxidation (and thus incorporation of functional groups) there is a monotonic decrease of the mesopores volume. In fact, while the mean mesopores average size remains constant (around 2.8 nm) the amount of larger pores diminishes rapidly, even under mild oxidation conditions of 0.03 mol L^{-1} of HNO_3, and the mesopores size distribution becomes narrower toward smaller sizes.

This effect can be explained on the basis of more efficient packing/organization of the SWCNTs bundles upon introducing functional groups, presumably due to excess hydrogen bonding. Indeed, it has been reported that surface functionalities promote

the stronger aggregation of the CNTs bundles [14, 15]. In the case of micropores, it is obvious (Figure 4.11 b) that even a mild acid treatment (0.03 or 0.10 mol L^{-1}) shifts microporosity to smaller sizes (0.93 to 0.85 nm), the shift being more pronounced at stronger oxidative conditions (0.20, 0.30 mol L^{-1}). This smaller size can be related to the chemical enrichment of the outer surface that facilitates individual SWCNTs to pack closer to each other and create more dense bundles. In Figure 4.11, it can be also observed that the micropore volume increases significantly after mild treatment (0.03, 0.10 mol L^{-1}). However, stronger oxidation leads to a decrease of the micropore volume compared to the pristine sample probably due to the stereochemical hindrance imposed by the large number of functional groups.

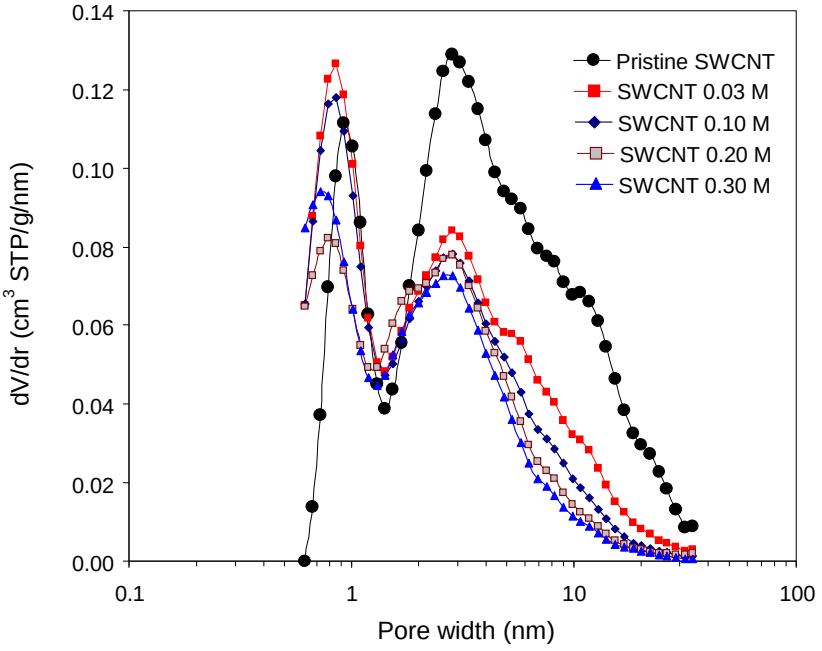

(a)

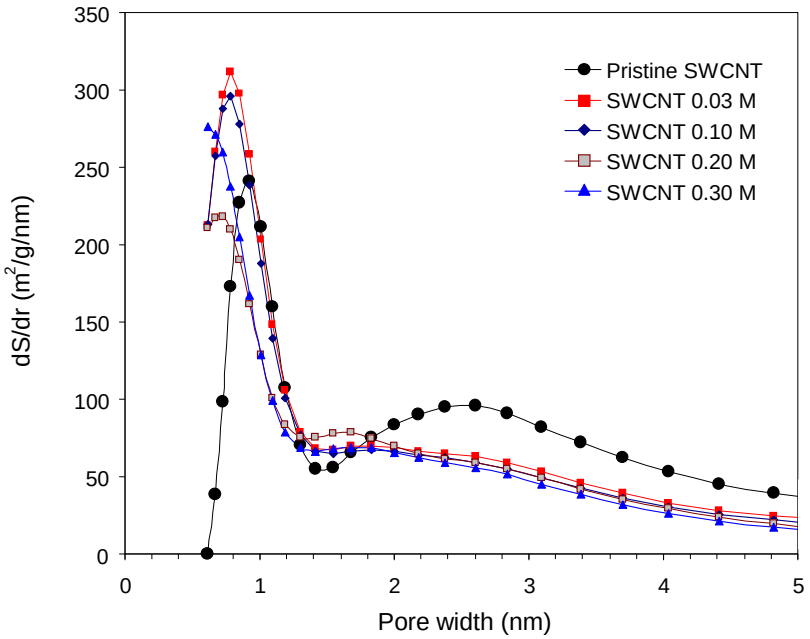

(b)

Figure 4.11 – Volume (a) and surface area (b) QSDFT PSDs of the hydrothermally treated SWCNTs samples as a function of the HNO_3 concentration.

The PSD of the air-treated sample (Figure 4.12) reveals a significant reduction of the mesopore volume with a simultaneous increase of microporosity. This variation shows that surface carboxylic groups facilitate SWCNTs' assembly to more dense bundles, creating thus excess microporosity.

On the other hand, Ar treatment leads to the removal of the existing functional groups and decreases the micropore volume, while the mesopore volume undergoes a less intense reduction.

This behavior is consistent with the removal of surface functional groups, which may lead to (a) partial collapse of the porous system under heating, (b) reduced interaction potential between the "pure" graphitic walls and nitrogen molecules, or (c) weakening of attractive forces between the SWCNT bundles that tend to aggregate in a rather loose configuration with interbundle void spaces of size that is above the upper limit of the QSDFT N_2 method (~40 nm).

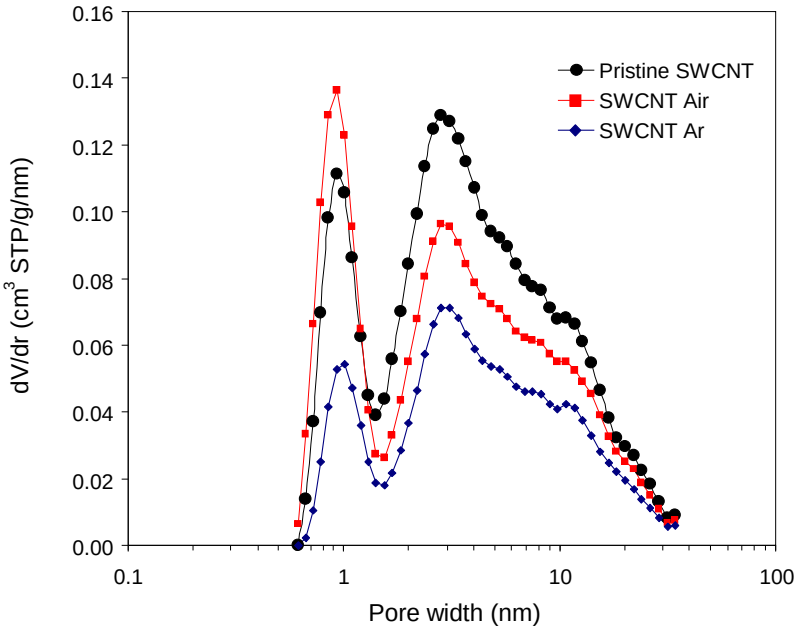

Figure 4.12 – Volume QSDFT PSDs of the pristine SWCNTs in comparison with the air- (300 ºC) and Ar-treated (500 ºC) analogues.

4.1.4 Identification of charge transfer effects by resonance Raman spectroscopy

The effect of the functional groups on the SWCNTs surface was investigated by Raman spectroscopy at two different excitation wavelengths in the NIR (785 nm) and visible range (514.5 nm). Figure 4.13 a and b shows the evolution of the Raman spectra for the hydrothermally treated samples in the spectral range of 1200 – 1900 cm^{-1}, where the first-order tangential G modes and the highly dispersive defect-induced D band are observed at 514.5 and 785 nm, respectively.

The contribution of elastic scattering from defects together with one phonon inelastic scattering has been successfully applied to explain the origin of the D-band and its excitation dependence based on double resonant Raman scattering [16], rendering this mode the characteristic fingerprint of structural disorder in graphitic materials [17].

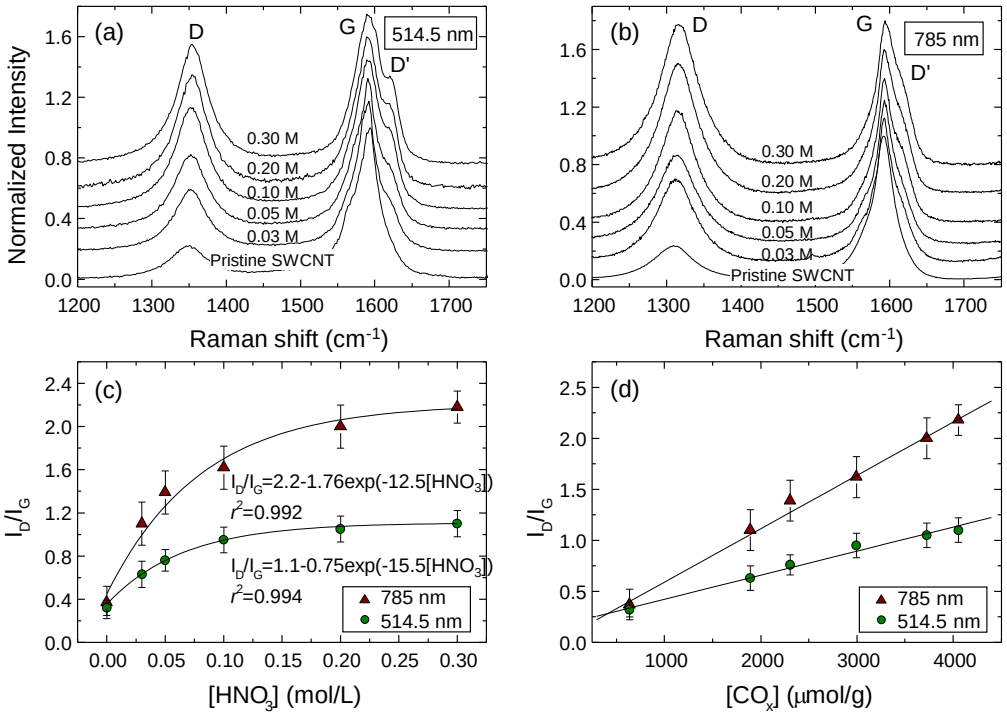

Figure 4.13 – Raman spectra of the hydrothermally treated SWCNTs samples at (a) 514.5 and (b) 785 nm. Variation of the I_D/I_G intensity ratio as a function of (c) $[HNO_3]$ and (d) $[CO_x]$ concentrations. Lines designate the corresponding exponential and linear best fit curves to the I_D/I_G vs $[HNO_3]$ and $[CO_x]$, respectively.

Specifically, the intensity ratio I_D/I_G between the integrated areas of the D and G bands has been long exploited as a measure of the in-plane crystallite size of nanographites [18], while recently it has been quantitatively related to the average distance between defects in covalently functionalized SWCNTs [19] and Ar^+ ion-irradiated graphene [20].

The Raman spectra of the oxidized samples reveal a marked dependence of the dispersive D band (1350 cm^{-1}, ~48 cm^{-1}/eV) with $[HNO_3]$ at both excitation wavelengths, as shown in Figure 4.13 a and b. The relative intensity of the D-band with respect to that of the tangential G-band increases rapidly with the increase of the nitric acid concentration, following the concomitant increase of the amount of oxygen functionalities on the SWCNTs. Moreover, at high HNO_3 concentrations (>0.05 mol L^{-1}), the defect-induced D' band at ~1620 cm^{-1}, originating from a similar double resonance process as the D-band, can be clearly resolved, especially at 514.5 nm, indicating the increase of structural disorder on the CNTs [17].

Quantification of this variation through the integrated intensity ratio I_D/I_G shows that the experimental data can be well fitted to a single exponential function as a function of the HNO_3 concentration (Figure 4.13 c). The corresponding exponent values depend on the laser excitation energy, resembling the excitation laser dependence of the I_D/I_G ratio in nanographites [17] and functionalized SWCNTs [19]. This variation closely follows the evolution of the concentration of surface groups determined by the amount of CO and CO_2 released during TPD [21]. Most importantly, plotting I_D/I_G as a function of the total amount of functional groups, quantified by $[CO_x] = [CO] + [CO_2]$, reveals a linear scaling of I_D/I_G with the defect concentration (Figure 4.13 d), while a similar correlation can be found with the water adsorption/desorption results. This indicates that the I_D/I_G ratio can provide a quantitative probe of the total amount of oxygen functional groups on the SWCNTs surface at these defect concentration levels.

Figure 4.14 a compares the Raman spectra of the pristine and the fully functionalized SWCNT 0.30 M samples up to higher frequencies at 514.5 nm, where the overtones and combination modes of SWCNTs are clearly observed. The dominant feature in the second order Raman spectra, is the highly dispersive (~109 cm^{-1}/eV) G' band corresponding to the overtone of the D-band (2D). The G' band originates from a two-phonon double resonance process that is, in principle, independent of disorder [17]. However, near-field Raman measurements have recently identified an additional defect-induced G' peak at higher/lower frequencies near defect sites spatially resolved along individual SWCNTs, due to the defect-induced renormalization of the electron and phonon energies [22].

In the present case, a gradual shift of the G' band is systematically observed toward higher frequencies with the increase of the HNO_3 concentration, reaching 16 cm^{-1} for the SWCNT 0.30 M sample (inset of Figure 4.14 a), in qualitative agreement with the acceptor action (hole doping) of oxygen functional groups [23]. However, the presence of two distinct G' peaks could not be reliably resolved, as the strong dependence of the G' mode on tube diameter, metallicity and excitation energy can be effectively averaged for SWCNTs bundles [24].

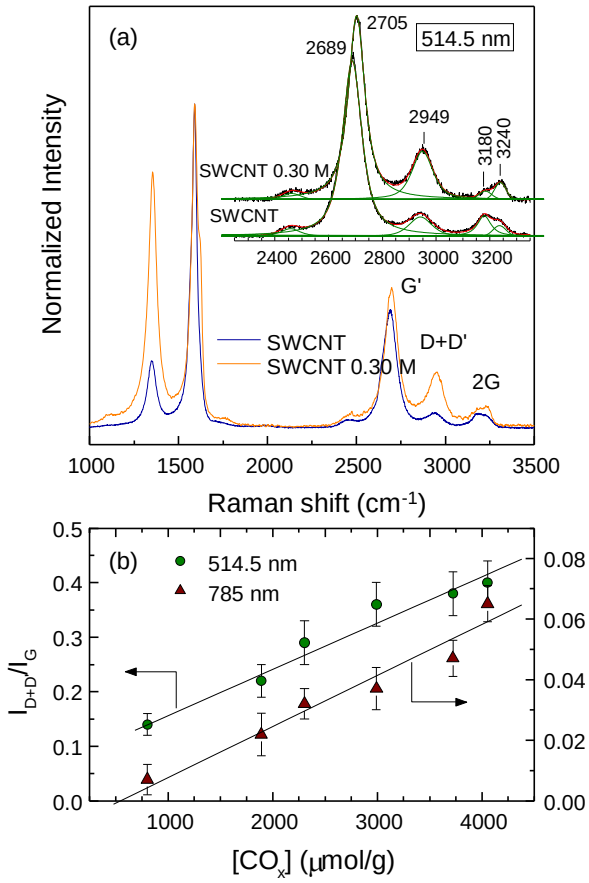

Figure 4.14 – (a) Raman spectra of the pristine and SWCNT 0.30 M samples in the high frequency region at 514 nm. The inset shows the spectral analysis (green-red lines) of the G', D + D' and 2G modes (black lines). (b) Variation of the $I_{D+D'}/I_G$ intensity ratio with $[CO_x]$ at 514.5 and 785 nm.

On the other hand, the relatively weak band at ~2950 cm^{-1} exhibits a pronounced dependence on HNO_3 concentration. This band has been recently attributed to the combination of the two defect-induced modes D+D' [19, 25] instead of the usual D+G assignment [26], based on the strong enhancement of its intensity with increasing concentration of chloro-phenyl groups on SWCNTs [19]. Calculation of the ratio between the integrated areas of the D+D' mode and the tangential G band ($I_{D+D'}/I_G$) reveals a strong, almost linear dependence of $I_{D+D'}/I_G$ on the defect density (Figure 4.14 b). A similar variation of $I_{D+D'}/I_G$ versus $[CO_x]$ is obtained at 785 nm, where, however, the relative intensity of the D+D' mode is drastically reduced. This behavior verifies the strongly defect-induced origin of the 2950 cm^{-1} mode [19]. Moreover, at

higher frequencies, an intriguing double peak structure is observed at ~3200 cm^{-1}, where the first overtone of the G-band is expected. Deconvolution of this composite band reveals two individual peaks at approximately 3180 and 3240 cm^{-1} (inset of Figure 4.14 a). The former corresponds closely to the second harmonic of the tangential G band (~1590 cm^{-1}), frequently identified in SWCNTs [27], while the latter is consistent with the corresponding shifted variant in graphitic materials and multi-walled CNTs (MWCNTs) due to the overbending of the graphite phonon dispersion curves [28]. Calculation of the corresponding intensity ratios I_{3180}/I_G and I_{3240}/I_G versus $[CO_x]$ concentration reveals a counter-dependence of the intensity of the two peaks with increasing concentration of the oxygen functional groups, i.e., a decrease (increase) of I_{3180}/I_G (I_{3240}/I_G) with $[CO_x]$. The intensification of the 3240 cm^{-1} mode correlates well with the enhancement of the defect-induced D' band with increasing HNO_3 concentration. The evolution of these two features may then be associated with the formation of CCFs or even the presence of MWCNTs, as indicated by the relatively lower SWCNT purity (> 60%).

Furthermore, the presence of small amounts of MWCNTs or even few-walled CNTs (FWCNT) in the SWCNTs samples (SWCNT purity > 60%), generally characterized by a higher D band intensity due to their inherently more defective structure, may effectively compromise the averaged Raman spectra on the powder samples. In that case, the contribution of functionalized MWCNTs and FWCNTs that are more resistant to the exfoliation into CCFs under nitric acid treatment [8], might promote the formation of the defect-induced D' band (Figure 4.13) or the splitting of the 2G overtone (Figure 4.14) in the SWCNT samples.

The location of the oxygen functional groups on the CNTs has been subsequently explored by Raman spectroscopy on the thermally treated SWCNTs and SWCNT 0.30 M samples in air and argon atmosphere at 300 and 500 ºC, respectively (Figure 4.15). Mild oxidative treatment in air results in significant decrease of the relative D-band intensity for the SWCNT 0.30 M sample at both excitation wavelengths, leading to the decrease of I_D/I_G to 1.3(1) and 0.7(1) at 785 and 514.5 nm, respectively. These values are approximately 35% lower than those of the fully functionalized SWCNT 0.30 M sample (Figure 4.13 d), verifying that an appreciable portion of the D-band intensity stems from amorphous carbon and CCFs, which are oxidized at 300 ºC. On the other hand, the persistence of substantial D band intensity after mild air oxidation suggests that a significant amount of oxygen functionalities remains or becomes attached on the CNTs surface rather than on CCFs, in agreement with the results of water adsorption/desorption analysis. This is

further supported by the variation of the I_D/I_G ratio upon thermal treatment of the SWCNT 0.30 M sample in inert atmosphere at 500 ºC, where it decreases to 1.0(1) and 0.5(1) at 785 and 514.5 nm, respectively.

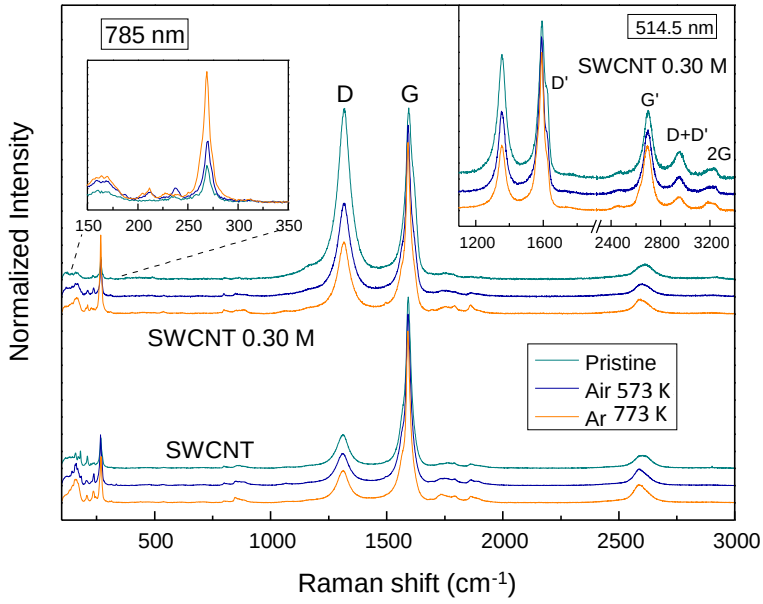

Figure 4.15 – Raman spectra of the Pristine and SWCNT 0.30 M samples thermally treated in air and Ar atmosphere at 573 and 773 ºC, respectively, in comparison with the corresponding spectra of the pristine samples at 785 nm. The left inset depicts the variation of the radial breathing modes for the SWCNT 0.30 M sample, while the right inset shows the corresponding Raman spectra at 514.5 nm.

The latter treatment is expected to decompose the more acidic groups on the SWCNTs, while leaving intact amorphous carbon/CCFs and the less acidic functional groups such as phenols that are the most abundant species created during hydrothermal HNO_3 treatment. In that case, removal of the strong acidic functional groups to a larger extent results in the increased reduction of I_D/I_G, which is thus found to correlate mainly with the variation of the water desorption capacity of the thermally treated SWCNT 0.30 M sample.

Similar effects are also observed on the D' and D+D' bands most clearly resolved at 514.5 nm (right inset of Figure 4.15). Both bands become gradually suppressed upon air and Ar treatment, verifying their defect-induced origin and their dependence on the density of functional groups. Appreciable variations are also observed in the

characteristic first-order radial breathing modes (RBMs) at 785 nm (left inset of Figure 4.15). The SWCNTs samples consist of CNTs bundles with a broad distribution of diameters (<2 nm), to which the dominant peaks in the RBM frequency region occur at 267 cm^{-1} under 785 nm excitation. These RBMs arise from semiconducting SWCNTs [29]. Thermal treatment leads to a systematic increase of the relative RBM intensity, most pronounced for the 500 ºC Ar-treated SWCNT 0.30 M sample. This variation can be associated with the decomposition of strongly acidic groups and the concomitant recover of the resonance conditions, partially suppressed in the SWCNT 0.30 M sample through charge transfer [23, 30, 31]. Qualitatively similar, though minor, changes are also traced for the RBM bands of the thermally treated SWCNTs samples, whereas the defect-induced D and D+D' modes were hardly affected (the I_D/I_G ratio remains practically constant at both excitations), in agreement with the weak variation of its water adsorption/desorption capacity upon thermal treatment.

4.2 Conclusions

The controlled surface modification of SWCNTs was successfully performed by means of a HNO_3 hydrothermal functionalization method and the present study shows that a controlled functionalization can be achieved by setting with precision the HNO_3 concentration and the temperature. The observed dependency in temperature confirms that activation energy is controlling the functionalization process.

The combined analytical power of water adsorption/desorption, resonance Raman spectroscopy, TGA, TPD-MS and nitrogen porosimetry provides a sensitive means to measure and quantify oxygen functionalities on SWCNTs bundles subjected to both hydrothermal and thermal treatment. In addition explains the origin of the pore structure alteration as result of the functionalization conditions and properties of the pristine materials.

By conducting water vapor adsorption-desorption isotherms in acidified SWCNTs, it was possible to discriminate the population of the high acidity carboxylic groups and correlate these findings with the TPD results. The method can be used to provide a rapid estimate on the amount of acidic groups attached to the surface of the CNTs, which are of particular interest for specific applications. However, this methodology may not be applicable for samples exhibiting high microporosity with pores in the

ultramicropore region, where the contribution of physisorption to the total monolayer capacity may be significant.

The functionalization degree on the surface of SWCNTs, studied through TPD analysis, is correlated with the HNO_3 concentration by a single-exponential function for the total amount of groups released as CO or CO_2 and can even be, in particular, numerically computed as function of the concentration of each oxygen specific group. In this way it can be used to consistently predict the functionalization results for each carbon material at defined HNO_3 concentrations.

Raman spectroscopy of the functionalized SWCNTs reveals a linear scaling of the defect-activated Raman mode intensity with the concentration of surface groups determined by TPD-MS and water adsorption-desorption measurements. In this way quantitative information extracted from Raman data can be correlated with the functionalization process. Distinct variations have been also identified in the first-order tangential and radial breathing Raman modes as well as the D and G band overtones of SWCNTs upon functionalization, reflecting the release of the resonance Raman condition caused by charge transfer and the underlying shift of the Fermi level, which depends on the amount and acidity of the oxygen functional groups as well as the SWCNT's chirality. Water adsorption-desorption and Raman measurements on thermally treated SWCNTs samples in air and argon atmosphere point to the formation of amorphous carbon, which depends on the aggressiveness of the oxidative conditions. However, a large fraction of the carboxylic groups that form upon acidification is concluded to remain attached on the SWCNT's surface rather than on the generated CCFs.

Analysis of the bimodal pore texture of SWCNTs by QSDFT calculations has shown that application of a soft acidification process results in the progressive decrease of the mesopore volume that correlates inversely with the acidity of the treatment solution. In addition, the micropore volume is shifted toward lower sizes. Both phenomena dictate more efficient packing/organization of the nanotube bundles and of individual CNTs upon the introduction of oxygen functional groups. Interesting enough is that the increase of the micropore volume exhibits a maximum in relation to the acidity of the solution. This variation evidences the optimum treatment above which the addition of more functional groups could stereochemically hinder the diffusion of gaseous molecules in the intertube space of SWCNTs bundles.

4.3 Experimental section

Pristine SWCNTs synthesized by Catalytic Chemical Vapor Deposition (CCVD) were purchased from Shenzhen Nanotechnologies Co. Ltd. (NTP) with the following manufacturer data: purity of CNT > 90%, purity of SWCNT > 50%, main range of diameter < 2 nm, length = 5-15 μm. The as received material will be referred as pristine SWCNTs.

Comparison was made with highly functionalized electric arc-discharge (EA) reference materials (CSI) from Carbon Solutions, Inc. (USA). CSI samples are characterized by the highest purity of most commercially available EA-SWCNTs (SWCNT purity > 90%) and a narrow distribution of diameters around 1.4 nm, while they are in a heavily functionalized state (~ 6 wt % of carboxylic acid groups) after oxidative treatment in concentrated HNO_3 [32, 33].

4.3.1 Single-Walled Carbon Nanotubes functionalization

The functionalization of SWCNTs followed an experimental procedure described in detail in Section 2.1.1 of Chapter 2. The CNTs (0.2 or 0.5 g) were immersed in HNO_3 solutions of different concentrations ranging from 0 – 0.3 mol L^{-1} in a pressurized autoclave at high temperature (393 or 473 K) during 2 h of operation.

4.3.2 Single-Walled Carbon Nanotubes characterization

Temperature Programmed Desorption (TPD) analysis was carried out using 0.1 g of each sample placed in a U-shaped quartz tube and heated at 5 K min^{-1} until reach the maximum temperature of 1273 K. The concentration of CO and CO_2 released was determined using the calibration performed at the end of each analysis and the experimental error was less than 8%.

The amount of volatiles, fixed carbon and ash content was assessed for each sample by Thermogravimetric Analysis (TGA). The samples were heated under a N_2 atmosphere to the final temperature of 1173 K allowing the calculation of the amount of volatile compounds at the surface and the amount of fixed carbon. After the gas feed was turned to O_2 the ash content is determined when a new stable weight was reached.

The materials texture was determined by N_2 adsorption-desorption isotherms at 77 K with calculation of the surface area based on the Brunauer, Emmett and Teller (BET)

theory, S_{BET}, determined by multipoint analysis in the relative pressure range from 0.05 to 0.3.

Other treatments and analytical techniques were performed in cooperation with the Institute of Advanced Materials, NCSR Demokritos, Greece.

Water vapor adsorption-desorption measurements were conducted on a microbalance with a 0.1 μg stable resolution. Before each measurement, the samples were degassed under high vacuum (10^{-5} mbar) at 180 ºC.

Mild oxidative and pyrolytic treatments in air and argon atmosphere were applied on the fully functionalized and pristine SWCNTs in order to determine the extent of amorphous carbon generation and the relative distribution of functional groups and CCFs. Argon treatment was performed with a ramp rate of 5 K min^{-1} up to the temperature of 773 K and an isothermal step of 30 min. For the air treatment the ramp rate was maintained at 2.5 K min^{-1} up to the temperature of 573 K followed by an isothermal step of 30 min.

Pore size distributions (PSDs) were obtained after using the Quenched Solid Density Functional Theory (QSDFT) N_2-carbon equilibrium transition kernel at 77 K of Quantachrome's Library [34].

Raman measurements were performed to assess structural morphologic changes at molecular level by applying an Ar^+ ion laser (λ = 514.5 nm, E = 2.41 eV) and a high power near-infrared (NIR) diode laser (λ = 785 nm, E = 1.58 eV) as excitation sources.

Detailed description of the applied conditions for every analytical technique mentioned before is explained in Chapter 3.

4.4 References

[1] Silva AMT, Machado BF, Figueiredo JL, Faria JL. Controlling the surface chemistry of carbon xerogels using HNO3-hydrothermal oxidation. Carbon. 2009; 47 (7):1670-9.

[2] López-Ramón MV, Stoeckli F, Moreno-Castilla C, Carrasco-Marín F. Specific and non-specific interactions of water molecules with carbon surfaces from immersion calorimetry. Carbon. 2000; 38 (6):825-9.

[3] Figueiredo JL, Pereira MFR, Freitas MMA, Órfão JJM. Modification of the surface chemistry of activated carbons. Carbon. 1999; 37 (9):1379-89.

[4] Figueiredo JL, Pereira MFR, Freitas MMA, Órfão JJM. Characterization of Active Sites on Carbon Catalysts. Ind Eng Chem Res. 2007; 46 (12):4110-5.

[5] Ros TG, van Dillen AJ, Geus JW, Koningsberger DC. Surface Oxidation of Carbon Nanofibres. Chem-Eur J. 2002; 8 (5):1151-62.

[6] Yang D-Q, Rochette J-F, Sacher E. Functionalization of Multiwalled Carbon Nanotubes by Mild Aqueous Sonication. J Phys Chem B. 2005; 109 (16):7788-94.

[7] Zhang J, Zou H, Qing Q, Yang Y, Li Q, Liu Z, et al. Effect of Chemical Oxidation on the Structure of Single-Walled Carbon Nanotubes. J Phys Chem B. 2003; 107 (16):3712-8.

[8] Yu H, Jin Y, Peng F, Wang H, Yang J. Kinetically Controlled Side-Wall Functionalization of Carbon Nanotubes by Nitric Acid Oxidation. J Phys Chem C. 2008; 112 (17):6758-63.

[9] Salzmann CG, Llewellyn SA, Tobias G, Ward MAH, Huh Y, Green MLH. The Role of Carboxylated Carbonaceous Fragments in the Functionalization and Spectroscopy of a Single-Walled Carbon-Nanotube Material. Adv Mater. 2007; 19 (6):883-7.

[10] Serp P, Corrias M, Kalck P. Carbon nanotubes and nanofibers in catalysis. Appl Catal A-Gen. 2003; 253 (2):337-58.

[11] Sing KSW, Everett DH, Haul RAW, Moscou L, Pierotti RA, Rouquerol J, et al. Reporting physisorption data for gas/solid systems with special reference to the determination of surface area and porosity (Recommendations 1984). Pure Appl Chem. 1985; 57 (4):603-19.

[12] Mawhinney DB, Naumenko V, Kuznetsova A, Yates Jr JT, Liu J, Smalley RE. Surface defect site density on single walled carbon nanotubes by titration. Chem Phys Lett. 2000; 324 (1–3):213-6.

[13] Esteves IAAC, Cruz FJAL, Müller EA, Agnihotri S, Mota JPB. Determination of the surface area and porosity of carbon nanotube bundles from a Langmuirian analysis of sub- and supercritical adsorption data. Carbon. 2009; 47 (4):948-56.

[14] Yang CM, Kim DY, Lee YH. Single-walled carbon nanotube network with bimodal pore structures of uniform microporosity and mesoporosity. J Nanosci Nanotechnol. 2005; 5 (6):970-4.

[15] Arai M, Kanamaru M, Matsumura T, Hattori Y, Utsumi S, Ohba T, et al. Pore characterization of assembly-structure controlled single wall carbon nanotube. Adsorpt. 2007; 13 (5-6):509-14.

[16] Thomsen C, Reich S. Double Resonant Raman Scattering in Graphite. Phys Rev Lett. 2000; 85 (24):5214-7.

[17] Pimenta MA, Dresselhaus G, Dresselhaus MS, Cancado LG, Jorio A, Saito R. Studying disorder in graphite-based systems by Raman spectroscopy. Phys Chem Chem Phys. 2007; 9 (11):1276-90.

[18] Tuinstra F, Koenig JL. Roman spectrum of graphite. J Chem Phys. 1970; 53 (3):1280-1.

[19] Fantini C, Pimenta MA, Strano MS. Two-Phonon Combination Raman Modes in Covalently Functionalized Single-Wall Carbon Nanotubes. J Phys Chem C. 2008; 112 (34):13150-5.

[20] Lucchese MM, Stavale F, Ferreira EHM, Vilani C, Moutinho MVO, Capaz RB, et al. Quantifying ion-induced defects and Raman relaxation length in graphene. Carbon. 2010; 48 (5):1592-7.

[21] Marques RRN, Machado BF, Faria JL, Silva AMT. Controlled generation of oxygen functionalities on the surface of Single-Walled Carbon Nanotubes by HNO3 hydrothermal oxidation. Carbon. 2010; 48 (5):1515-23.

[22] Maciel IO, Anderson N, Pimenta MA, Hartschuh A, Qian H, Terrones M, et al. Electron and phonon renormalization near charged defects in carbon nanotubes. Nat Mater. 2008; 7 (11):878-83.

[23] Zhou W, Vavro J, Nemes NM, Fischer JE, Borondics F, Kamarás K, et al. Charge transfer and Fermi level shift in *p*-doped single-walled carbon nanotubes. Phys Rev B. 2005; 71 (20):205423.

[24] Kalbac M, Kavan L, Farhat H, Kong J, Dresselhaus MS. Large Variety of Behaviors for the Raman G′ Mode of Single Walled Carbon Nanotubes upon Electrochemical Gating Arising from Different (n,m) of Individual Nanotubes. J Phys Chem C. 2009; 113 (5):1751-7.

[25] Nemanich RJ, Solin SA. First- and second-order Raman scattering from finite-size crystals of graphite. Phys Rev B. 1979; 20 (2):392-401.

[26] Tan P, An L, Liu L, Guo Z, Czerw R, Carroll DL, et al. Probing the phonon dispersion relations of graphite from the double-resonance process of Stokes and

anti-Stokes Raman scatterings in multiwalled carbon nanotubes. Phys Rev B. 2002; 66 (24):245410.

[27] Dresselhaus MS, Dresselhaus G, Saito R, Jorio A. Raman spectroscopy of carbon nanotubes. Phys Rep. 2005; 409 (2):47-99.

[28] Thomsen C. Second-order Raman spectra of single and multiwalled carbon nanotubes. Phys Rev B. 2000; 61 (7):4542-4.

[29] O'Connell MJ, Sivaram S, Doorn SK. Near-infrared resonance Raman excitation profile studies of single-walled carbon nanotube intertube interactions: A direct comparison of bundled and individually dispersed HiPco nanotubes. Phys Rev B. 2004; 69 (23):235415.

[30] Itkis ME, Perea DE, Jung R, Niyogi S, Haddon RC. Comparison of Analytical Techniques for Purity Evaluation of Single-Walled Carbon Nanotubes. J Am Chem Soc. 2005; 127 (10):3439-48.

[31] Kavan L, Kalbáč M, Zukalová M, Dunsch L. Electrochemical Doping of Chirality-Resolved Carbon Nanotubes. J Phys Chem B. 2005; 109 (42):19613-9.

[32] Hu H, Zhao B, Itkis ME, Haddon RC. Nitric Acid Purification of Single-Walled Carbon Nanotubes. J Phys Chem B. 2003; 107 (50):13838-42.

[33] Itkis ME, Perea DE, Niyogi S, Rickard SM, Hamon MA, Hu H, et al. Purity Evaluation of As-Prepared Single-Walled Carbon Nanotube Soot by Use of Solution-Phase Near-IR Spectroscopy. Nano Lett. 2003; 3 (3):309-14.

[34] Neimark AV, Lin Y, Ravikovitch PI, Thommes M. Quenched solid density functional theory and pore size analysis of micro-mesoporous carbons. Carbon. 2009; 47 (7):1617-28.

5 MWCNTs functionalization by hydrothermal oxidation

Controlled surface functionalization of multi-walled carbon nanotubes by HNO_3 hydrothermal oxidation[3]

Given the structural differences between SWCNTs and MWCNTs, with a predictable higher resistance for the latter to post effects of oxidation treatments and the significantly lower costs for mass production, the potential of nitric acid hydrothermal oxidation was systematically explored for their controlled functionalization. Two types of commercially available MWCNTs, grown by catalytic chemical vapor deposition, with largely different morphological characteristics (diameter and length) were compared. The same conditions were reproduced from the previously tested with the SWCNTs. The effectiveness on the creation of surface oxygen-functionalities was compared based on the results obtained with temperature programmed desorption coupled with mass spectrometry from which was possible to identify and quantify the groups created at the surface. Further detailed characterization was carried out to evaluate the occurred structural modifications by thermogravimetry and differential scanning calorimetry, Raman spectroscopy and N_2 porosimetry analysis (Institute of Advanced Materials, NCSR Demokritos, Greece). Comparison was made with the commonly used boiling acid methods, revealing that hydrothermal oxidation is a competitive methodology to efficiently modify CNTs surface using much lower amounts of oxidizing agent and reducing amorphous carbon deposits on CNTs surface. On the other hand, boiling acid methods provide higher amounts of the carboxylic acid functionalities on MWCNTs surface, which are of particular interest on the progress of this research, namely in the synthesis of CNT composite materials for photocatalytic applications.

[3] Likodimos, V., Steriotis, T.A., Papageorgiou, S.K., Romanos, G.Em., **Marques, R.R.N.**, Rocha, R.P., Faria, J.L., Pereira, M.F.R., Figueiredo, J.L., Silva, A.M.T., Falaras, P. (2014) Controlled surface functionalization of multiwall carbon nanotubes by HNO_3 hydrothermal oxidation, Carbon, 69, 311-326.

5.1 Results and discussion

Commercially available Multi-Walled Carbon Nanotubes (MWCNTs) grown by catalytic chemical vapor deposition (CCVD) with different morphologies, regarding diameter and length, were studied and compared to the SWCNTs discussed in the previous Chapter 4 with basis on the extent of surface functionalization and subsequent structural modifications after being oxidized through the same hydrothermal HNO_3 oxidation method. The results were compared with those obtained with the aggressive oxidation of CNTs in concentrated HNO_3 at boiling temperature. Experimental conditions used on the oxidation treatments are given in detail in Sections 2.1.1 and 2.1.2 of Chapter 2. Information about the CNTs involved in this work can be found in Experimental section 5.3.

5.1.1 Identification and quantification of oxygen groups

Figure 4.1 displays the Temperature Programmed Desorption (TPD) spectra arising from specific oxygen groups released as CO and CO_2 from the surface of the hydrothermally treated NTX3 MWCNTs (see Experimental section 5.3), as a function of the HNO_3 concentration. These results are obtained by coupling TPD to mass spectrometry (MS). The TPD profiles measured for the pristine NTX3 material and for the blank experiment in the absence of HNO_3 are also included for comparison. Qualitatively similar TDP spectra were acquired for the thin and narrow NC3100 MWCNTs (see Experimental section 5.3) under identical HNO_3 concentrations as for the NTX3, though using higher amount (0.5 g) of NC3100 material (not shown).

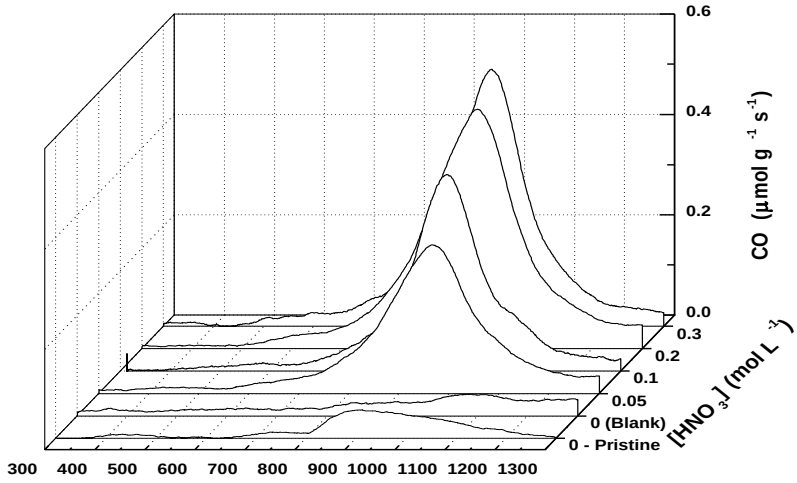

(a)

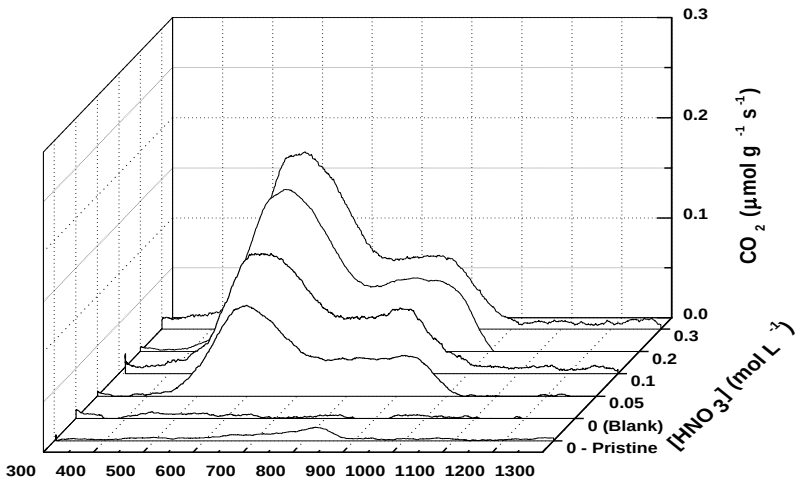

(b)

Figure 5.1 – TPD spectra for the pristine and hydrothermally treated NTX3 MWCNTs at different HNO_3 concentrations and 473 K: (a) CO and (b) CO_2 release.

To quantify the relationship between oxygen groups and HNO_3 concentrations, the total amount of surface groups released as CO and CO_2 was determined from the area under the corresponding TPD spectra (Table 5.1). The weight percentage of the total amount of molecular oxygen released as CO and CO_2 (wt.% O_2), which is representative of the total amount of oxygenated groups introduced on the CNT surface, was calculated based on the amounts determined by the TPD analysis.

Table 5.1 - Total amount of CO, CO_2 and wt.% O_2 calculated from the TPD spectra obtained for the hydrothermally functionalized NTX3 different HNO_3 concentrations and 473 K.

$[HNO_3]$ (mol L^{-1})	CO (±20) (µmol g^{-1})	CO_2 (±20) (µmol g^{-1})	CO/CO_2	O_2 (wt.%)
0 – Pristine	218	43	5.12	0.5
0 (Blank)	278	23	12.3	0.5
0.05	946	304	3.11	2.5
0.10	1156	482	2.40	3.4
0.20	1463	545	2.68	4.1
0.30	1573	662	2.38	4.6
7.0 (Boiling)	1344	751	1.79	4.6

Pristine NTX3 materials comprised low amounts of surface groups leading to a low amount of released wt.% O_2. Furthermore, hydrothermal treatment without nitric acid was verified to cause negligible effects on the poor surface chemistry of the pristine NTX3 MWCNTs. On the other hand, hydrothermal treatment in the presence of nitric acid resulted in a marked increase of the release of both CO and CO_2 that depended strongly on the HNO_3 concentration, as shown in Figure 5.2.

Previous studies [1] have pointed out that oxygen containing groups are not created on the surface of SWCNTs when hydrothermal oxidation is performed at a lower temperature (393 K), the two key parameters of the functionalization process being the temperature and HNO_3 concentration. However, pressure during hydrothermal treatment may also promote surface group kinetics and the homogenous generation of oxygen functional groups within the MWCNTs layers, as inferred from their low thermal stability (Section 5.1.2).

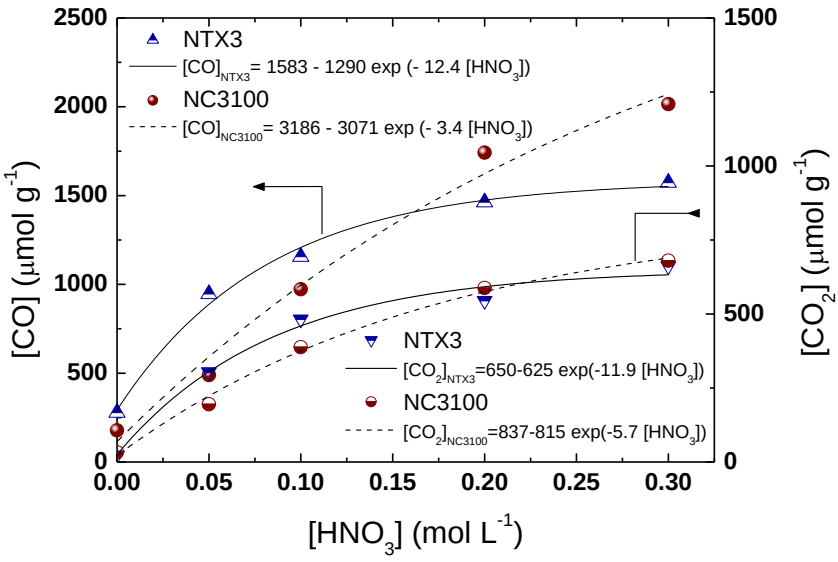

Figure 5.2 - Evolution of the amount of CO and CO_2 released from the surface of the hydrothermally treated NTX3 and NC3100 MWCNTs vs. the HNO_3 concentration.

In addition, a single exponential function was found to describe analytically the evolution of CO and CO_2 amounts with the HNO_3 concentration, in qualitative agreement with the results obtained for hydrothermally treated SWCNTs [1, 2], and

carbon xerogels [3]. This shows that oxygen surface functionalization of both MWCNTs and SWCNTs can be accurately controlled through the hydrothermal methodology regardless of the structural differences between them and the different amounts of surface groups introduced on the CNT's surface. However, despite the qualitatively similar evolution of oxygen functionalities on the hydrothermally treated materials, the degree of oxygen functionalization as monitored by the CO, CO_2 and CO/CO_2 dependence on [HNO_3], varied appreciably for the two different types of MWCNTs. In fact, the amounts of oxygen groups released as CO and CO_2 for NC3100 exceeded significantly the corresponding ones of NTX3 at HNO_3 concentrations above 0.1 mol L^{-1} (Table 5.1). This difference is further augmented if we take into account the higher loading of NC3100 MWCNTs (0.5 g) that would be expected to effectively decrease the amount of oxygen functionalities on the MWCNT surface at the same HNO_3 concentration. These distinct differences between NTX3 and NC3100, indicate that the nanotube morphology and particularly the MWCNT's diameter and length, which differ considerably between the two types of CCVD tubes, are critical parameters for the extent of surface functionalization by the HNO_3 hydrothermal process. Furthermore, comparison with the corresponding results on hydrothermally treated SWCNTs [1] shows that the degree of surface functionalization of the MWCNTs is systematically lower, especially for NTX3, where the amount of groups released as CO is nearly two times lower for all the HNO_3 concentrations.

Although the TPD profiles of the hydrothermally treated MWCNTs are similar to the corresponding ones of SWCNTs, the CO/CO_2 ratios for the MWCNTs (< 3.11) are considerably lower than those of the SWCNTs (> 3.50) [1], implying that the generation of surface groups released as CO_2 with respect to CO is favored on the MWCNTs surface in comparison with SWCNTs. In typical liquid phase functionalization methods with acids, the CO/CO_2 ratio tends to decrease with the increase of the concentration of the oxidizing agent due to the introduction of more acidic groups on the CNTs surface that are released as CO_2. This implies the formation of relatively more acidic groups, in comparison to basic groups, on the surface of MWCNTs than on SWCNTs oxidized under similar conditions. In order to further assess the interplay between the efficiency of hydrothermal oxidation for CNTs surface functionalization and the intrinsic materials properties, the total amount of molecular oxygen released from the materials' surface (wt.% O_2) was compared for both types of MWCNTs, NTX3 and NC3100, including previous results on

hydrothermally treated SWCNTs (S_{BET} ~ 400 m^2 g^{-1} for SWCNTs) [1] as a function of the $[HNO_3]/m_{CNT}$ ratio, which is independent of the CNTs loading (Figure 5.3).

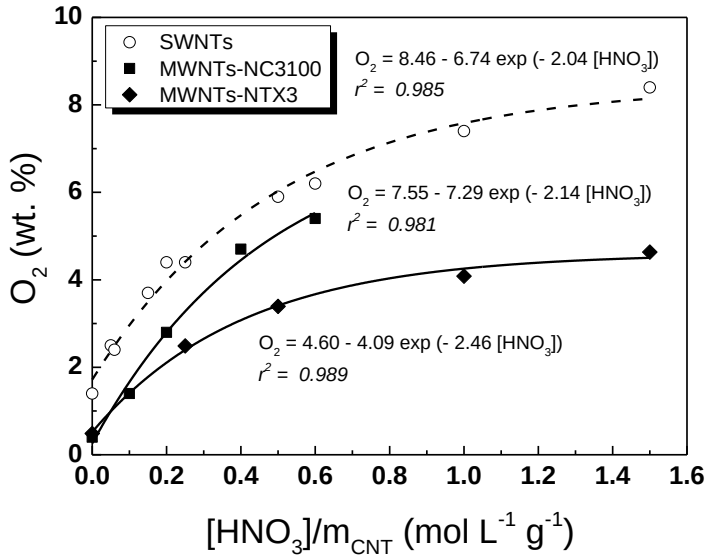

Figure 5.3 - Amount of molecular oxygen present as oxygen groups in the surface of SWCNT, NC3100 and NTX3 as a function of the $[HNO_3]/m_{CNT}$ ratio.

In fact, it has been proved that the wt.% O_2 for two different loadings of SWCNTs (namely 0.2 and 0.5 g) scale consistently, when plotted as a function of the $[HNO_3]/m_{CNT}$ ratio [1], which may thus serve as common scale for the comparison of functionalized CNTs by the hydrothermal oxidation methodology.

The $[HNO_3]$ dependence of the amount of molecular O_2 was thus found to vary considerably for the different types of CNTs, the most pronounced differences occurring between NC3100 and NTX3. In particular, the short and thin (length of ~ 1.5 µm and diameter of ~ 10 nm) NC3100 MWCNTs were functionalized to a considerably higher extent than the much longer (>10 µm) and thicker (diameter in the range of 25-40 nm) NTX3 nanotubes, in accordance with the respective BET surface area of the pristine materials (S_{BET} ~ 300 and 80 m^2 g^{-1} for NC3100 and NTX3, respectively), i.e. a higher functionalization is obtained for MWCNTs with higher surface area. This confirms that the CNTs morphology and especially the MWCNT's diameter and length and the concomitant variation of the surface area, dictate to a large extent the degree of surface functionalization. Additionally, regarding both NTX3 and SWCNTs, Figure 5.3 shows a plateau for the wt.% O_2 evolution at the higher $[HNO_3]/m_{CNT}$ ratios, which was not observed for the NC3100 samples since

only lower $[HNO_3]/m_{CNT}$ ratios were tested in this particular case. The total amount of CO and CO_2, as well as the $[HNO_3]/m_{CNT}$ ratio, were also normalized to the BET surface area of each sample (i.e. CO + CO_2/S_{BET} vs. $[HNO_3]/m_{CNT}/S_{BET}$, not shown). The amount of groups per surface area were thus found to be slightly higher for SWCNTs in comparison to NC3100, corroborating that the surface of the longer and thinner SWCNTs is more easily oxidized than that of the shorter and thicker MWCNT NC3100. However, the CO + CO_2/S_{BET} ratio for a given $[HNO_3]/m_{CNT}/S_{BET}$ was higher for NTX3 than for the other two materials, even if the total amount of groups introduced in these MWCNTs is much lower (Figure 5.3), indicating that NTX3 offers less (but more reactive) sites for surface functionalization.

To explore further the modification of the MWCNT's surface chemistry by hydrothermal oxidation, the nature of the distinct functional groups and their amounts were determined as function of the HNO_3 concentration by deconvolution of the CO and CO_2 TPD spectra following the procedure previously developed for activated carbons [4, 5]. All spectra were deconvoluted and the amount of each group (determined by calculating the area under the correspondent peak) is presented as a function of the HNO_3 concentration in Figure 5.4.

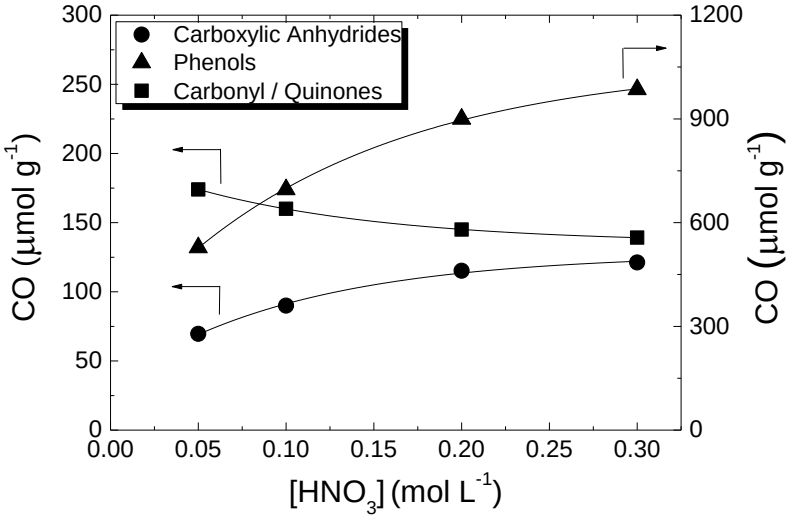

(a)

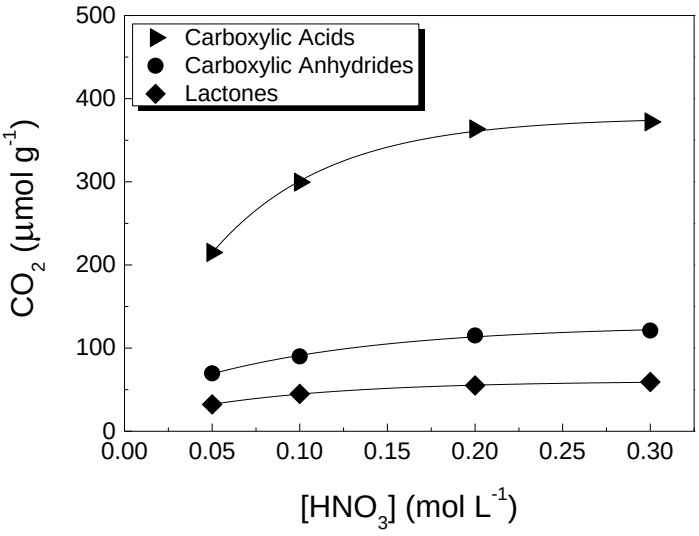

(b)

Figure 5.4 - Evolution of the amount of specific oxygen groups created at the surface of the hydrothermally treated NTX3 with the HNO_3 concentration released as CO (a) and CO_2 (b).

Phenols were the main groups released as CO and carboxylic acids those released as CO_2. Carbonyls/quinones and lactones were also identified by the deconvolution of the CO and CO_2 spectra, respectively, while carboxylic anhydrides were identified on both CO and CO_2 spectra. In addition, an exponential analytic function was found to fit well the [HNO_3] dependence of the amount of each single oxygen moiety (not shown), as found for the total amount of groups on the surface of MWCNTs (Figure 5.2). The amount of all identified surface groups increased with the HNO_3 concentration except for carbonyl/quinone functionalities. As reported in the previous Section 4.1.2 of Chapter 4 for SWCNTs, the proposed mechanism for the creation/evolution of oxygen surface groups on CNTs is based on a progressive pathway where the carbonyl/quinone groups (C=O) are formed and further transformed into phenolic (-OH) and carboxylic (-COOH) functionalities [6-9]. Under the conditions applied in the present work, the amount of carbonyl/quinones functionalities decreased with the increase of the HNO_3 concentration for NTX3 MWCNTs, suggesting that the development of phenolic and carboxylic surface groups could in fact result from the conversion of carbonyl/quinones initially created on the MWCNTs' surface. The same tendencies of groups and their evolution were verified for the NC3100 MWCNTs (results not shown).

Furthermore, comparison between the two types of MWCNT showed that the generation of both phenols and carboxylic groups was markedly enhanced for NC3100, confirming that this material offers more sites for surface functionalization compared with the long and large diameter NTX3 MWCNTs. Moreover, the amount of carboxylic anhydrides for MWCNTs was comparable (NTX3) or even higher (NC3100) than that estimated for SWCNTs at the same conditions [1]. Regarding the other surface groups, the amounts of carbonyl/quinones, phenols and lactones were smaller in MWCNTs compared to the corresponding ones obtained for SWCNTs. However, the amount of carboxylic acids was similar for NTX3 or considerably larger for the NC3100 MWCNTs in comparison with the SWCNTs, verifying that the transformation of carbonyl/quinones to carboxylic acids is more favorable on the surface of MWCNTs than on SWCNTs, in particular when compared to phenols. This justifies the lower CO/CO_2 ratios found for hydrothermally treated MWCNTs with respect to their SWCNT analogues and further emphasizes the high efficiency of hydrothermal oxidation for CCVD MWCNTs under optimal conditions. The enhanced surface reactivity of hydrothermally treated MWCNTs for -COOH generation may be in principle rationalized by the inherent differences in the spatial dimensions and defect structure (e.g. CNTs caps with pentagons and heptagons) of MWCNTs with respect to SWCNTs. This could effectively alter the nature and density of reactive sites for oxygen groups' formation and lead to diverse oxidation mechanisms under hydrothermal conditions. Recent theoretical work on the oxidation of MWCNTs under HNO_3 reflux predicted a four step reaction mechanism for a monovacancy defect leading to a surface carboxylic group accompanied with vacancy enlargement [6]. On the other hand, a different oxidation mechanism may occur for SWCNTs, where the confined diameter and diverse chirality were predicted to lower the adsorption barrier for NO_2 attack on the tube walls leading to the preferential functionalization and even selective removal of small diameter metallic SWCNTs [10].

For comparison, the boiling acid method was also applied for the surface functionalization of the NTX3 and NC3100 MWCNTs. Figure 5.5 shows the TPD spectra for NTX3 treated with 7.0 mol L^{-1} HNO_3 at boiling temperature and their deconvolution to the individual components of the different oxygen surface groups (see Figure A.1 in Appendix A for the corresponding spectra of NC3100 MWCNTs).

The corresponding amount of surface groups released as CO and CO_2 as well as wt.% O_2 are included in Table 5.1. The total amount of surface groups was comparable, though systematically lower, than that obtained under hydrothermal treatment at the highest HNO_3 concentration (0.3 mol L^{-1}), especially for the highly

functionalized NC3100 samples (results not shown – forward to Figure A.1 in Appendix A). These results indicate that apart from being a controllable functionalization process that consumes a lower amount of oxidizing agent, hydrothermal oxidation competes well with the harsh boiling HNO_3 treatment in terms of the generation of sufficient quantities of oxygen functionalities on the MWCNTs surface.

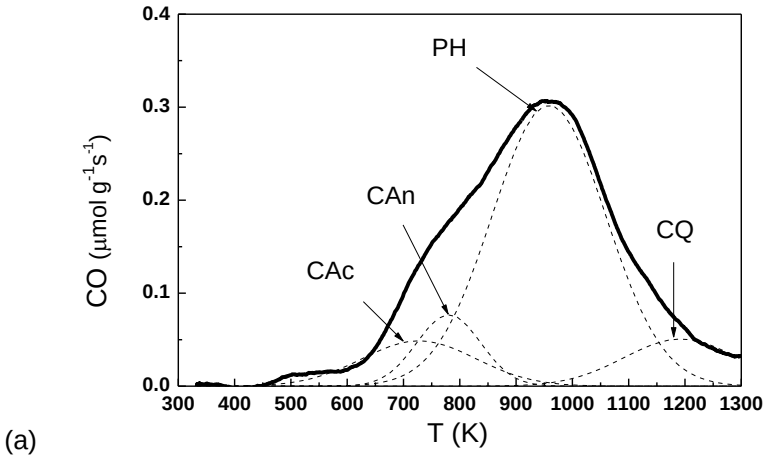

(a)

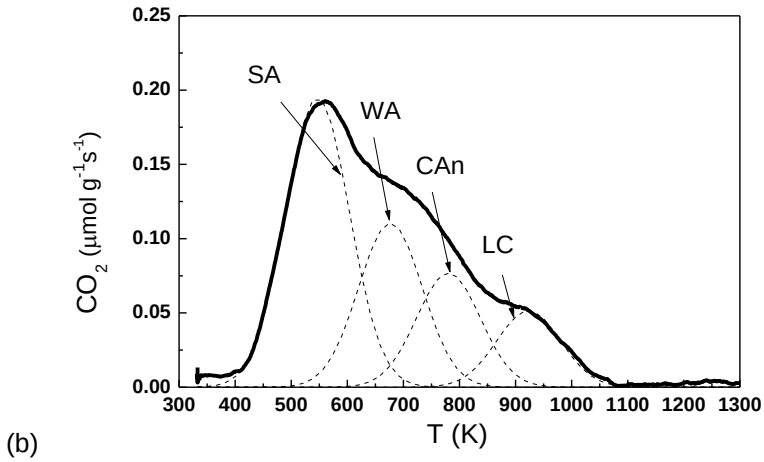

(b)

Figure 5.5 - Deconvolution of TPD spectra for NTX3 treated with [HNO_3] = 7.0 mol L^{-1} at boiling temperature: groups released as (a) CO and (b) CO_2 (PH – phenols; CAn – carboxylic anhydrides; CQ – carbonyl quinones; LC – lactones; CAc – carboxylic acids; SA – strong acidic CAc; WA – weakly acidic CAc).

Nevertheless, the CO_2 amount was relatively higher (by 13%) in the MWCNTs oxidized under boiling acid compared to the hydrothermally treated ones (Table 5.1).

Specifically, the amounts of carboxylic acids for the NTX3 sample treated with the boiling method (7.0 mol L^{-1}) and for the hydrothermally treated sample at the highest HNO_3 concentration (0.3 mol L^{-1}) reached 520 and 370 μmol g^{-1}, respectively. In the case of NC3100, the corresponding amounts were 550 and 440 μmol g^{-1}, respectively, indicating that more acidic surface groups were produced on the MWCNT surface not only due to the aggressive oxidizing conditions of the boiling acid method but also because hydrothermal oxidation is performed at 473 K, a temperature where a fraction of carboxylic acids can be partially released. In this context, the CO_2 TPD spectrum of the hydrothermally treated samples (Figure 5.1 b) differed appreciably from that obtained under boiling conditions (Figure 5.5 b). In the latter case, CO_2 evolved from lower temperatures, due to the higher amount of carboxylic acids in this sample, allowing the distinction of two different types of carboxylic acids by the deconvolution of the CO_2 TPD spectrum, namely strong acidic (SA) and weakly acidic (WA) carboxylic acids, which have been established to evolve at lower and higher temperatures, respectively [41]. A shoulder in the CO spectrum can be also traced at the same temperatures, where the carboxylic acids evolve in the CO_2 spectrum (identified as CAc in Figure 5.5 a), whose origin, however, is not fully understood [5]. An additional process that occurs during the hydrothermal oxidation is the weight loss (WL) that corresponds to the difference between the weight of CNTs introduced into the autoclave and the final weight of the recovered material after the hydrothermal run. Figure 5.6 compares the observed Weight Loss (WL) as a function of the $[HNO_3]/m_{CNT}$ ratio for the SWCNTs, NTX3 and NC3100 MWCNTs.

The observed WL variation can be fitted to exponential functions, resembling the dependence of the oxygen groups with the $[HNO_3]/m_{CNT}$ ratio. This effect can be associated with the preferential formation of oxygen groups on carboxylated carbonaceous fragments (CCFs) produced by the CNT's consumption during HNO_3 treatment, especially SWCNTs that are most susceptible to acid oxidation [2, 11-14].

It was proposed that under strong enough oxidizing conditions the adsorbed CCFs on the CNTs walls can be fully gasified to CO_2, accounting for the observed WL and its dependence on the HNO_3 concentration [1].

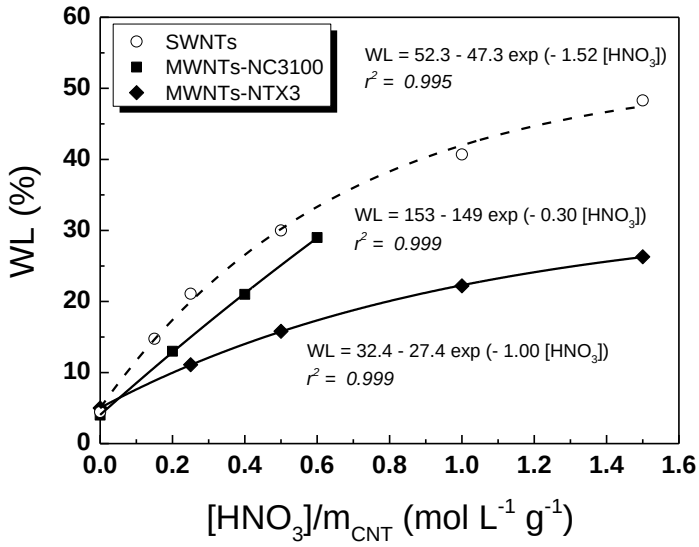

Figure 5.6 - Weight loss observed after hydrothermal treatment of NTX3, NC3100 and SWCNTs as a function of the $[HNO_3]/m_{CNT}$ ratio.

In the present case, the WL increased upon hydrothermal treatment at 0.30 mol L^{-1} HNO_3 up to around 50%, 25% and 30% for SWCNTs, NTX3 and NC3100 materials, respectively. These results confirm the higher stability of the MWCNT structure to nitric acid oxidation compared with the SWCNTs. Moreover, NC3100 exhibited appreciable WL upon hydrothermal oxidation, approaching that of SWCNTs, consistently with their highly functionalized state.

5.1.2 Thermal analysis

Further evidence for the efficiency of MWCNT hydrothermal oxidation was provided by TGA-DSC measurements. Figure 5.7 compares the TGA curves and the corresponding enthalpy (DSC) changes on the pristine and hydrothermally treated NTX3 MWCNTs at different HNO_3 concentrations.

The effect of hydrothermal treatment was evident on both classes of materials, as increasing the HNO_3 concentration resulted in significantly lower thermal stability of the functionalized MWCNTs due to the existence of covalently bonded oxidizing surface groups and the concurrent partial loss of crystallinity [15].

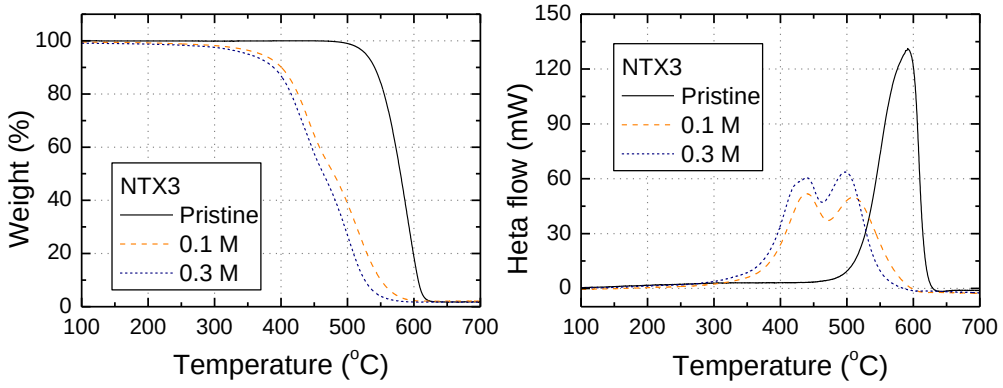

Figure 5.7 – TGA-DSC curves on the pristine and hydrothermally treated NTX3 MWCNTs at different HNO_3 concentrations.

No marked differences were observed on the thermal stability between the pristine NTX3 and the NC3100 samples. The onset of thermal degradation for the pristine NTX3 occurred at ca. 753 K, only 30 K higher than the corresponding one of NC3100 MWCNTs, despite their much larger diameter (the oxidation temperatures determined from the maxima of the corresponding mass loss rates were 861 and 870 K for the NTX3 and NC3100, respectively). This further implies that the thin and short NC3100 MWCNTs present a high degree of crystallinity, in spite of their small diameter that would otherwise lead to considerably lower oxidation temperature and thermal stability [16]. Hydrothermal functionalization reduced drastically the thermal stability of NTX3 with increasing HNO_3 concentration, as for the functionalized samples of NC3100. For the last, thermal degradation started at 603 and 543 K for the treated samples at 0.1 and 0.3 mol L^{-1} HNO_3, followed by complete burn out at 878 and 813 K, respectively (results not shown). However, contrary to the NC3100 MWCNTs, two major components with distinct thermal properties were clearly differentiated by a slope change of the TGA traces around 763 K and a double peak profile of the DSC curve for the functionalized NTX3 samples. The first component was identified at temperatures slightly below the corresponding oxidation peak of NC3100, while the second one occurred at higher temperatures, indicative of a MWCNT fraction more resistant to oxidation. This distinctive behavior may be related to the diverse reactivity of inner and outer CNT layers to thermal decomposition [17] most pertinent to the large diameter NTX3 MWCNTs comprising a high number (25-50) of rolled graphitic layers. Furthermore, TGA measurements on the NTX3 and NC3100 MWCNTs oxidized with 7.0 mol L^{-1} HNO_3 at boiling temperature (not shown), revealed considerably higher thermal stability of both samples compared to the

corresponding (0.3 mol L^{-1}) hydrothermally functionalized ones, in spite of the presence of comparable amounts of oxygen functional groups (Table 5.1). This would further imply that hydrothermal treatment results in more homogenous distribution of oxygen groups within the MWCNTs, most likely through the beneficial effect of pressure, leading to the distinct reduction of MWCNT thermal stability compared to the boiling acid method. In the latter case, surface modification including the formation of amorphous carbon may be limited to the external layers of the MWCNTs, leaving intact the internal CNTs structure and justifying the relatively higher thermal stability of boiling acid treated samples.

5.1.3 Raman spectroscopy

The effect of hydrothermal oxidation on the MWCNTs' microstructure was further investigated by Raman spectroscopy. Figure 5.8 presents the evolution of the Raman spectra for the hydrothermally functionalized NTX3 samples compared with the pristine one at two different excitation wavelengths in the NIR (785 nm) and visible range (514.5 nm).

The characteristic Raman modes of MWCNTs were thus identified, the most prominent being the first order tangential G band (~1585 cm^{-1}) together with two highly dispersive modes, the defect-induced D band (~1350 cm^{-1} at 514.5 nm) and its overtone (G' band) at 2D (~2700 cm^{-1} at 514.5 nm). The D band originates from a double resonant Raman process that involves elastic scattering from defects together with one phonon inelastic scattering, rendering it the characteristic feature for the identification of structural disorder and defects in graphitic materials [18].

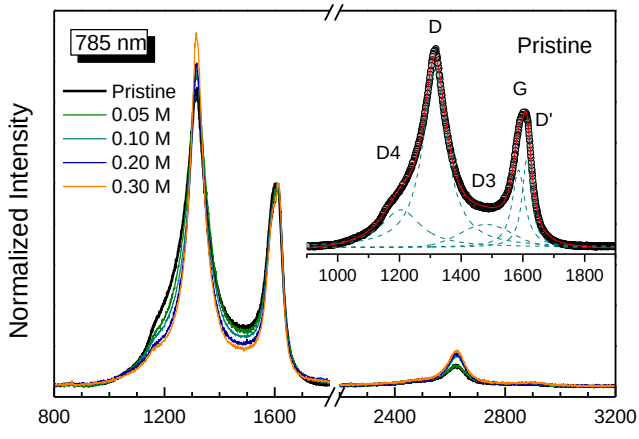

(a)

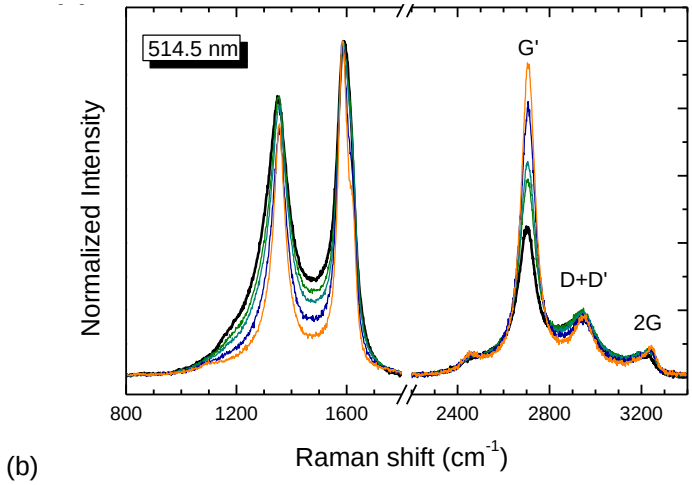

(b)

Figure 5.8 - Raman spectra on the pristine and hydrothermally treated NTX3 MWCNTs at (a) 785 nm and (b) 514.5 nm. The Raman intensity was normalized to that of the G band. The inset in (a) depicts representative results of the five-peak spectral fitting for the pristine MWCNTs at 785 nm.

On the other hand, the second-order G' band is activated independently of defects through a two-phonon double resonance process [18], which is responsible for its dispersive nature and sensitivity to the structural ordering of the tube walls and the graphitic electronic structure [19]. Two additional defect-induced modes of lower intensity were also observed: the D' band appearing as a shoulder to the G mode at ~1622 cm^{-1} arising from a double resonance process similar to the D-band [18] and the relatively broad D + D' combination mode (~2950 cm^{-1} at 514.5 nm) [20]. Most of the MWCNTs' Raman bands exhibited significant variations for the hydrothermally treated NTX3 upon increasing the HNO_3 concentration, at both excitation energies. However, quantitative spectral analysis at the intermediate frequency range (1200-1800 cm^{-1}) in terms of the three independent Raman bands (G, D and D') resulted in rather poor fitting results. Accurate spectral deconvolution was obtained by including two additional broad bands, the D3 (~1500 cm^{-1}) and D4 (~1200 cm^{-1}) ones (inset of Figure 5.8 a), related to the presence of amorphous carbon and disordered graphitic material [21-23], respectively, following the five-peak fitting procedure of Sadezky et al. [24] that has been successfully applied in several carbonaceous materials [25, 26] including MWCNTs [27, 28] . At the high frequency range (2300-3400 cm^{-1}), the Raman spectra could be well described by the superposition of the weak non-dispersive step-like mode at ~2450 cm^{-1} related to the overtone of the longitudinal optical phonon near the K points of the two-dimensional graphite Brillouin zone with q = 0 [29], the G' and the defect-induced D + D' bands together with a

composite band at higher frequencies (see Figure A.2 in Appendix A). The latter band could be approximated by two weak peaks at ~3180 and ~3240 cm^{-1} corresponding to the frequencies of the G band overtone (2G) and its shifted variant in graphitic materials due to the overbending of the graphite phonon dispersion curve [2, 30]. Figure 5.9 a and b show the [HNO_3] dependence of the Raman intensity ratios of the D, D', D+D', D3 and D4 bands (I_D/I_G, $I_{D'}/I_G$, $I_{D+D'}/I_G$, I_{D3}/I_G and I_{D4}/I_G) relative to the tangential G mode for the NTX3 MWCNTs, calculated from the areas of the corresponding Raman bands, at 514.5 and 785 nm, respectively.

A gradual decrease of the integrated intensity ratios for both the defect activated D, D', and D + D' modes and the two broad D3 and D4 bands due to amorphous/disordered carbon, was evidenced at both excitation wavelengths upon successive introduction of oxygen functionalities on the NTX3 MWCNTs with increasing HNO_3 concentration. This variation apparently contrasts with the linear increment of the corresponding defect-activated Raman band intensity ratios with the amount of oxygen groups on hydrothermally functionalized SWCNTs under the same conditions [2] as well as the frequently observed increase of the I_D/I_G ratio with the reaction time for MWCNTs oxidized by the boiling acid method [31, 32].

The decrease of the intensity ratios was further accompanied by the progressive narrowing of the width (full width at half-maximum – FWHM) of the defect activated Raman bands, as shown in Figure 5.9 c, together with a systematic upward shift of their frequency reaching 5, 8 and ~15 cm^{-1} for the D, D' and D + D' bands, respectively, under the highest HNO_3 concentration of 0.30 mol L^{-1}.

Both effects, i.e. the relative intensity reduction and the narrowing/shift of the defect activated Raman bands, point to the preferential oxidation of the most reactive external carbon layers on the surface of NTX3 MWCNTs with hydrothermal treatment, in close analogy to previous results on soot oxidation [25]. On the other hand, the G' band, which is independent of defects and sensitive to the graphitic structural ordering [19], was significantly enhanced upon increasing the HNO_3 concentration. Specifically, the intensity ratio $I_{G'}/I_G$ increased continuously with [HNO_3], while the FWHM of the G' band decreased drastically in the same concentration range (Figure 5.9 d).

This effect can be rationalized by the partial removal of the amorphous carbon deposits on the MWCNTs or even the consumption of the most disordered/defective outer MWCNTs shells upon hydrothermal oxidation [33], directly probed by the decrease of the D3 and D4 band intensities.

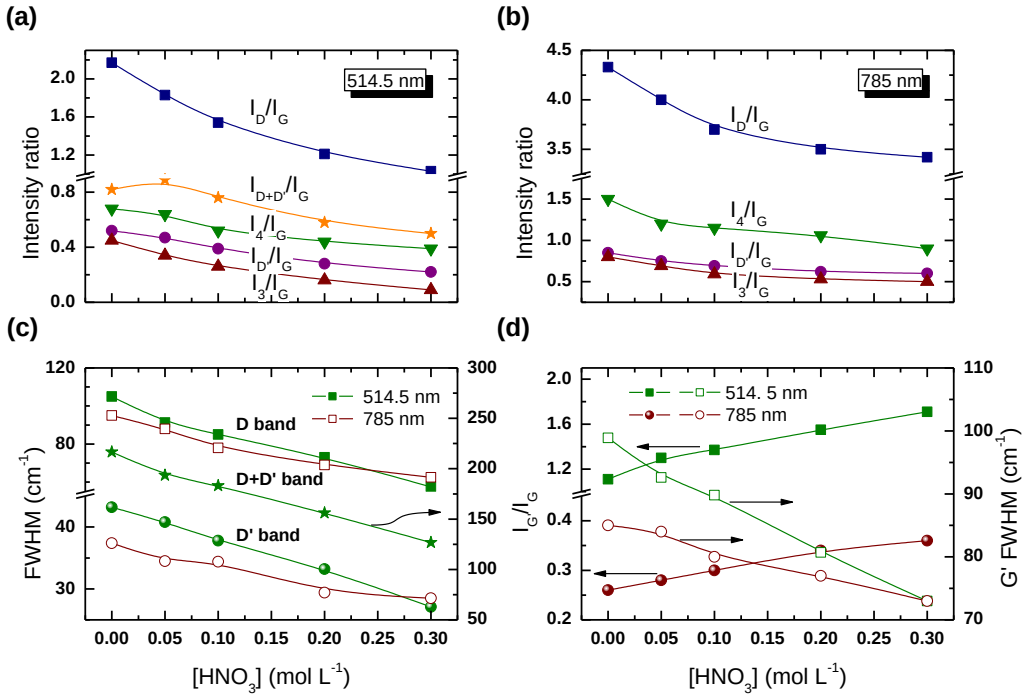

Figure 5.9 - The HNO_3 concentration dependence of the I_D/I_G, $I_{D'}/I_G$, $I_{D+D'}/I_G$, I_{D3}/I_G and I_{D4}/I_G integrated intensity ratios for the hydrothermally functionalized NTX3 MWCNTs at (a) 514.5 and (b) 785 nm. Variation of the FWHM of the defect activated (D, D', D+D') Raman bands (c) and the intensity ratio $I_{G'}/I_G$ and FWHM of the G' band (d) as a function of $[HNO_3]$.

The inner, more graphitic shells of the nanotubes are thus unveiled, which can be identified by the upsurge of the narrow G' band together with the relatively sharper and upward shifted D, D', D + D' bands, whose intensity is primarily determined by the inherent defect structure of the CCVD grown MWCNTs rather than the oxygen groups produced by hydrothermal oxidation. Such a variation indicates that besides the controlled generation of functional groups, the hydrothermal treatment has the capacity to reduce the amount of amorphous/disordered carbon from the MWCNTs.

This behavior can be contrasted to the enhanced formation of amorphous carbon during the MWCNT digestion and the concomitant weight loss under the harsh boiling acid oxidation conditions [31]. This was directly evidenced by Raman measurements on the NTX3 MWCNTs oxidized with 7.0 mol L^{-1} HNO_3 at boiling temperature (Figure A.2 in Appendix A). The corresponding Raman spectra were similar to those of the pristine material rather than the 0.30 mol L^{-1} HNO_3 treated sample, despite the

comparable amounts of functional groups produced by the boiling and hydrothermal treatments. In fact, spectral analysis revealed that the D, D', D + D' bands were not severely affected by the boiling acid oxidation (the I_D/I_G, $I_{D'}/I_G$, $I_{D+D'}/I_G$ intensity ratios decreased by 10% at most compared to the pristine NTX3). On the other hand, the relative intensity of the D3 band at ~1500 cm^{-1} associated with the presence of amorphous carbon increased significantly, i.e. the I_{D3}/I_G ratio was doubled for the boiling acid treated NTX3, in sharp contrast to the hydrothermally treated sample at 0.30 mol L^{-1} HNO_3, where the corresponding ratio showed a fivefold decrease. This behavior confirmed that hydrothermal oxidation is much more efficient in the generation of oxygen functionalities on the MWCNTs compared to the aggressive boiling acid oxidation, where the creation of more carboxylic acid groups identified by TPD analysis is accompanied by extensive formation of amorphous carbon on the MWCNT surface.

Spectral analysis of pristine NC3100 MWCNTs at 514.5 nm revealed that the relative intensity of the defect activated Raman bands, especially that of the D, D' and D4 bands, as well as their width were appreciably lower than those of the corresponding NTX3 MWCNTs (results not shown). In addition, the relative intensity of the G' band was considerably enhanced for the pristine NC3100 by ca. 70%, indicating that these MWCNTs are more crystalline and contain smaller amounts of amorphous carbon than the NTX3 ones, in agreement with high resolution TEM results on NC3100 [34]. Hydrothermal oxidation resulted in a moderate and most importantly non-monotonous dependence of the I_D/I_G, $I_{D'}/I_G$, $I_{D+D'}/I_G$, I_{D3}/I_G and I_{D4}/I_G intensity ratios on the HNO_3 concentration. In particular, a modest decrease of the relative Raman intensity was observed up to 0.1 mol L^{-1} HNO_3, most evident for the D band, followed by a gradual increase to the initial values at higher nitric acid concentrations. This variation was further accompanied by the decrease of the Raman band width, especially up to 0.10 mol L^{-1}. Likewise, the G' band exhibited a decrease of the $I_{G'}/I_G$ intensity ratio together with narrowing up to 0.10 mol L^{-1}, whereas it remained nearly stable at higher HNO_3 concentrations. This evolution complies favorably with the TPD results, where a faster increment of both the CO and CO_2 amounts was observed above 0.10 mol L^{-1} HNO_3. This dependence can be accordingly accounted for the decrease of the amorphous carbon content at relatively low HNO_3 concentrations (0.10 mol L^{-1}), similar to NTX3, while the excessive production of oxygen surface groups appears to take over at higher HNO_3 concentrations.

To further investigate the extent of amorphous carbon generation and the thermal stability of oxygen surface groups on the oxidized MWCNTs, the hydrothermally

treated NTX3 and NC3100 samples at the highest HNO_3 concentration (0.30 mol L^{-1}) and the boiling acid NTX3 (7.0 mol L^{-1}) samples were subjected to successive isothermal oxidations at 623 and 673 K in air. Mild oxidative treatment at 623-673 K in air is expected to oxidize amorphous carbon and CCFs from CNTs without affecting drastically oxygen groups such as carboxylic anhydrides and those released as CO that decompose at higher temperatures (Figure 5.1), and thus provide an independent probe of their modified surface chemistry upon HNO_3 oxidation [2].

Figure 5.10 compares the corresponding Raman spectra of the thermally treated NTX3 samples at 514.5 nm.

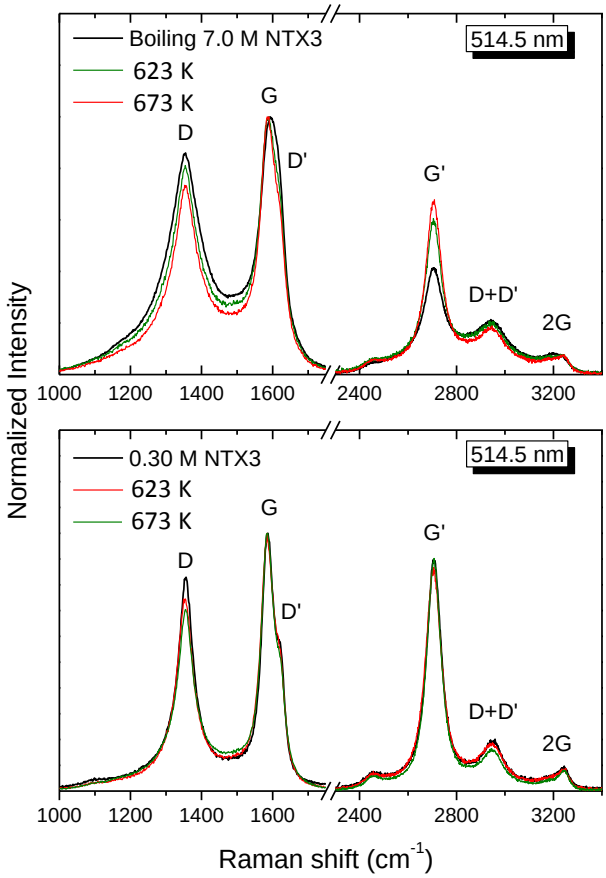

Figure 5.10 - Raman spectra of the boiling (7.0 mol L^{-1}) and hydrothermally (0.3 mol L^{-1}) acid treated NTX3 MWCNTs under isothermal oxidation at 623 and 673 K.

The Raman spectra of the hydrothermally functionalized 0.30 mol L^{-1} NTX3 MWCNTs showed rather small changes upon isothermal oxidation, the most notable variation being the decrease of I_D/I_G by ca. 5%, which can be mainly related to the moderate removal of acidic groups released as CO_2 rather than amorphous carbon [35], since the relative intensity of the D3 and D4 Raman bands was hardly affected. On the other hand, the Raman spectra of the boiling acid treated NTX3 exhibited appreciable changes upon thermal oxidation demonstrating clearly the counter acting effects of hydrothermal and boiling acid treatment on the MWCNT surface chemistry. In that case, thermal oxidation led to the progressive narrowing and decrease of the relative intensity of the defect activated D, D', and D + D' modes reaching 20% at 673 K, together with an even higher reduction of the I_{D3}/I_G and I_{D4}/I_G intensity ratios (40% at 673 K) due to the decrease of the amorphous carbon content. In addition, the G' band gradually narrowed (the FWHM decreased from 102 to 85 cm^{-1} at 673 K) and its intensity ratio was greatly enhanced upon increasing the isothermal annealing temperature, resembling closely the effect of hydrothermal treatment with the increase of HNO_3 concentration on the NTX3 MWCNTs.

These results confirm the beneficial effects of hydrothermal HNO_3 treatment that outperforms the harsh boiling acid oxidation by generating controlled amounts of oxygen groups on the CNTs, while partially removing amorphous carbon fragments from the surface of MWCNTs. The efficiency and the mild oxidative conditions underlying hydrothermal treatment were further corroborated by the isothermal oxidation experiments on the heavily functionalized 0.30 mol L^{-1} NC3100 characterized also by the highest degree of graphitization. Despite the large amounts of oxygen functionalities, the Raman spectra of the thin NC3100 MWCNTs exhibited the least sensitivity to thermal oxidation (see Figure A.3 in Appendix A), where minor changes of the D, D', and D + D' modes could be traced. The lowest amount of amorphous carbon/CCFs that could be thermally exfoliated from the MWCNTs' surface was observed for the NC3100 MWCNT. This further emphasizes that apart from the CNT morphological characteristics (diameter and length) the inherent structural properties and purity of the starting MWCNT materials are critical factors for the efficiency of the functionalization process and the nature of surface groups introduced on the nanotube surface under hydrothermal oxidation.

5.1.4 Pore structure analysis

The N_2 adsorption-desorption isotherms of the pristine and hydrothermally treated MWCNTs at different HNO_3 concentrations were assessed and the results for the NTX3 samples are presented in Figure 5.11.

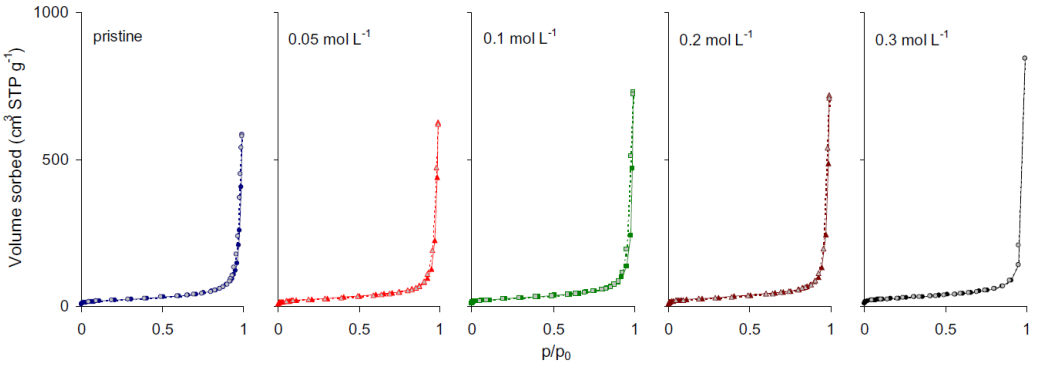

Figure 5.11 – Adsorption-desorption N_2 isotherms at 77 K of the pristine and hydrothermally functionalized NTX3 MWCNTs at different HNO_3 concentrations (left to right: 0, 0.05, 0.10, 0.20 and 0.30 mol L^{-1} HNO_3).

The N_2 adsorption isotherms for the NTX3 series are of type II and exhibit a steep increase of adsorption close to the saturation pressure, indicative of pore condensation into large meso and macropores without completely filling the pore volume of the material, precluding the accurate determination of the total pore volume. Smaller pristine and treated NC3100 samples present typical type IV isotherms (not shown), with hysteresis at high p/p_0, in agreement with previous results [34]. Moreover, while the shapes of the NTX3 isotherms remained practically the same at high p/p_0, the total pore volume values, V_{tot}, (determined from the N_2 uptake at $p/p_0 = 0.99$) increased appreciably with HNO_3 treatment (Table 5.2). The mesopore structure of the samples is closely associated with the pore space between the CNTs, i.e. the bundle free space. This behavior points to an inefficient re-packing of the nanotubes during acid treatment, which can be attributed to the large size (mainly length) of NTX3 MWCNTs, in contrast to what was observed for the smaller NC3100 samples as significant pore volume is lost (from 2.9 for the pristine MWCNTs to 1.1 ml g^{-1} for the material treated with 0.30 mol L^{-1} HNO_3), pointing to a more efficient arrangement of the nanotube bundles upon hydrothermal treatment. The BET surface areas, S_{BET}, increased continuously with the increase of the HNO_3

concentration, as shown in Figure 5.12. The values seem to approach asymptotically a maximum, correlating with the evolution of the surface group's concentration on the hydrothermally treated MWCNTs (Figure 5.3).

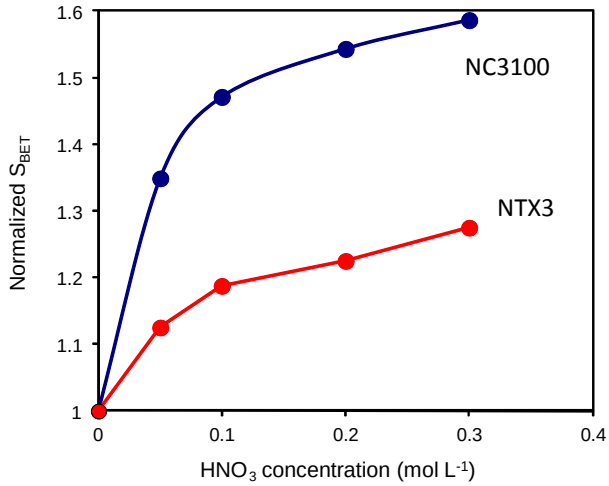

Figure 5.12 - Normalized (with respect to pristine samples) BET surface areas of the pristine and hydrothermally functionalized MWCNTs at different HNO_3 concentrations.

A small increase in surface area (80 up to 102 m^2/g for the pristine and 0.30 mol L^{-1} treated nanotubes, respectively) and micropore volume, V_{micro}, was derived (Figure 5.12 and Table 5.2), both being significantly lower than for those of the NC3100 samples. This S_{BET} and V_{micro} increase may be attributed to progressive decrease of the amorphous carbon content as well as the enhanced accessibility to the inner part of the nanotubes by defect creation and/or the opening of the nanotube caps.

To delineate the underlying variations in the MWCNTs pore structure upon hydrothermal oxidation, pore size analysis was performed by means of quenched solid density functional theory (QSDFT) adsorption kernels up to a size of 50 nm. Pure cylindrical models were thereby used, while the quenched solid variance of the method was applied as it allows the study of heterogeneous surfaces [36].

Although this model is based on slit pore geometry, it was considered as the most appropriate for the present case for the following reasons: (a) all experimental N2 adsorption isotherms at 77 K reveal hysteresis loops of H3 type [37], which is typical for layered materials/slit pore geometries, (b) in contrast to all other NonLocal Density Functional Theory (NLDFT) or Grand Canonical Monte Carlo (GCMC) models that

assume structureless homogeneous graphitic pore walls, the QSDFT method takes into account the effects of surface heterogeneity, which is typical for our functionalized samples, and (c) the QSDFT method eliminates artificial gaps and minimizes artificial peaks in the PSDs, a typical problem encountered in NLDFT calculations.

Table 5.2 - BET surface areas, S_{BET}, DFT micropore volume, V_{micro} and pore volume at $p/p_0 = 0.99$, designated as V^*, for the pristine and hydrothermally treated NTX3 samples [38].

$[HNO_3]$ (mol L^{-1})	S_{BET} (m^2 g^{-1})	V_{micro} (cm^3 g^{-1})	V^* (cm^3 g^{-1})
0- pristine	80	0.029	0.9
0.05	90	0.034	1.0
0.10	95	0.036	1.1
0.20	98	0.037	1.1
0.30	102	0.039	1.3

The pertinent pore size distributions (PSDs) for NTX3 samples are presented in Figure 5.13 showing rather small pores at the limit of micropore sizes (around 2 nm). As in the case of NC3100, these pores become more and more accessible to fluid molecules through defects created upon hydrothermal treatment. Beyond this size there is practically a continuum of different mesopores (e.g. local peaks at 5 and 10 nm) indicative of the rather random nature of the NTX3 texture in the mesoscale. In the case of NC3100 group, the PSDs revealed a systematic and more significant enhancement of the small mesopore peaks (3-6 nm) centered around 4 nm, arising from the inner part of the nanotubes, with increasing HNO_3 concentration. Moreover, the 0.30 mol L^{-1} treated sample revealed a slight decrease of the 4 nm pore volume coupled with a stronger sign of microporosity. Such a feature may be related to the partial deterioration of the CNT structure and the development of amorphous (or low crystallinity) areas in a way that part of the inner nanotube space is narrowed, since the original structure is smaller and thinner than that of the NTX3. Much larger pores (>40 nm) are observed for the pristine NTX3 MWCNTs and their size decreased to ca. 32 nm for the treated samples, while the strongest treatment (0.30 mol L^{-1}) resulted in a pore size peak at 24 nm. It may be thus concluded that the main

structural effect of hydrothermal treatment on the NTX3 nanotubes is a minimal disentaglement, together with a small re-organization of the tubes (since the mean pore size of large pores is slightly reduced).

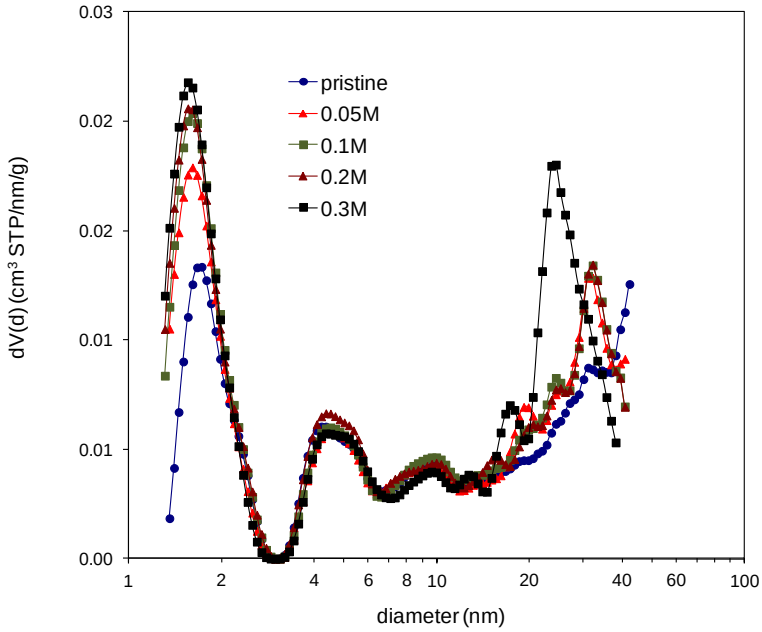

Figure 5.13 - QSDFT pore size distributions of pristine and hydrothermally functionalized NTX3 MWCNTs at different HNO_3 concentrations.

Due to original structural differences, the pore sizes of NC3100 were centered at 33, 27, 24 and 18 nm for the pristine, 0.05, 0.10 and 0.20 mol L^{-1} treated samples, respectively, while no further significant reduction (in volume and size) was observed for the sample treated with 0.30 mol L^{-1} HNO_3. This trend can be attributed to the oxygen surface groups that can increase the attractive forces between individual nanotubes, e.g. through H-bonding.

5.2 Conclusions

Nitric acid hydrothermal oxidation is demonstrated as a controlled and highly efficient functionalization process for CCVD grown MWCNTs under mild acidic conditions. Analytical investigations by TPD-MS and TGA-DSC have shown that HNO_3 hydrothermal treatment results in the progressive generation of distinct oxygen

functional groups on the MWCNT surface, controlled by the nitric acid concentration. The amount and thermal stability of oxygen functionalities was further found to be primarily determined by the MWCNTs morphology (diameter and length), as well as by the crystallinity and purity of the pristine materials. Furthermore, Raman spectroscopy revealed a progressive intensity reduction along with a shift and narrowing of the defect activated MWCNT Raman bands accompanied by the gradual enhancement of the graphitic G' (2D) band, indicative of the oxidation of the highly reactive external carbon layers on the surface of hydrothermally treated MWCNTs with increasing the HNO_3 concentration. This behavior was contrasted with the enhanced amorphous carbon generation obtained upon comparative processing of the CCVD MWCNTs with the boiling acid oxidation method that produced comparable amounts of oxygen functionalities, while consuming higher amounts of oxidizing agent.

Pore structure analysis of the functionalized MWCNTs revealed that upon hydrothermal treatment, the inner part of the nanotubes becomes progressively more accessible to fluid molecules, leading to the increase of surface area (also micropore volume, which remains rather low for all the samples). In the case of the short and thin MWCNTs (NC3100) hydrothermal oxidation additionally triggered a disentanglement followed by more efficient reorganization of the nanotube bundles, shifting thus the mean pore size from the macro to the mesopore areas. This behavior was considerably lessened for the long MWCNTs (NTX3), where the most pronounced effect of hydrothermal oxidation involved a small increase of the total pore volume. Nitric acid hydrothermal treatment is accordingly proposed as an effective mild functionalization process that affords the controlled modification of the MWCNTs' surface chemistry with significant amounts of oxygen functional groups, while removing the amorphous carbon from the CCVD MWCNT surface, a major drawback of conventional liquid phase oxidation methods.

The main global conclusions following the studies over SWCNTs and MWCNTs with relation to the hydrothermal and boiling acid methods are:

(i) CNTs morphology and especially the MWCNT's diameter and length and the concomitant variation of the surface area, dictate to a large extent the degree of surface functionalization.

(ii) MWCNTs structures present higher stability to nitric acid oxidation when compared to SWCNTs.

(iii) Under similar conditions, the evolution of acidic groups, namely carboxylic acids, is favored on the surface of MWCNTs structures rather than on SWCNTs, in a greater extent for smaller and thinner tubes.

(iv) Due to the higher temperatures applied on the hydrothermal oxidation methodology, more acidic groups are effectively anchored on MWCNTs surface through the boiling nitric acid route, since at those higher temperatures (473 K) a fraction of these functionalities can be released out of the CNT's surface.

(v) Despite comparable amounts of oxygen functional groups, MWCNTs show higher thermal stability when treated under boiling nitric acid conditions comparing with the analog samples hydrothermally oxidized.

(vi) Boiling acid methods require greater amounts of oxidizing agents but can produce high amounts of oxidized CNTs without need of applying higher temperature and pressure, which also implies higher costs. Simultaneously, hydrothermal oxidation is a consistent tool for such pre-treatments where the amount and type of groups needed are previously known and required for specific applications.

5.3 Experimental section

Pristine MWCNTs of large diameter (25-40 nm) produced by CCVD were purchased from Nanothinx S.A. with purity of 98.35% and length >10 μm, designated with the product code NTX3. For comparison purposes, in order to get some information about the influence of the CNTs structural properties on their functionalization, the results were compared with those obtained in our group with thin MWCNTs purchased from NANOCYL™, designated as NC3100, which were oxidized under similar conditions [39]. These MWCNTs are produced via the CCVD process with average diameter and length of 9.5 nm and 1.5 μm, respectively, and purity greater than 95%.

5.3.1 Multi-Walled Carbon Nanotubes functionalization

The NTX3 CNTs (0.2 g) were hydrothermally oxidized immersed in a HNO_3 solution at different concentrations (0 - blank experiment, 0.05, 0.1, 0.2, 0.3 mol L^{-1}) inside a pressurized vessel at the temperature of 473 K. HNO_3 oxidation was also performed by direct contact of the MWCNTs with the acid solution at boiling temperature, as it is a commonly used methodology to modify CNTs surface. The CNTs (0.5 g) were immersed in 7.0 mol L^{-1} HNO_3 solutions during 3 h. The detailed procedure for both

oxidation methods is described in Sections 2.1.1 and 2.1.2 of Chapter 2. Conditions at which the NC3100 CNTs were oxidized are described elsewhere [39].

5.3.2 Multi-Walled Carbon Nanotubes characterization

The surface chemistry of the MWCNTs was quantified in terms of oxygen functionalities by deconvolution of the CO and CO_2 profiles obtained by temperature programmed desorption (TPD) coupled with mass spectrometry (MS).

Other analytical techniques were performed in cooperation with the Institute of Advanced Materials, NCSR Demokritos, Greece.

The specific surface area (S_{BET}) of the materials was determined through N_2 adsorption-desorption isotherms, the total pore volume and the micropore volume, V_{micro}, performed by means of QSDFT.

Thermogravimetric analysis (TGA) with simultaneous differential scanning calorimetry (DSC) was conducted to evaluate the effect of hydrothermal oxidation on thermal stability and physical transformations on MWCNTs.

Structural morphologic changes at molecular level were assessed by Raman measurements at two different excitation wavelengths in the near infrared (785 nm) and visible range (514.5 nm) by evaluating the evolution of the graphite and defect Raman modes against the different oxidizing conditions tested.

Detailed description of the conditions applied in all the above mentioned analytical techniques are described in Chapter 3.

5.4 References

[1] Marques RRN, Machado BF, Faria JL, Silva AMT. Controlled generation of oxygen functionalities on the surface of Single-Walled Carbon Nanotubes by HNO3 hydrothermal oxidation. Carbon. 2010; 48 (5):1515-23.

[2] Romanos GE, Likodimos V, Marques RRN, Steriotis TA, Papageorgiou SK, Faria JL, et al. Controlling and Quantifying Oxygen Functionalities on Hydrothermally and Thermally Treated Single-Wall Carbon Nanotubes. J Phys Chem C. 2011; 115 (17):8534-46.

[3] Silva AMT, Machado BF, Figueiredo JL, Faria JL. Controlling the surface chemistry of carbon xerogels using HNO3-hydrothermal oxidation. Carbon. 2009; 47 (7):1670-9.

[4] Figueiredo JL, Pereira MFR, Freitas MMA, Órfão JJM. Modification of the surface chemistry of activated carbons. Carbon. 1999; 37 (9):1379-89.

[5] Figueiredo JL, Pereira MFR, Freitas MMA, Órfão JJM. Characterization of Active Sites on Carbon Catalysts. Ind Eng Chem Res. 2007; 46 (12):4110-5.

[6] Gerber I, Oubenali M, Bacsa R, Durand J, Gonçalves A, Pereira MFR, et al. Theoretical and Experimental Studies on the Carbon-Nanotube Surface Oxidation by Nitric Acid: Interplay between Functionalization and Vacancy Enlargement. Chem-Eur J. 2011; 17 (41):11467-77.

[7] Zhang J, Zou H, Qing Q, Yang Y, Li Q, Liu Z, et al. Effect of Chemical Oxidation on the Structure of Single-Walled Carbon Nanotubes. J Phys Chem B. 2003; 107 (16):3712-8.

[8] Ros TG, van Dillen AJ, Geus JW, Koningsberger DC. Surface Oxidation of Carbon Nanofibres. Chem-Eur J. 2002; 8 (5):1151-62.

[9] Yang D-Q, Rochette J-F, Sacher E. Functionalization of Multiwalled Carbon Nanotubes by Mild Aqueous Sonication. J Phys Chem B. 2005; 109 (16):7788-94.

[10] Yang C-M, Park JS, An KH, Lim SC, Seo K, Kim B, et al. Selective Removal of Metallic Single-Walled Carbon Nanotubes with Small Diameters by Using Nitric and Sulfuric Acids. J Phys Chem B. 2005; 109 (41):19242-8.

[11] Yu H, Jin Y, Peng F, Wang H, Yang J. Kinetically Controlled Side-Wall Functionalization of Carbon Nanotubes by Nitric Acid Oxidation. J Phys Chem C. 2008; 112 (17):6758-63.

[12] Worsley KA, Kalinina I, Bekyarova E, Haddon RC. Functionalization and Dissolution of Nitric Acid Treated Single-Walled Carbon Nanotubes. J Am Chem Soc. 2009; 131 (50):18153-8.

[13] Price BK, Lomeda JR, Tour JM. Aggressively Oxidized Ultra-Short Single-Walled Carbon Nanotubes Having Oxidized Sidewalls. Chem Mater. 2009; 21 (17):3917-23.

[14] Del Canto E, Flavin K, Movia D, Navio C, Bittencourt C, Giordani S. Critical Investigation of Defect Site Functionalization on Single-Walled Carbon Nanotubes. Chem Mater. 2010; 23 (1):67-74.

[15] Santangelo S, Messina G, Faggio G, Lanza M, Milone C. Evaluation of crystalline perfection degree of multi-walled carbon nanotubes: correlations between thermal kinetic analysis and micro-Raman spectroscopy. J Raman Spectrosc. 2011; 42 (4):593-602.

[16] Singh DK, Iyer PK, Giri PK. Diameter dependence of oxidative stability in multiwalled carbon nanotubes: Role of defects and effect of vacuum annealing. J Appl Phys. 2010; 108 (8):084313.

[17] Lehman JH, Terrones M, Mansfield E, Hurst KE, Meunier V. Evaluating the characteristics of multiwall carbon nanotubes. Carbon. 2011; 49 (8):2581-602.

[18] Pimenta MA, Dresselhaus G, Dresselhaus MS, Cancado LG, Jorio A, Saito R. Studying disorder in graphite-based systems by Raman spectroscopy. Phys Chem Chem Phys. 2007; 9 (11):1276-90.

[19] Delhaes P, Couzi M, Trinquecoste M, Dentzer J, Hamidou H, Vix-Guterl C. A comparison between Raman spectroscopy and surface characterizations of multiwall carbon nanotubes. Carbon. 2006; 44 (14):3005-13.

[20] Fantini C, Pimenta MA, Strano MS. Two-Phonon Combination Raman Modes in Covalently Functionalized Single-Wall Carbon Nanotubes. J Phys Chem C. 2008; 112 (34):13150-5.

[21] Cuesta A, Dhamelincourt P, Laureyns J, Martínez-Alonso A, Tascón JMD. Raman microprobe studies on carbon materials. Carbon. 1994; 32 (8):1523-32.

[22] Jawhari T, Roid A, Casado J. Raman spectroscopic characterization of some commercially available carbon black materials. Carbon. 1995; 33 (11):1561-5.

[23] Dippel B, Jander H, Heintzenberg J. NIR FT Raman spectroscopic study of flame soot. Phys Chem Chem Phys. 1999; 1 (20):4707-12.

[24] Sadezky A, Muckenhuber H, Grothe H, Niessner R, Pöschl U. Raman microspectroscopy of soot and related carbonaceous materials: Spectral analysis and structural information. Carbon. 2005; 43 (8):1731-42.

[25] Ivleva NP, Messerer A, Yang X, Niessner R, Pöschl U. Raman Microspectroscopic Analysis of Changes in the Chemical Structure and Reactivity of Soot in a Diesel Exhaust Aftertreatment Model System. Environ Sci Technol. 2007; 41 (10):3702-7.

[26] Vallerot J-M, Bourrat X, Mouchon A, Chollon G. Quantitative structural and textural assessment of laminar pyrocarbons through Raman spectroscopy, electron diffraction and few other techniques. Carbon. 2006; 44 (9):1833-44.

[27] Frank B, Rinaldi A, Blume R, Schlögl R, Su DS. Oxidation Stability of Multiwalled Carbon Nanotubes for Catalytic Applications. Chem Mater. 2010; 22 (15):4462-70.

[28] Rinaldi A, Frank B, Su DS, Hamid SBA, Schlögl R. Facile Removal of Amorphous Carbon from Carbon Nanotubes by Sonication. Chem Mater. 2011; 23 (4):926-8.

[29] Shimada T, Sugai T, Fantini C, Souza M, Cançado LG, Jorio A, et al. Origin of the 2450 cm−1 Raman bands in HOPG, single-wall and double-wall carbon nanotubes. Carbon. 2005; 43 (5):1049-54.

[30] Thomsen C. Second-order Raman spectra of single and multiwalled carbon nanotubes. Phys Rev B. 2000; 61 (7):4542-4.

[31] Rosca ID, Watari F, Uo M, Akasaka T. Oxidation of multiwalled carbon nanotubes by nitric acid. Carbon. 2005; 43 (15):3124-31.

[32] Osswald S, Havel M, Gogotsi Y. Monitoring oxidation of multiwalled carbon nanotubes by Raman spectroscopy. J Raman Spectrosc. 2007; 38 (6):728-36.

[33] Koh AL, Gidcumb E, Zhou O, Sinclair R. Observations of Carbon Nanotube Oxidation in an Aberration-Corrected Environmental Transmission Electron Microscope. ACS Nano. 2013; 7 (3):2566-72.

[34] Tessonnier J-P, Rosenthal D, Hansen TW, Hess C, Schuster ME, Blume R, et al. Analysis of the structure and chemical properties of some commercial carbon nanostructures. Carbon. 2009; 47 (7):1779-98.

[35] Behler K, Osswald S, Ye H, Dimovski S, Gogotsi Y. Effect of thermal treatment on the structure of multi-walled carbon nanotubes. J Nanopart Res. 2006; 8 (5):615-25.

[36] Neimark AV, Lin Y, Ravikovitch PI, Thommes M. Quenched solid density functional theory and pore size analysis of micro-mesoporous carbons. Carbon. 2009; 47 (7):1617-28.

[37] Sing KSW, Everett DH, Haul RAW, Moscou L, Pierotti RA, Rouquerol J, et al. Reporting physisorption data for gas/solid systems with special reference to the

determination of surface area and porosity (Recommendations 1984). Pure Appl Chem. 1985; 57 (4):603-19.

[38] Gregg SJ, Sing KSW. Adsorption, Surface Area and Porosity. New York: Academic Press; 1982.

[39] Likodimos V, Steriotis TA, Papageorgiou SK, Romanos GE, Marques RRN, Rocha RP, et al. Controlled surface functionalization of multiwall carbon nanotubes by HNO3 hydrothermal oxidation. Carbon. 2014; 69:311-26.

Part IV

TiO_2/CNT composites

6 TiO_2/CNT composites for photocatalytic degradation of caffeine aqueous solutions

Photocatalytic degradation of caffeine: Developing solutions for emerging pollutants[4]

The photocatalytic degradation of the psychoactive substance caffeine was studied by testing composites prepared with MWCNTs and three different TiO_2 materials: one synthesized by a modified sol-gel method and two commercial others obtained from Evonik Degussa Corporation (P25) and Sigma-Aldrich. These materials were characterized by several techniques (DRIFT, XRD, N_2 adsorption-desorption isotherms, TEM, SEM). The tested materials increased the caffeine degradation rate in comparison to the pure photochemical regime. The oxygen groups created by acid treatment on the surface of the carbon nanotubes were crucial for the photocatalytic activity of all prepared composites. In addition, the photocatalytic activity of TiO_2 from Sigma-Aldrich markedly increased with the addition of functionalized carbon nanotubes, which seems to be related with the larger TiO_2 crystallite sizes and the better contact of these TiO_2 particles with carbon nanotubes. The activity of the semiconductor TiO_2 could be enhanced by taking advantage of the CNTs properties, in particular those with surface oxygen functionalities previously created by HNO_3 oxidation. Radicals and holes scavengers were applied to give some information about the photocatalytic reaction mechanism under near-UV/Vis irradiation, unveiling that free radicals produced by photo-excited electrons seem to be responsible for the higher activity observed for composites prepared with functionalized carbon nanotubes and TiO_2 from Sigma-Aldrich in comparison to bare TiO_2. Films prepared with these composites revealed higher photocatalytic activity than films of the pure TiO_2 benchmark P25.

[4] **Marques**, **R.R.N.**, Sampaio, M.J., Carrapiço, P.M., Silva, C.G., Morales-Torres, S., Dražić, G., Faria, J.L., Silva, A.M.T. (2013) Photocatalytic degradation of caffeine: Developing solutions for emerging pollutants, Catalysis Today, 209, 108-115.

6.1 Results and discussion

Several TiO_2/CNT composites were prepared based on different TiO_2 powders and pristine or previously functionalized MWCNTs through HNO_3 boiling oxidation and characterized through complementary analytical techniques. Two commercial TiO_2 materials were purchased to industrial companies, P25 (Evonik Degussa Corporation) and SA (Sigma-Aldrich), and the third one was synthesized in our laboratory by the sol-gel method (SG). The notation given to refer the composites is of type XX/CNT-Y, where XX is the type of TiO_2 used (SG, SA or P25) and Y is the mass of CNTs per 100 mass units of bare TiO_2. The notation CNTf stands for the previously functionalized CNTs.

Catalysts photocatalytic activity was tested in suspensions on a photoimmersion reactor, as described in Section 2.2.1, for the oxidative degradation of caffeine aqueous solutions and selected materials were further tested in the form of films, deposited on thin glass slides, using a different small cylindrical photo-reactor, with experimental details in Section 2.2.2.

6.1.1 Materials characterization

6.1.1.1 Diffuse reflection infrared Fourier transformed (DRIFT)

The vibrational structure of the three different bare TiO_2 materials (SG, P25 and SA) is depicted by the DRIFT spectra in Figure 6.1.

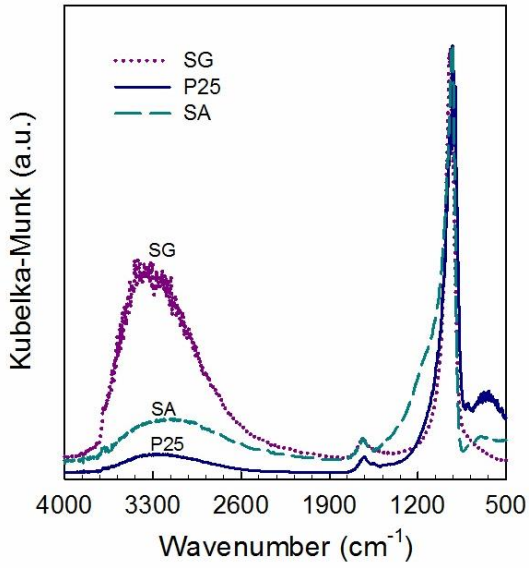

Figure 6.1 - DRIFT spectra for bare TiO_2 materials.

Table 6.1 – Pseudo-first order kinetic constants (*k*) and respective standard errors for the photolytic and photocatalytic degradation of caffeine using different catalysts. The regression coefficients (r^2) are also presented.

Catalyst	Scavenger	*k* (10^{-3} min^{-1})	r^2
None	none	0.36 ± 0.02	0.93
SG	none	4.9 ± 0.1	0.995
SG/CNTf-5	none	6.5 ± 0.5	0.995
SG/CNT-10	none	2.83 ± 0.04	0.998
SG/CNTf-10	none	5.89 ± 0.09	0.998
SG/CNTf-20	none	4.2 ± 0.1	0.99
P25	none	123 ± 10	0.99
P25	EDTA	5.4 ± 0.2	0.993
P25	*t*-BuOH	36.0 ± 0.9	0.998
P25/CNTf-5	none	62 ± 4	0.9994
P25/CNT-10	none	50 ± 4	0.99
P25/CNTf-10	none	83 ± 3	0.998
P25/CNTf-20	none	76 ± 3	0.997
P25/CNTf-20	EDTA	2.95 ± 0.07	0.994
P25/CNTf-20	*t*-BuOH	12.3 ± 0.4	0.994
SA	none	26 ± 2	0.99
SA	EDTA	2.16 ± 0.07	0.99
SA	*t*-BuOH	7.47 ± 0.05	0.9997
SA/CNTf-5	none	53 ± 6	0.98
SA/CNT-10	none	16.6 ± 0.4	0.997
SA/CNTf-10	none	63 ± 3	0.997
SA/CNTf-20	none	77 ± 3	0.998
SA/CNTf-20	EDTA	3.0 ± 0.2	0.95
SA/CNTf-20	*t*-BuOH	3.49 ± 0.04	0.998

The presence of coordinated water and Ti-OH bonds is confirmed in all materials by the band at around 1680 cm^{-1} [1]. The strong peak at around 900-950 cm^{-1}, common to all spectra, is typical of TiO_2 [2].

The broad band between 2500 and 3750 cm^{-1} is usually attributed to the stretching vibrations of hydrogen-bonded surface water molecules, adsorbed at face (1 0 1) of TiO_2 crystals, and to hydroxyl groups located close to each other [1-3]. This broad band is more intense for SG than for P25 and SA. It can be also observed a very small shoulder at around 3700 cm^{-1} that has been attributed to surface defects and isolated hydroxyl groups present on the face (0 0 1) [3]. These hydroxyl groups can interact with the oxygen surface groups of carbon nanotubes (e.g. carboxylic groups), creating Ti-O-C bonds in TiO_2/CNT composites.

6.1.1.2 X-ray diffraction (XRD)

XRD spectra for bare TiO_2 and respective composites are shown in Figure 6.2. The 2θ diffraction peaks at ca. 25.3°, 37.7°, 48.0° and 54.0° (marked as A in the XRD spectra) correspond to anatase crystalline phase. The major characteristic peak of rutile crystalline phase that appears at 27.4° (marked as R in the XRD spectra) is only detected for P25, as expected.

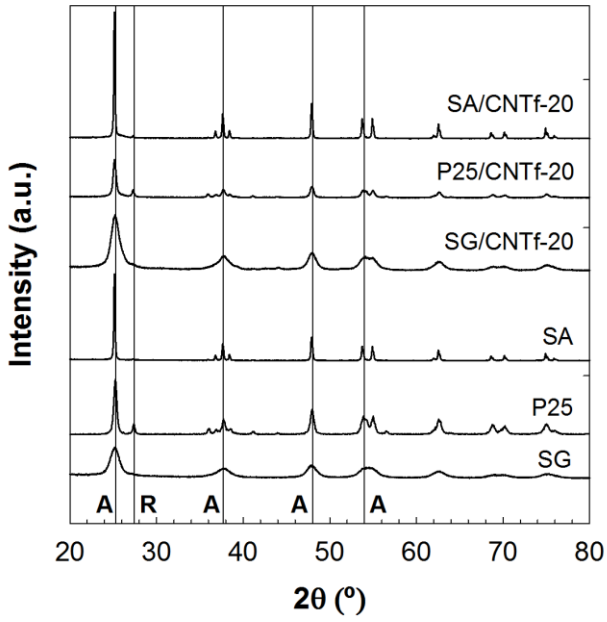

Figure 6.2 - XRD spectra for bare and respective TiO_2/CNT (XX/CNTf-20) composites.

The catalysts SG and SA consist of anatase crystalline phase with average crystallite sizes of around 9 nm and 50 nm, respectively, while P25 has both anatase and rutile phases. The average anatase crystallite sizes of TiO_2 is much larger for P25 (24 nm) and SA (50 nm) than for the SG material (9 nm) and about 2 times larger for SA than for P25. Remarkable differences were not observed by XRD when the TiO_2 materials were combined with carbon nanotubes.

6.1.1.3 Nitrogen adsorption-desorption isotherms

N_2 adsorption-desorption isotherms obtained at 77 K are represented in Figure 6.3 and the BET surface area calculated for each TiO_2 material and their respective composites are shown in Table 6.2.

Regarding the bare TiO_2 materials, SG has a higher S_{BET} (99 m^2 g^{-1}) than P25 (56 m^2 g^{-1}), while SA has the lowest S_{BET} (13 m^2 g^{-1}). The results obtained for S_{BET} (SG > P25 > SA) are in agreement with the observed TiO_2 particle sizes (SA > P25 > SG), *i.e.*, S_{BET} decreases with the increase of particle sizes.

Table 6.2 – S_{BET} ($\pm$ 5 m^2 g^{-1}) of the different TiO_2 powders (XX = P25, SA or SG) and for the respective TiO_2/CNT composites.

	XX	XX/CNTf-5	XX/CNTf-10	XX/CNTf-20	XX/CNT-10
P25	56	45	62	73	57
SA	13	17	22	25	15
SG	99	93	99	108	87

The isotherm for bare SG is Type IV with a hysteresis loop that can be ascribed to Type H2 accordingly to IUPAC classification [4].The isotherms of bare P25 and SA can be classified as Type II, with high N_2 uptake at high p/p_0. In all cases, as higher is the amount of CNTf introduced in the TiO_2 material, the higher the N_2 uptake at high relative pressures, while the determined S_{BET} values were similar or slightly higher for the composites (e.g., 22, 62, and 99 m^2 g^{-1} for SA/CNTf-10, P25/CNTf-10 and SG/CNTf-10, respectively) in comparison to bare TiO_2 materials. In fact, for the materials used in this work, porosity mainly refers to interparticle channels available for N_2 filling during isotherm assessment and, for this reason, the effect of the carbon nanotubes is mainly related with some deagglomeration of the TiO_2 particles.

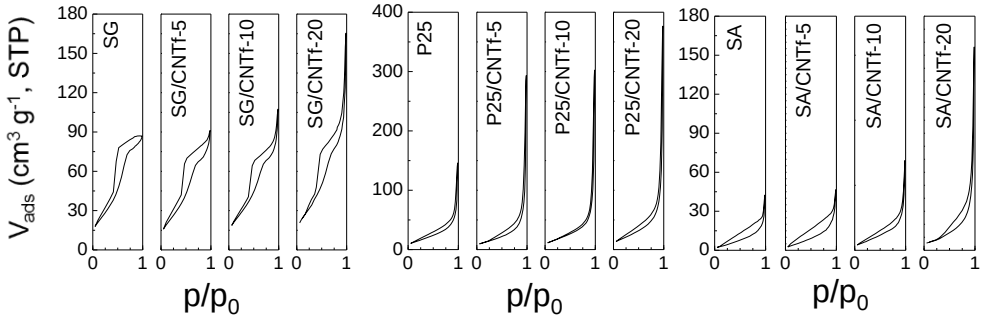

Figure 6.3 - N_2 adsorption-desorption isotherms for bare and respective TiO_2/CNT (XX/CNTf-20) composites.

As expected, introduction of the carbon phase on the TiO_2 matrix promoted the dispersion of the small nanoparticles, increasing the surface area in proportion with the CNT loading on the corresponding composites. It is relevant to note that there was no increase on the S_{BET} when the composites were prepared with non-functionalized CNTs. When functionalized CNTs were used the increase on the surface area for the same CNT loading was notorious, in particular for P25 and SA, where the measured increase was of 10 and 70%, respectively. It reinforces the relevance of a functionalization pre-treatment on the synthesis of TiO_2/CNT composites.

6.1.1.4 Electron microscopy

The representative SEM images of bare TiO_2 materials are shown in Figure 6.4 (a-c) for SG, P25 and SA and the corresponding arrangement with carbon nanotubes can be observed in Figure 6.4 (d-f). SG materials significantly differ from P25 and SA samples. TiO_2 crystallites are very small in the SG material (as determined by XRD) and seem to be strongly aggregated forming very large clusters of TiO_2 particles (Figure 6.4 a and 6.4 d), in contrast with materials prepared with P25 (Figure 6.4 b and 6.4 e) and SA (Figure 6.4 c and 6.4 f) which have higher crystallite sizes, due to the different routes of fabrication and, as consequence, resulting in different arrangements with carbon nanotubes. Therefore, TiO_2 crystallite sizes have a strong influence on the way as TiO_2 and carbon nanotubes are distributed in the composite. For the SG/CNTf-20 material (Figure 6.4 d) the contact between TiO_2 and carbon nanotubes is not as good as that obtained in P25/CNTf-20 (Figure 6.4 e) or in SA/CNTf-20 (Figure 6.4 f). For P25/CNTf-20 and SA/CNTf-20, carbon nanotubes seem to uniformly turn around TiO_2 particles, an indication of good assembling.

TEM micrographs of SG/CNTf-20, P25/CNTf-20 and SA/CNTf-20 are shown in Figure 6.4 (g-i), respectively. These images reinforce the previous observations made by SEM. SG crystallites synthesized through the sol-gel method (ca. 9 nm as determined by XRD) form big aggregates (a TiO_2 aggregate of 500 nm in size is shown in Figure 6.4 g), in this case the interaction between the TiO_2 crystallites and carbon nanotubes being weaker than in P25/CNTf-20 (Figure 6.4 h) or in SA/CNTf-20 (Figure 6.4 i).

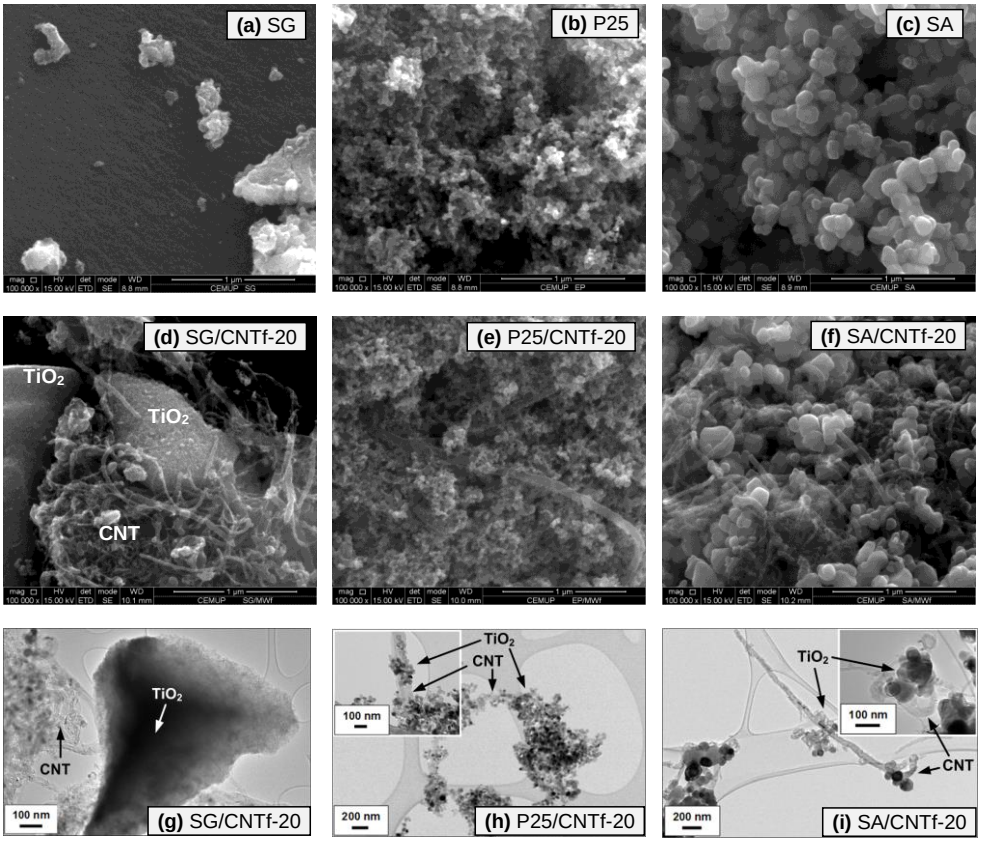

Figure 6.4 - (a-f) SEM and (g-i) TEM micrographs of bare TiO_2 materials and TiO_2/CNT composites.

Therefore, Figure 6.4 (d-i) show that particles distribution in TiO_2/CNT composites is clearly different depending on TiO_2 particle sizes. Among the prepared composites: (i) SG particles have the worst distribution since they usually form big aggregates with very weak interaction with the carbon phase; (ii) P25 based composites show a good distribution of TiO_2 particles along the walls of the carbon nanotubes; (iii) SA

particles also show a good contact with the carbon nanotubes and these particles are in some cases rolled up by the carbon nanotubes, as already observed in literature for TiO_2/CNT composites prepared with SA [5], due to their larger TiO_2 particle sizes (not observed for P25-based composites).

6.1.2 Photocatalytic experiments

As an emergent pollutant, caffeine was chosen to be the organic probe molecule for photocatalytic studies. It is a psychoactive substance widely consumed either in beverages or in pharmaceuticals and personal care products. It has been detected in natural watercourses [6] over many different countries, being used as a chemical marker for surface water pollution [7]. Caffeine is an antagonist of adenosine, thus its chemistry is dominated by radical adduct formation in the presence of oxidative radicals such as HO• [8]. Caffeine degradation studies are already reported in literature using TiO_2 and photo-Fenton approaches under solar conditions [9-12] and TiO_2 particles with magnetic properties modified with iron oxide under UV illumination [13]. However, to our knowledge, the photocatalytic degradation of this pollutant by using TiO_2/CNT composites is here firstly reported.

In addition, exploratory experiments to assess the feasibility of using catalytic films were performed with diphenhydramine (DP), another emerging pollutant which was studied in our group [14]. DP is a first generation antihistamine drug mainly used in the treatment of allergies as well as in many sleep aids which presents low biodegradability and high toxicity with mutagenic and carcinogenic effects [15].

6.1.2.1 Photocatalytic activity of bare TiO_2 materials in powder form

To ensure that the experimental results reflect caffeine disappearance in solution due to oxidative photocatalytic degradation, instead of the effect of the incident radiation on it, the absorption spectra of an organic aqueous solution (30 μM ~ 6 ppm) is depicted in Figure 6.5 together with the resulting emission lines when using the DURAN® 50 cut-off filter (see Section 2.2.1).

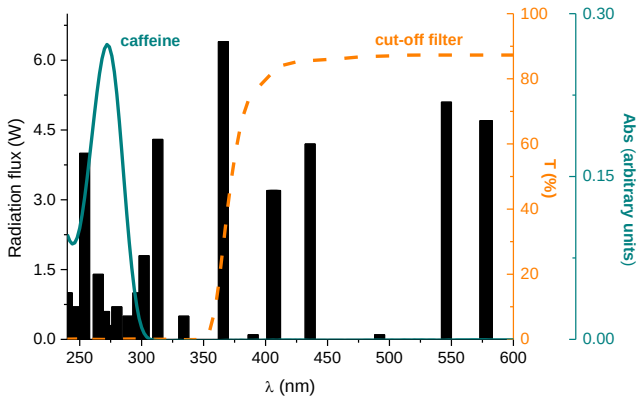

Figure 6.5 – Radiation flux of TQ 150 immersion lamp and transmission spectrum of the cut-off filter together with the absorption spectrum of aqueous caffeine.

According to the above figure, the emission lines reaching caffeine molecules (mainly at λ of 366, 406, 436, 546 and 578 nm) will not be absorbed, being instead used to generate the oxidative radicals involved on the pure photocatalytic mechanism (see Section 1.2.1), so photochemical contribution (direct photolysis) to the obtained conversions is not mathematically accounted.

The photocatalytic degradation of caffeine was first examined using bare TiO_2 materials. Figure 6.6 shows the caffeine concentration evolution in these photocatalytic experiments together with the results obtained for the non-catalytic run (photolysis). All tested catalysts markedly increased the caffeine degradation rate with respect to the non-catalytic experiment. The respective pseudo-first order kinetic constants (k) are shown in Table 6.1, namely $k = 4.9\times10^{-3}$, 26×10^{-3} and 123×10^{-3} min^{-1} for SG, SA and P25, respectively, against 0.36×10^{-3} min^{-1} for the pure photochemical regime. Both SG and SA consist of anatase crystalline form, but SA having the larger average anatase crystallite sizes of TiO_2 performs clearly better than SG. Even so, at the employed conditions, P25 (which consists of both anatase and rutile crystalline phases) is the most effective bare TiO_2 material for caffeine photocatalytic degradation.

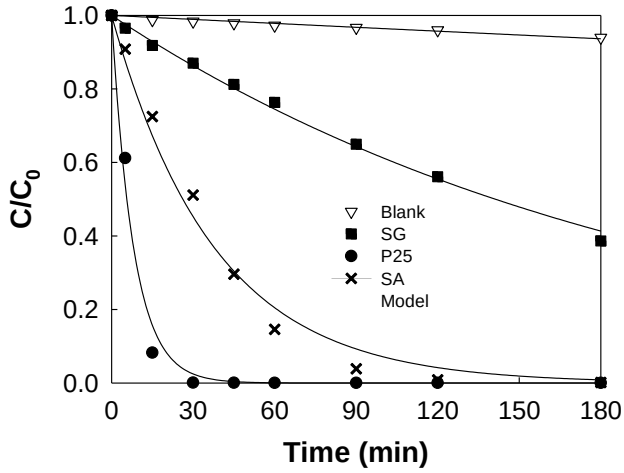

Figure 6.6 – Photolytic (blank) and photocatalytic degradation of caffeine over bare TiO_2 materials.

6.1.2.2 Photocatalytic activity of TiO_2/CNT composites in powder form

Figure 6.7 a-d show the photo-degradation profiles obtained with the TiO_2/CNT composites and in Figure 6.8 are represented the caffeine conversions after 30 min of irradiation. Figure 6.7 (a-c) show the caffeine concentration evolution in photocatalytic experiments as function of the CNT:TiO_2 ratio. It is possible to observe that carbon nanotubes have negligible effect on the activity of the SG material (see Figure 6.8), the pseudo-first order kinetic constants for SG-based materials being always very low ($5.55\times10^{-3} \pm 1.44\times10^{-3}$ min^{-1} in Table 6.1). Regarding P25-based materials, all have demonstrated to be very efficient on achieving high caffeine conversions; however, when carbon nanotubes are combined with P25, a significant decrease of the photocatalytic activity was always observed (see Figure 6.8), the pseudo-first order kinetic constant decreasing from 123×10^{-3} min^{-1} for bare P25 to under 83×10^{-3} min^{-1} for the respective composites, regardless the content of carbon nanotubes (Table 6.1). In contrast, the positive effect of functionalized carbon nanotubes on SA matrix is evident with the progressive increase on CNT loading as shown in Figure 6.8, the photocatalytic activity of SA ($k = 26\times10^{-3}$ min^{-1}) markedly increasing with the addition of CNTf: SA/CNTf-5 ($k = 53\times10^{-3}$ min^{-1}) < SA/CNTf-10 ($k = 63\times10^{-3}$ min^{-1}) < SA/CNTf-20 ($k = 77\times10^{-3}$ min^{-1}).

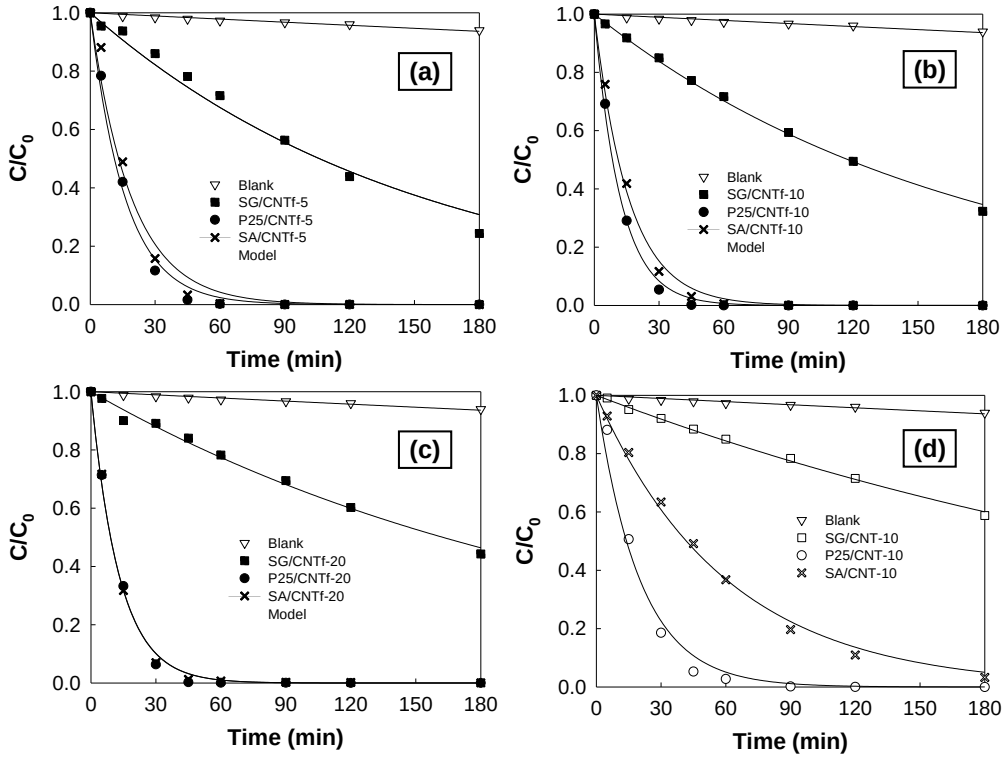

Figure 6.7 – Photolytic (blank) and photocatalytic degradation of caffeine over (a) XX/CNTf-5, (b) XX/CNTf-10, (c) XX/CNTf-20 and (d) XX/CNT-10 composites in powder form.

The photocatalytic degradation of caffeine using composites prepared with non-functionalized CNT (XX/CNT-10 in Figure 6.7 d) and functionalized CNT (XX/CNTf-10 in Figure 6.7 b) show that the oxygen groups introduced on carbon nanotubes play an important role in the catalytic activity of the prepared composites, corroborating characterization results (see Figure 6.3), with caffeine conversion for SA-based composites increasing from 23% (with pristine CNT) to 88% (with CNTf) in 30 min (see Figure 6.8), and the respective pseudo-first order kinetic constants from 16.6×10^{-3} to 63×10^{-3} min^{-1} (Table 6.1).

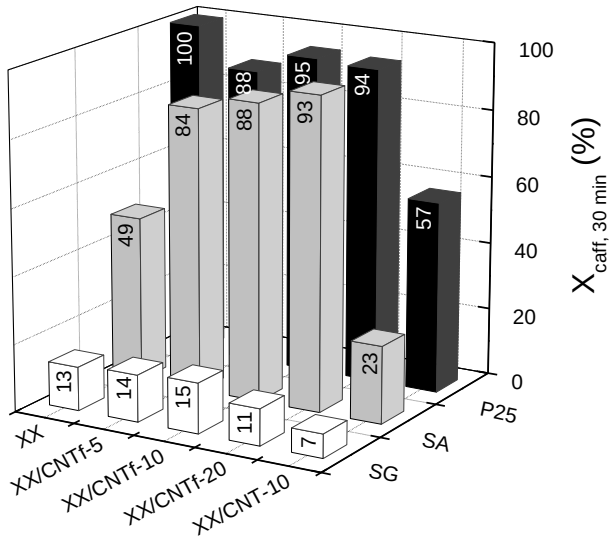

Figure 6.8 – Caffeine conversion after 30 min of irradiation, $X_{caff, 30 min}$ (%), for bare TiO_2 materials (XX = P25, SA, SG) and for the respective TiO_2/CNT composites.

This marked enhancement on the photocatalytic activity was also observed for P25-based composites (k = 50×10^{-3} and 83×10^{-3} min^{-1} for P25/CNT-10 and P25/CNTf-10, respectively) and less notorious for SG-based composites (k = 2.83×10^{-3} and 5.89×10^{-3} min^{-1} for SG/CNT-10 and SG/CNTf-10, respectively), as clearly shown in Figure 6.8. In fact, the applied nitric acid treatment introduces a considerable amount of oxygen groups in the poor surface of the pristine carbon nanotubes, which were identified by TPD analysis following a methodology described elsewhere [16]. The total amount of oxygen containing groups released as CO and CO_2, was of 1066 µmol g^{-1} and 434 µmol g^{-1}, respectively. The amount of phenols (evolved as CO) is 803 µmol g^{-1} and the amount of carboxylic acids (evolved as CO_2) is 289 µmol g^{-1}, which represent 55 and 20% of the total groups at the CNT surface, respectively. The remaining 25% correspond to the contribution of carboxylic anhydrides, carbonyl/quinones and lactones. Phenolic and carboxylic acid groups promote the dispersion of TiO_2 particles in TiO_2/CNT composites and are also expected for contributing to the formation of Ti-O-C bonds, as in esterification reactions between the carboxylic acid groups of CNTs and the hydroxyl groups of TiO_2 (observed by DRIFT analysis) [14].

The pseudo-first order kinetic constants obtained for SA and for the respective composites, including that prepared with non-functionalized CNT (SA/CNT-10) are

all represented in Figure 6.9, where the benefit of functionalized CNT on the photocatalytic activity of SA-based materials becomes clear.

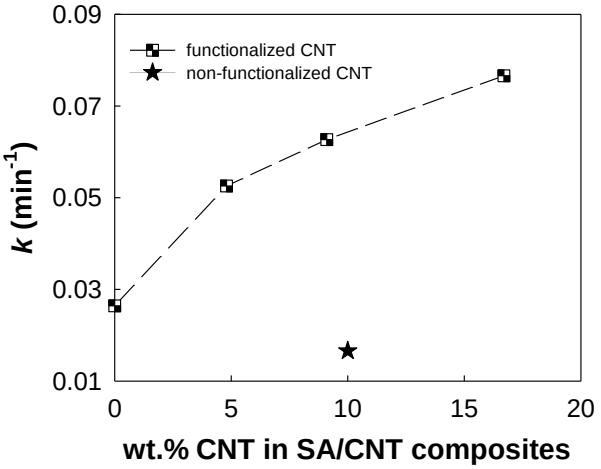

Figure 6.9 – Effect of CNT content on the pseudo-first order kinetic constant when using SA/CNTf-Y composites and comparison with SA and SA/CNT-10 materials. Curves represent the fitting of the pseudo-first order equation to the experimental data.

In conclusion, the larger TiO_2 crystallite sizes of SA lead to a good contact between the anatase TiO_2 particles and the carbon nanotubes, and the oxygen surface groups in carbon nanotubes are crucial on the high activity of these composites.

6.1.2.3 Photocatalytic degradation pathway

The main oxidative routes of the photocatalytic process were discriminated by using EDTA and *t*-BuOH, acting as scavengers for holes and radicals, respectively [17, 18]. Figure 6.10 a and b show the caffeine concentration evolution in these photocatalytic experiments for the bare P25 and SA materials, respectively, and the corresponding pseudo-first order kinetic constants are presented in Table 6.1.

These constants decrease for both SA (from 26×10^{-3} to 2.16×10^{-3} and 7.47×10^{-3} min^{-1} with EDTA and *t*-BuOH, respectively) and P25 (from 123×10^{-3} to 5.4×10^{-3} and 36.0×10^{-3} min^{-1} with EDTA and *t*-BuOH, respectively). Therefore, *t*-BuOH decreased the pseudo-first order kinetic constants for both TiO_2 materials, but the addition of EDTA reduced in a higher extent the caffeine photo-degradation. Regarding the

TiO_2/CNT composites, the pseudo-first order kinetic constant of SA/CNTf-20 decreased from 77×10^{-3} to 3.0×10^{-3} min^{-1} with EDTA and to 3.49×10^{-3} min^{-1} with *t*-BuOH (Figure 6.10 d and Table 6.1), while for P25/CNTf-20 the observed decrease was from 76×10^{-3} to 2.95×10^{-3} min^{-1} with EDTA and to 12.3×10^{-3} min^{-1} with *t*-BuOH (Figure 6.10 c and Table 6.1).

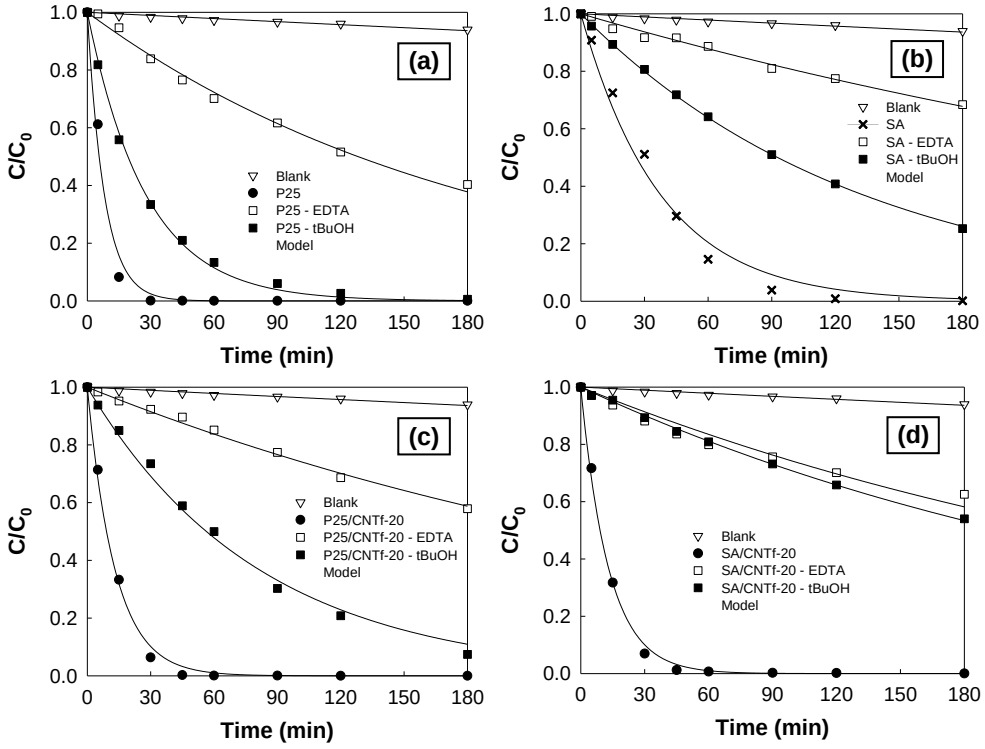

Figure 6.10 – Effect of holes/radicals scavengers (EDTA/*t*-BuOH) on the photocatalytic degradation of caffeine when using (a) P25, (b) SA, (c) P25/CNTf-20 and (d) SA/CNTf-20 as catalysts in powder form.

Therefore, photogenerated holes play a major role on this mechanism (both direct oxidation and through formation of reactive radicals), but free radicals produced by photoexcited electrons also participate in this mechanism and are particularly important when comparing the results obtained with SA/CNTf-20 and bare SA, since the reduction on the pseudo-first order kinetic constant with *t*-BuOH is more pronounced for SA/CNTf-20 (95% - from 77×10^{-3} to 3.49×10^{-3} min^{-1}) than for SA (71% - from 26×10^{-3} min^{-1} to 7.47×10^{-3} min^{-1}). From the results presented, carbon nanotubes seem to have a positive effect on the photocatalytic activity of SA by

increasing the ability to produce free oxidative radicals generated by photoexcited electrons.

6.1.2.4 Photocatalytic activity of TiO_2/CNT composites in film form

The separation of nanometric catalyst powders from the treated water requires critical separation steps that should be considered for the materials technological implementation. The associated short and long term implications of nanomaterials on the public health and environment are also a current major concern. Stabilization of these nanomaterials over adequate substrates, for instance in the form of films, is a possibility to overcome the drawback of the powders suspensions.

Given the results obtained with powder catalysts in suspension it was considered that the most promising composite for further studies is the one based on SA TiO_2 with the highest load on functionalized CNT, SA/CNTf-20, since the synergy resulting from the contact with the carbon phase was evident through characterization (see Figure 6.3 and Figure 6.4) and photocatalytic results (see Figure 6.8). Despite the significantly faster kinetics for original P25 when compared to bare SA (k = 123×10^{-3} and 26×10^{-3} min^{-1}, respectively, in Table 6.1), it is believed that the synergistic effects between phases for composite materials can gain relevance when these are supported in a substrate, since scattering effects and density properties cease to have meaning during reaction with catalysts in film form.

For this reason a set of experiments was carried out with a film prepared with the SA/CNTf-20 composite and the efficiency compared to that obtained with a film based on the benchmark P25. The method used to prepare the films consisted in the doctor blade technique, which is described in Section 6.3.3. The experimental conditions were the same used previously for the studies with powder catalysts, regarding light irradiation and the initial concentration of caffeine. More details on the experimental procedure is given in Section 2.2.2 of Chapter 2. Figure 6.11 a shows that the film made of SA/CNTf-20 has a significantly higher photocatalytic activity for caffeine degradation than that prepared with P25 (k = 8.3 × 10^{-3} and 5.6 × 10^{-3} min^{-1}, respectively).

For comparison purposes, a few exploratory experiments to assess the feasibility of using this type of films were also performed with diphenhydramine (DP). In line with the caffeine results, the pollutant abatement was faster with the SA/CNTf-20 film than with the one of P25 (12.0 × 10^{-3} and 7.0 × 10^{-3} min^{-1}, respectively), as shown in Figure 6.11 b.

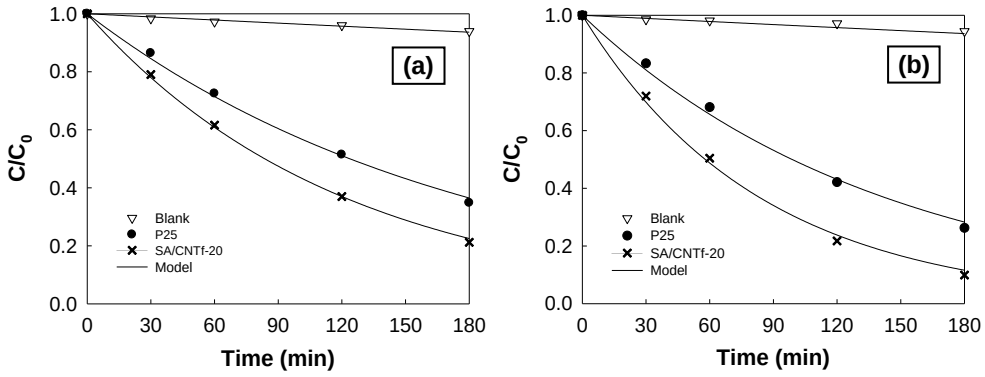

Figure 6.11 – Photocatalytic degradation of (a) caffeine and (b) diphenhydramine over P25 and SA/CNTf-20 catalysts in the form of films. Curves represent the fitting of the pseudo-first order equation to the experimental data.

Film characterization reveal a homogenous smooth and thin surface (ca. 3.75 µm) for the composite SA/CNTf-20, as shown in Figure 6.12 a. As described elsewhere [19], SA based films evidenced to be more homogeneous and thinner than P25 based ones, with a good interphase interaction between carbon and the semiconducting SA phase, most probably due to the larger nanoparticles (crystallite sizes SA 50 nm > P25 24 nm), then promoting electronic transitions in the visible range (λ > 400 nm), as shown in Figure 6.12 b.

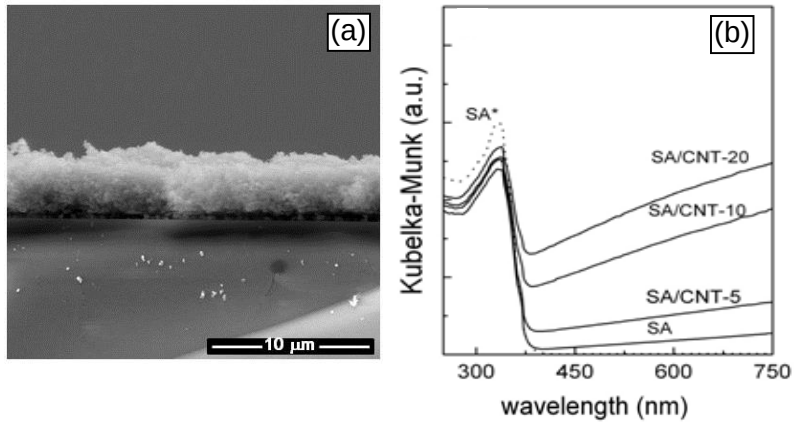

Figure 6.12 – SEM image of SA/CNT-20 sectional cut of the film (a); diffuse reflectance UV-Vis spectra of SA based films (b) and of the corresponding powder substrate (SA*) [19].

In fact, the increase in materials absorption seems to be proportional to the CNT loading and furthermore the absorption edge is shifted to higher wavelengths which indicates a progressive decrease in the band gap energy for the composite materials, in agreement with results for TiO_2/CNT powders reported in literature [20-22].

The motivation on choosing this composite as the base to produce the films was based on the activity of the bare SA TiO_2 which takes advantage of the synergy with the functionalized CNTs. It follows from the previous study with powder catalysts that SA/CNTf-20 films can be a promising solution on further studies with TiO_2 based materials modified with CNTs for technological applications, as they overcome the photocatalytic activity of the commercial benchmark P25 TiO_2 films on caffeine degradation.

In fact, all the powder composites prepared in this study were further deposited and tested in films on the photo-degradation of 10 mg L^{-1} of methylene blue, which is a model compound commonly used on photocatalysts screening reactions [23-26] . The activity of all the films prepared with basis on SA TiO_2 was systematically higher than those based on P25 (conversions for methylene blue after 60 min of irradiation: e.g. 89% for SA/CNTf-20 and 74% for P25) [19].

A deeper knowledge on the improvement of TiO_2 photo-activity by promoting the quality of the interphase with the CNTs was investigated by synthesizing new composites [27]. The traditional sol-gel method was used to prepare composites by including the CNTs directly on the ageing step of the sol, to be compared with their analogues prepared by hydration-dehydration (SG/CNT) referred in the above Section 6.3.2. The powders were deposited in glass slides through the doctor blade technique and tested for the photocatalytic degradation of methylene blue solutions of 10 mg L^{-1}. The objective was to search for the advantage on including the carbon phase during the formation of the TiO_2 matrix enhancing the quality of the created interphase, with the possibility of decoration of CNTs sidewalls with smaller TiO_2 nanoparticles, especially with functionalized CNTs, avoiding the formation of the big aggregates previously observed in Figure 6.4 g.

As expected, the characterization results revealed that the interphase between the TiO_2 and the CNTs is significantly improved when the CNTs are included during the formation of the sol and especially when these are previously functionalized, corroborating all the previous results about the advantage on having the CNT walls decorated with oxygen functionalities representing anchoring points for the TiO_2 nanoparticles. The observed aggregates of TiO_2 nanoparticles are appreciably

shortened when the composites are synthesized by sol-gel instead of being prepared by the hydration-dehydration method and a much more homogeneous catalyst is obtained even when using the non-functionalized CNTs [27]. The achievement of catalysts with a homogeneous distribution of the phases counteracting the segregation observed for composites prepared by hydration-dehydration, allows a good electronic interphase and consequently results in a most effective yield on charge separation, leading to higher photocatalytic activities, at variance with high rates of electron-hole recombination occurring in bulk aggregates with low photonic yield on the degradation process.

The photocatalytic results for the films on the degradation of methylene blue after 60 min of irradiation have, in fact, corroborated what was observed through characterization analysis [27]. Accordingly to the results obtained with SG/CNT catalysts in the photocatalytic degradation of caffeine (see Figure 6.8), the functionalization of CNT resulted in higher activities for the films on the degradation of methylene blue either for the composites prepared by hydration-dehydration (58% > 33%) or sol-gel methods (62% > 53%). Even comparing the activity of the films prepared with non-functionalized CNTs by the different methods, the higher efficiency for the sol-gel synthesis was clear (53% > 33%). Despite the results obtained with bare TiO_2 films with higher conversions for the composites prepared through hydration-dehydration (59% > 46%), the synergy with the carbon phase was clearly developed through the sol-gel synthesis for composites prepared with high amounts of functionalized CNTs (62% > 58%). Once again the results obtained with the aforementioned films were higher than those obtained for the films of P25 with a conversion of 53%.

It is then possible to conclude that the behavior of catalysts on powder suspensions cannot be directly related with their performance in the form of films. Photocatalysis in suspensions is favored when catalysts have low density, showing a good distribution in solution and a high contact with the organics to be degraded. However, when the catalysts are supported in substrates, density is no more an issue and other properties gain relevance for the inherent oxidative photocatalytic mechanism, namely the synergy with a carbon phase which can act as a dispersing agent for TiO_2 nanoparticles, as co-adsorbent or as photosensitizer [20, 22, 28].

Composites prepared by the traditional sol-gel method showed better results when tested in films, in comparison with those prepared through hydration-dehydration, unveiling that an intimate contact between TiO_2 and CNTs can be created, resulting in homogeneous composites with a good interphase and light response in the

near-UV to visible range with lower band gaps, even overcoming the results obtained in films with the benchmark P25 [27].

In a recent study developed to shed light on the interdependency of the photocatalytic efficiency and the interface properties of the TiO_2/CNT composites prepared by the hydration-dehydration method (referred on Section 6.3.2), important conclusions could be obtained [29]. A new liquid nitrogen porosimetry methodology was proposed to assess catalysts photo-efficiency on the degradation of aqueous caffeine as function of their mixing quality in the synthesized composites, supported on complementary characterization analysis. In particular, Raman analysis concluded to the absence of any interfacial interaction. As expected, in the absence of synergetic effects the photocatalytic efficiency correlated well with the extent of mixing between the CNTs and TiO_2 phases.

From this point on, further insights on the development of methods to synthesize TiO_2/CNT composites are needed in order to improve the quality of the interphase created between both phases, taking advantages of the intimate contact at electronic level to give an effective response to what the photocatalytic mechanism involves. As discussed previously, the traditional sol-gel method to synthesize TiO_2 nanoparticles in the presence of functionalized CNTs is a good start point to future studies aiming high efficiencies on the degradation of different organic pollutants with supported catalysts [27].

6.2 Conclusions

Three different TiO_2 materials (P25, SA, SG) were studied as a basis to produce TiO_2/CNT composites with improved photo-efficiency on the near-UV to visible region for the photocatalytic degradation of caffeine, as a model compound. All the prepared composites revealed photocatalytic activity towards the chosen reactions.

DRIFT analysis revealed the presence of hydroxyl groups at the surface of all the TiO_2 materials. The hydroxyl groups of TiO_2 interact with oxygen groups on the carbon nanotubes surface (e.g. carboxylic groups), creating Ti-O-C bonds on the TiO_2/CNT composites. Therefore, CNTs were successfully functionalized through a nitric acid boiling method creating a modified chemical surface populated with hydroxyl and carboxylic groups which can, by esterification reactions, bond with TiO_2 nanoparticles.

The average crystallite size and crystalline phases of the TiO_2 catalysts was investigated by XRD showing that SG and SA are pure anatase with crystallite sizes of 9 and 50 nm, respectively, and P25 constituted as a mix of anatase and rutile phases with an average crystallite size of 24 nm.

The surface area of the composites increased with CNT loading, especially when using functionalized CNTs. This was due to promoted dispersion of the TiO_2 nanoparticles, following the introduction of the carbon phase in the semiconductor matrix.

The SG particles form big aggregates with a very weak interaction with the carbon phase. On the other hand, a good mixture is observed in the case of the big SA particles which are in some cases rolled up by the CNTs. Finally, the P25 based composites show also a good distribution of the smaller nanoparticles along the walls of the CNTs.

The photocatalytic oxidation of caffeine could be ascribed to a pseudo-first order kinetic model with the reference catalysts having the following order for the kinetic constant: $k = 4.9\times10^{-3}$, 26×10^{-3} and 123×10^{-3} min^{-1} for SG, SA and P25, respectively.

Despite the higher activities for P25 based composites, SA TiO_2 was the catalyst which markedly took benefit of the combination with the carbon phase. Furthermore, its photo-efficiency increased with CNTs loading. In addition, functionalized CNTs gave rise to much more active photocatalysts.

Selective trapping of photogenerated holes and radicals allowed concluding that holes play a major role in this reaction mechanism however, for SA based materials, the mechanism seems to undergo a different pathway since free radicals produced by photo-excited electrons appears to be responsible for the higher activity of SA/CNTf-20 in comparison to bare SA.

When used in the film form SA/CNTf-20 was the most efficient photocatalyst for caffeine degradation, better than that prepared with P25.

Photocatalytic results on the degradation of methylene blue with the composites in film form, demonstrate that the synergy between TiO_2 and CNTs is markedly developed in the case of composites prepared by the sol-gel technique as compared to the materials prepared by hydration-dehydration.

The performance of the composites prepared by hydration-dehydration is directly correlated to the quality of the mixing between TiO_2 and CNTs phases. However, it

is not due to the existence of a good interphase interaction, as confirmed by the Raman analysis.

From the gathered evidence is obvious that the hydration-dehydration method has a poor contribution to the creation of a real interphase interaction. The traditional sol-gel method revealed to be a good synthesis procedure.

It follows from the above that the selection of the synthesis procedure must be rigorously complemented with a deep characterization of the materials, especially based on Raman spectroscopy to evaluate the interphase interaction. Once confirmed the advantage of using a particular TiO_2 in combination with CNTs, in powder suspensions, reactions with supported catalysts should be finally performed on the photo-degradation of different organic molecules, mixtures and finally real effluents.

6.3 Experimental section

Multi-walled CNT structures were chosen for the synthesis of TiO_2 based composites, in detriment of SWCNTs, because of their higher thermal stability and the favored evolution of acidic groups, namely carboxylic acids which are of interest for covalent bonds with TiO_2, under HNO_3 oxidation. MWCNTs synthesized by chemical vapor deposition (CVD) were purchased from Shenzhen Nanotechnologies Co. Ltd. (purity ≥ 95%, main range of diameter < 10 nm, length = 5-15 μm, ash content ≤ 0.2 wt%, amorphous carbon < 3%).

Three different types of TiO_2 powders were used: (i) TiO_2 synthesized through a modified acid catalyzed sol-gel method (SG); (ii) benchmark TiO_2 from Evonik Degussa Corporation (P25); (iii) commercial TiO_2 from Sigma-Aldrich (SA).

6.3.1 Functionalization of CNTs

Accordingly to the previous study on the functionalization of CNTs, MWCNTs were elected to be functionalized by boiling nitric acid to preserve the required carboxylic acids for TiO_2/CNT composites preparation. 0.5 g of the pristine MWCNTs were immersed in 150 mL of a HNO_3 solution with a concentration of 10.0 mol L^{-1} in a round bottom flask equipped with a condenser. The suspension was heated to boiling temperature and kept under magnetic stirring for 3 h. After cooling, the suspension

was washed up and the powder was recovered and stored after being dried overnight at 383 K. Functionalized CNTs are here designated as CNTf.

6.3.2 Sol-gel synthesis of TiO_2 and preparation of TiO_2/CNT composites

TiO_2 (SG) was prepared by an acid catalyzed sol-gel method, as described elsewhere [30]. An alkoxide precursor Ti $(OC_3H_7)_4$ (Aldrich, 97 %) was dissolved in ethyl alcohol (Panreac, 99.5 %) under magnetic stirring and the reaction was catalyzed by adding HNO_3 (Fluka, 65 wt. %). The mixture was loosely covered and kept under stirring until a homogeneous gel was formed. The gel was aged in air for several days and when completely dried was crushed into fine powder. To obtain pure crystalline anatase phase, the powder was calcined in nitrogen for 2 h at 673 K before being stored.

The composite powders were prepared by a simple hydration/dehydration method adapted from procedures described in literature [5, 31]. Briefly, CNTs were dispersed in 1 L of distilled water under sonication and then TiO_2 added under stirring, the mixture heated at 353 K until complete evaporation of water and the resulting composite dried overnight at 383 K. The composites prepared with functionalized CNT and different TiO_2 powders were made at different mass ratios. These composites are labelled as XX/CNTf-Y, where XX is the type of TiO_2 used (SG, SA or P25) and Y (5, 10 or 20) is the mass of CNTf per 100 mass units of bare TiO_2, giving approximately 5, 9 and 17 wt.% of CNTf. Composites were also prepared with pristine CNTs using the three different TiO_2 powders at a fixed mass ratio (XX/CNT-10). Major emphasis is given in the present work to materials prepared with 17 wt.% of CNTf, since the highest photocatalytic activities for degradation of different pollutants if often found near this ratio [28].

6.3.3 Preparation of photocatalytic films

Selected materials were also prepared on glass slides as films using the doctor blade technique, as described elsewhere [19]. Briefly, glass slides of 1.5 cm diameter are coated on one side with different pastes of each material. For each powder catalyst, a paste was prepared by mixing 50 mg with 1.5 mL of a solution constituted by acetone (10.0 mL), α-terpineol (5.0 mL) and ethylcellulose (0.3 g). The mixture was left under stirring during 24 h in a closed vial and then the vial was opened until solvent evaporation for another 24 h. On a freshly cleaned transparent glass slide the paste was spread using the doctor blade technique by limiting the surface to be

covered with the catalyst by two parallel stripes of adhesive tape, in order to obtain an area of 1.0 × 1.0 cm. After deposition over the glass slides the films were calcined at 723 K for 2 h.

6.3.4 Materials characterization

The structure of materials surface was investigated by Diffuse Reflection Infrared Fourier Transformed (DRIFT) spectroscopy and the interferograms are presented in Kubelka-Munk scale. The morphology and the phase dispersion on the composites were observed by scanning electron microscopy (SEM) and transmission electron microscopy (TEM) analysis. Crystalline phases and crystallite sizes on bare TiO_2 materials and the respective composites were determined through X-ray diffraction (XRD) analysis. BET surface area (S_{BET}) of the prepared materials was determined from N_2 adsorption-desorption isotherms obtained at 77 K. The amount of oxygen groups introduced on the pristine CNTs surface was quantified through temperature programmed desorption (TPD) analysis. Caffeine absorption spectrum was collected by UV-Vis spectroscopy. Details on the conditions under which the analyses took place are described in Chapter 3.

6.3.5 Photocatalytic experiments

Photocatalytic experiments with powders were conducted in a glass-immersion photochemical reactor equipped with a UV-Vis Heraeus TQ 150 medium pressure mercury vapour lamp located axially and held in a quartz immersion tube, as depicted in Figure 2.2 in Section 2.2.1 of Chapter 2. A DURAN 50® glass jacket was used for cool water circulation to maintain a constant temperature, acting also as an optical cut-off of UVB and UVC irradiation (λ > 350 nm). The reactor was charged with a fixed amount of each catalyst (1.0 g L^{-1}) and with 250 mL of a caffeine solution (50 mg L^{-1}) continuously bubbled with a 20 vol.% of oxygen. A series of preliminary experiments was performed using four different catalyst loads of bare P25, SA and SG materials (0.8, 0.9, 1.0 and 1.1 g L^{-1}), that were selected having into account the minimum TiO_2 content used on 1 g L^{-1} of a TiO_2/CNT composite (i.e., ca. 0.8 g L^{-1} for XX/CNTf-20). The results obtained were similar with a given material for different catalyst loads (deviations lower than 5%), indicating that the reaction rate was independent on the amount of TiO_2 at these conditions.

Dark experiments were performed to establish the period of time needed to achieve the adsorption-desorption equilibrium for the prepared materials and to determine t = 0 for the photocatalytic reactions (instant to turn on the irradiation). An experiment in the absence of catalyst was also performed as blank in order to calculate the contribution from direct photolysis. Photocatalytic tests with caffeine were also conducted employing hole and radical trapping agents (10 mM of EDTA and *t*-BuOH, respectively) with the aim to study the photocatalytic reaction mechanism. Some materials were also tested in the form of films, and in this case a smaller reactor was used maintaining the operating conditions and radiation source, accordingly to the procedure and experimental setup described in detail in Section 2.2.2 of Chapter 2.

Experimental data revealed that the photocatalytic oxidation of caffeine could be ascribed to a pseudo-first order kinetic model, as described by the following equation:

$$\boldsymbol{C = C_0 e^{-k \cdot t}} \quad (1)$$

where *C* corresponds to pollutant concentration, *k* is the pseudo-first order kinetic constant, *t* is the reaction time and C_0 is the pollutant concentration for t = 0. The *k* values (Table 6.1) were obtained by non-linear regression, fitting Eq. (1) to the normalized caffeine concentration evolution (C/C_0). The used Marquardt-Levenberg algorithm seeks the values of the parameters that minimize the sum of the squared differences between observed and predicted values of the dependent variable (the tolerance was set at 1×10^{-10}). The standard error of each estimated *k* parameter and the respective regression coefficient of the model (r^2) are shown in Table 6.1 and indicate in general good fitting of the model to the experimental data.

Samples were periodically withdrawn, centrifuged and analyzed by High Performance Liquid Chromatography (HPLC) with a mobile phase consisting on ultra-pure water and methanol. Caffeine concentration was determined at the maximum absorption wavelength (274 nm). This absorbance was found to be linear over the whole considered range (a maximum relative standard deviation of 2%).

6.4 References

[1] Gao Y, Masuda Y, Seo W-S, Ohta H, Koumoto K. TiO2 nanoparticles prepared using an aqueous peroxotitanate solution. Ceram Int. 2004; 30 (7):1365-8.

[2] Comparelli R, Fanizza E, Curri ML, Cozzoli PD, Mascolo G, Passino R, et al. Photocatalytic degradation of azo dyes by organic-capped anatase TiO2 nanocrystals immobilized onto substrates. Appl Catal B-Environ. 2005; 55 (2):81-91.

[3] Araña J, Doña-Rodríguez JM, Portillo-Carrizo D, Fernández-Rodríguez C, Pérez-Peña J, González Díaz O, et al. Photocatalytic degradation of phenolic compounds with new TiO2 catalysts. Appl Catal B-Environ. 2010; 100 (1–2):346-54.

[4] Sing KSW, Everett DH, Haul RAW, Moscou L, Pierotti RA, Rouquerol J, et al. Reporting Physisorption Data for Gas Solid Systems with Special Reference to the Determination of Surface-Area and Porosity (Recomendations 1984). Pure Appl Chem. 1985; 57 (4):603-19.

[5] Yao Y, Li G, Ciston S, Lueptow RM, Gray KA. Photoreactive TiO2/Carbon Nanotube Composites: Synthesis and Reactivity. Environ Sci Technol. 2008; 42 (13):4952-7.

[6] Metcalfe CD, Miao X-S, Koenig BG, Struger J. Distribution of acidic and neutral drugs in surface waters near sewage treatment plants in the lower Great Lakes, Canada. Environ Toxicol Chem. 2003; 22 (12):2881-9.

[7] Buerge IJ, Poiger T, Müller MD, Buser H-R. Caffeine, an Anthropogenic Marker for Wastewater Contamination of Surface Waters. Environ Sci Technol. 2003; 37 (4):691-700.

[8] P. Telo J, J. S. C. Vieira A. Mechanism of free radical oxidation of caffeine in aqueous solution. J Chem Soc, Perkin Trans 2. 1997; (9):1755-8.

[9] Bernabeu A, Vercher RF, Santos-Juanes L, Simón PJ, Lardín C, Martínez MA, et al. Solar photocatalysis as a tertiary treatment to remove emerging pollutants from wastewater treatment plant effluents. Catal Today. 2011; 161 (1):235-40.

[10] Klamerth N, Malato S, Maldonado MI, Agüera A, Fernández-Alba AR. Application of Photo-Fenton as a Tertiary Treatment of Emerging Contaminants in Municipal Wastewater. Environ Sci Technol. 2010; 44 (5):1792-8.

[11] Klamerth N, Miranda N, Malato S, Agüera A, Fernández-Alba AR, Maldonado MI, et al. Degradation of emerging contaminants at low concentrations in MWTPs effluents with mild solar photo-Fenton and TiO2. Catal Today. 2009; 144 (1–2):124-30.

[12] Klamerth N, Rizzo L, Malato S, Maldonado MI, Agüera A, Fernández-Alba AR. Degradation of fifteen emerging contaminants at μg L−1 initial

concentrations by mild solar photo-Fenton in MWTP effluents. Water Res. 2010; 44 (2):545-54.

[13] Álvarez PM, Jaramillo J, López-Piñero F, Plucinski PK. Preparation and characterization of magnetic TiO2 nanoparticles and their utilization for the degradation of emerging pollutants in water. Appl Catal B-Environ. 2010; 100 (1–2):338-45.

[14] Pastrana-Martínez LM, Morales-Torres S, Likodimos V, Figueiredo JL, Faria JL, Falaras P, et al. Advanced nanostructured photocatalysts based on reduced graphene oxide–TiO2 composites for degradation of diphenhydramine pharmaceutical and methyl orange dye. Appl Catal B-Environ. 2012; 123–124 (0):241-56.

[15] Kinney CA, Furlong ET, Werner SL, Cahill JD. Presence and distribution of wastewater-derived pharmaceuticals in soil irrigated with reclaimed water. Environ Toxicol Chem. 2006; 25 (2):317-26.

[16] Figueiredo JL, Pereira MFR, Freitas MMA, Órfão JJM. Modification of the surface chemistry of activated carbons. Carbon. 1999; 37 (9):1379-89.

[17] Minero C, Mariella G, Maurino V, Vione D, Pelizzetti E. Photocatalytic Transformation of Organic Compounds in the Presence of Inorganic Ions. 2. Competitive Reactions of Phenol and Alcohols on a Titanium Dioxide−Fluoride System. Langmuir. 2000; 16 (23):8964-72.

[18] Serpone N, Texier I, Emeline AV, Pichat P, Hidaka H, Zhao J. Post-irradiation effect and reductive dechlorination of chlorophenols at oxygen-free TiO2/water interfaces in the presence of prominent hole scavengers. J Photochem Photobiol A-Chem. 2000; 136 (3):145-55.

[19] Sampaio MJ, Silva CG, Marques RRN, Silva AMT, Faria JL. Carbon nanotube–TiO2 thin films for photocatalytic applications. Catal Today. 2011; 161 (1):91-6.

[20] Wang W, Serp P, Kalck P, Faria JL. Photocatalytic degradation of phenol on MWNT and titania composite catalysts prepared by a modified sol–gel method. Appl Catal B-Environ. 2005; 56 (4):305-12.

[21] Wang W, Serp P, Kalck P, Faria JL. Visible light photodegradation of phenol on MWNT-TiO2 composite catalysts prepared by a modified sol–gel method. J Mol Catal A: Chem. 2005; 235 (1–2):194-9.

[22] Gao B, Chen GZ, Li Puma G. Carbon nanotubes/titanium dioxide (CNTs/TiO2) nanocomposites prepared by conventional and novel surfactant wrapping sol–gel methods exhibiting enhanced photocatalytic activity. Appl Catal B-Environ. 2009; 89 (3–4):503-9.

[23] Kwon CH, Shin H, Kim JH, Choi WS, Yoon KH. Degradation of methylene blue via photocatalysis of titanium dioxide. Mater Chem Phys. 2004; 86 (1):78-82.

[24] Kim SY, Lim TH, Chang TS, Shin CH. Photocatalysis of methylene blue on titanium dioxide nanoparticles synthesized by modified sol-hydrothermal process of TiCl4. Catal Lett. 2007; 117 (3-4):112-8.

[25] Xiong L, Sun W, Yang Y, Chen C, Ni J. Heterogeneous photocatalysis of methylene blue over titanate nanotubes: Effect of adsorption. J Colloid Interface Sci. 2011; 356 (1):211-6.

[26] Hwang KJ, Lee JW, Shim WG, Jang HD, Lee SI, Yoo SJ. Adsorption and photocatalysis of nanocrystalline TiO 2 particles prepared by sol-gel method for methylene blue degradation. Adv Powder Technol. 2012; 23 (3):414-8.

[27] Sampaio MJ, Marques RRN, Tavares PB, Faria JL, Silva AMT, Silva CG. Tailoring the properties of immobilized titanium dioxide/carbon nanotube composites for photocatalytic water treatment. Journal of Environmental Chemical Engineering (JECE). 2013; 1 (4):945-53.

[28] Silva CG, Faria JL. Photocatalytic Oxidation of Phenolic Compounds by Using a Carbon Nanotube-Titanium Dioxide Composite Catalyst. ChemSusChem. 2010; 3 (5):609-18.

[29] Miranda SM, Romanos GE, Likodimos V, Marques RRN, Favvas EP, Katsaros FK, et al. Pore structure, interface properties and photocatalytic efficiency of hydration/dehydration derived TiO2/CNT composites. Appl Catal B-Environ. 2014; 147:65-81.

[30] Silva CG, Faria JL. Anatase vs.rutile efficiency on the photocatalytic degradation of clofibric acid under near UV to visible irradiation. Photochem Photobiol Sci. 2009; 8 (5):705-11.

[31] Vijayan BK, Dimitrijevic NM, Finkelstein-Shapiro D, Wu J, Gray KA. Coupling Titania Nanotubes and Carbon Nanotubes To Create Photocatalytic Nanocomposites. ACS Catalysis. 2011; 2 (2):223-9.

Part V

A photocatalytic system to study the activity of powdered or immobilized catalysts

7 Assembling and validation of a customized photocatalytic system for water remediation studies using caffeine as model compound

In a heterogeneous photocatalytic process the kinetics are influenced by main physical parameters namely mass of catalyst, wavelength of the irradiated light, initial concentration of the compound in study, temperature during reaction and radiant flux reaching the catalyst. It is therefore relevant to create conditions where these parameters can be studied with accuracy and their effects assessed for a given system.

A new customized setup was assembled with the goal of improving some limitations detected in the system used in Chapter 6 (with the small cylindrical reactor), namely the inefficiency on the usage of light given the dimensions of the arc of the lamp. In this new setup, it was used a high-pressure mercury vapor lamp with an arc of comparable dimensions to the photo-reactor. Optical elements like an optical window and a biconvex lens were included to optimize the usage of light in the photocatalytic process, by focusing the emitted light beam on the photo-reactor. This strategy allows maintaining the wavelength distribution of the beam, with maximum transmittance. Optical filters can also be used to study catalysts activity at different wavelengths, approaching to sunlight conditions in solar-driven applications. Optical characterization and validation of preliminary results in caffeine photocatalytic degradation with suspensions of the benchmark TiO_2 P25 (Evonik Degussa Corporation) were obtained. The system configuration was optically characterized and tested at different conditions with or without optical accessories and the reactor positioned at different distances from the irradiation source. Optimal conditions for P25 suspensions were obtained: 1.0 g L^{-1} of catalyst load being irradiated under near-UV to visible light (350 – 600 nm) through the optical lens with the photo-reactor positioned at 17 cm to the lamp. This setup is available to study photocatalytic degradation in aqueous systems either with suspensions or supported catalysts under different irradiating conditions with optimized usage of the emitted light.

7.1 Results and discussion

Several photo-reactors for wastewater treatment have been thoroughly reviewed [1]. In the present study, the new photocatalytic system was assembled taking into account some of the published scientific recommendations on photo-reactors configuration and process intensification regarding efficiency of illumination and mass transfer limitations [1-5].

In fact, efficiency on the light usage is one of the most important parameters with a strong influence on photocatalytic studies. This new setup was designed to make up for the inadequacy of dimensions between the arc of the immersion lamp and the small cylindrical photo-reactor used in Chapter 6 (see Section 2.2.2 in Chapter 2). The small photo-reactor with an exposed surface of 3.14 cm^2 can now be positioned at well-defined distances from the light source to evaluate the effect on photocatalytic results, as irradiance decreases inversely with the square of the distance from the source [4]. Intensification of the photocatalytic system was accomplished by using an optical accessory, namely a biconvex lens, for focusing the light beam over the reactor exposed surface with a uniform distribution of the transmitted wavelengths in relation to the spectrum originally emitted from the light source. The application of various optical filters at very well defined distances, to simulate specific spectral conditions, is also possible. The two main configurations for photocatalytic reactors vary on the state of the catalyst: suspended photocatalyst particles or immobilized onto an inert support. Mass transfer limitations are minimized when photocatalytic reactions are conducted with catalyst suspensions but with the main drawback of requiring for the solid phase additional post separation processes, besides difficulties either due to eventual particle aggregation or the preclusion to operation in continuous mode. In this sense, supported catalysts have been studied over different supports on diverse photo-reactors configurations representing a way out to overcome the catalyst separation step [1, 6-8]. Though, increased mass transfer limitations rise up over the catalyst immobilized layers.

7.1.1 Assembling of the customized photocatalytic reaction system

The HPK125W lamp here in use is a high pressure mercury vapor lamp with similar spectral emission lines when compared to the TQ150 lamp used in the photocatalytic studies discussed in the previous Chapter 6, as shown in Figure 7.1 a. However, it is more suitable to the dimensions of the small cylindrical reactor since the arc has an adequate scale of ca. 3 cm (Figure 7.1 b).

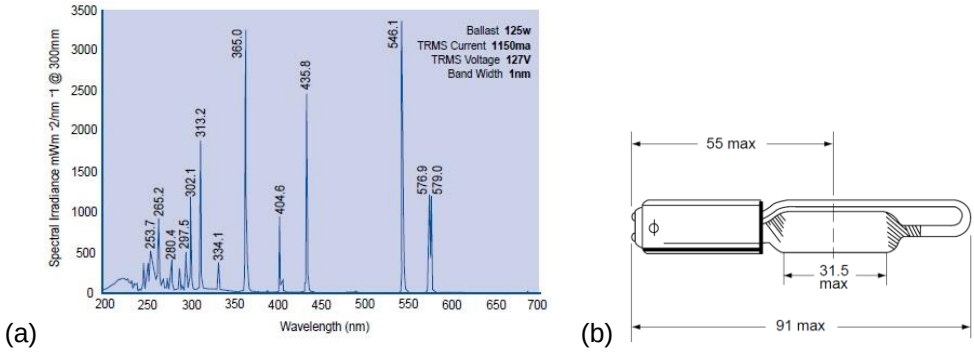

Figure 7.1 – HPK125W emission lines (a) and lamp dimensions in mm (b).

In this new setup, the lamp is enclosed in an aluminum box separated from the environment of the photo-reactor, allowing it to be turned on and stabilize the emitted radiation during the dark adsorption phase without reaching the aqueous solution inside the photo-reactor, as shown in Figure 7.2. After reaching adsorption/desorption equilibrium, an optical window (OW) is opened and the illumination starts at constant radiant flux. The aqueous solutions inside the photo-reactor are magnetically stirred and bubbled with air to provide the molecular oxygen involved on the photocatalytic reaction mechanism, as described in Section 1.2.1 of Chapter 1. When the lamp is turned on and the light passes through the OW it can be intersected by optical elements before reaching the photocatalytic reactor, like the biconvex lens (BL) or optical filters to create specific spectral conditions. A black tunnel is used to block the light to the outside of the photocatalytic system for user's protection from skin and ocular injuries.

A user manual containing a detailed procedure for this specific photocatalytic setup has been produced, emphasizing some notes and cautions to have in consideration while operating and is given in Appendix B.1.

Given the abovementioned considerations, this photocatalytic system was designed to study both the activity of catalyst suspensions and immobilized catalysts on thin glass round slides. The development of photocatalysts can be rapidly assessed in terms of their photo-activity in aqueous suspensions and for the elected materials thin films can then be tested in the same setup, even under continuous operation. The system was optically characterized regarding optical spectrum evolution with the distance to the lamp, absolute irradiance and wavelength distribution.

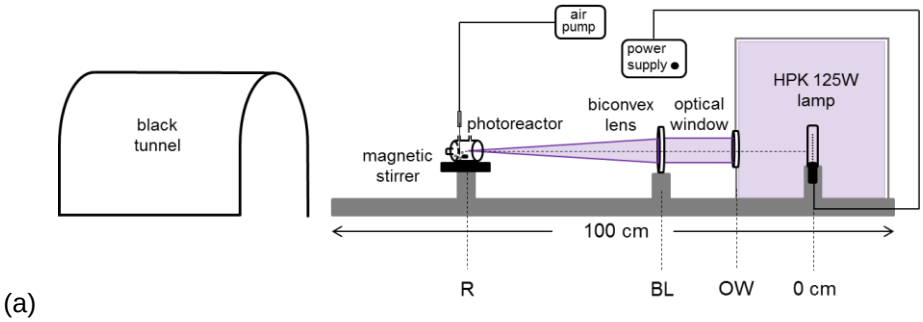

(a)

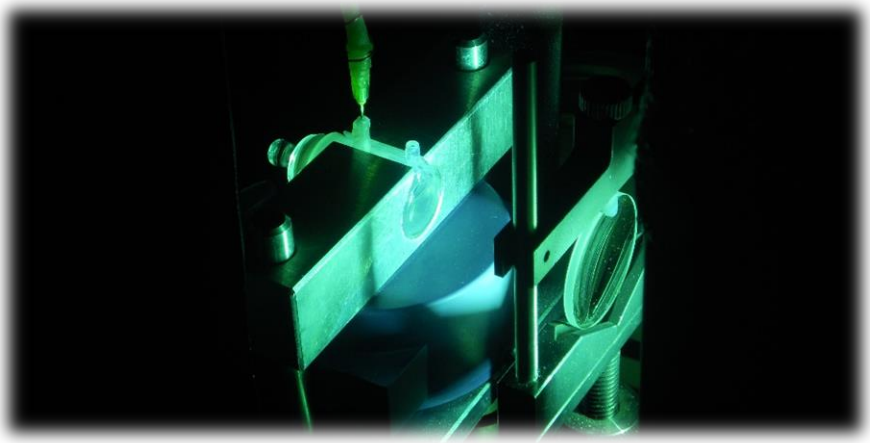

(b)

Figure 7.2 – Cylindrical reactor with HPK125W lamp setup scheme (a) and picture (b).

The effect of the biconvex lens and long pass filters was also evaluated as accessories to create different optical conditions for the assessment of new photocatalysts activity. Photocatalytic results on caffeine degradation did corroborate what was expected given the optical characterization results. Comparison with the system used in Chapter 6 for the same cylindrical photo-reactor was made and the results are shown and commented in Appendix B.2.

7.1.2 Optical characterization

7.1.2.1 Variation on the light spectrum with the distance to the lamp

By positioning the reactor at different distances from the lamp, the irradiated spectra reaching the inside of the borosilicate reactor through the surface exposed to the light

beam, previously intersected by the optical window, were collected and are represented in Figure 6.1.

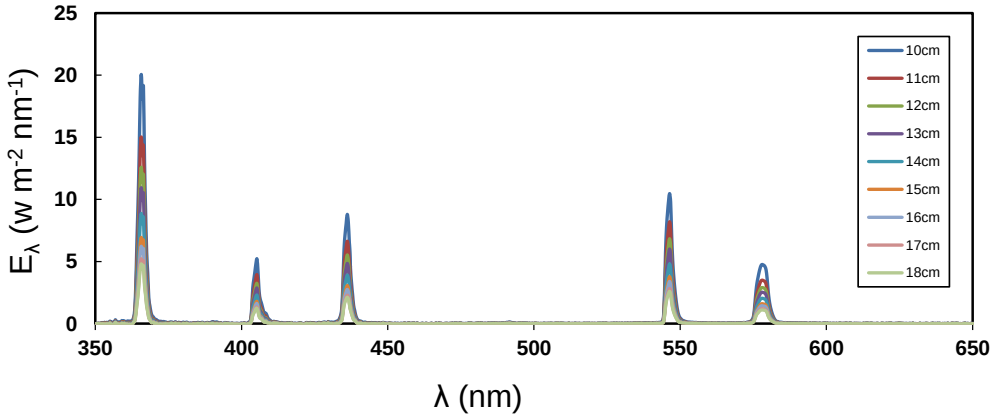

Figure 7.3 – Evolution on the spectral irradiance reaching the inside of the photo-reactor with the distance to the irradiation source.

For wavelengths higher than 350 nm, five main emission lines are observed centred at 365, 405, 436, 546 and a small band centred at 578 nm, resulting from the contribution of the two peaks at 576.9 and 578 nm, accordingly to the information of the supplier (Figure 7.1 a). As expected, the intensity of the emission lines decreases progressively with the distance to the lamp.

The area of the spectrum recorded for each fixed distance was integrated corresponding to the irradiance represented in Figure 7.4. A maximum of 142 W m^{-2} was measured at 10 cm, decreasing inversely with the square distance to the lamp (r^2 = 0.9698) with less representative differences for distances above 15 cm, reaching ca. 35 W m^{-2} at 18 nm.

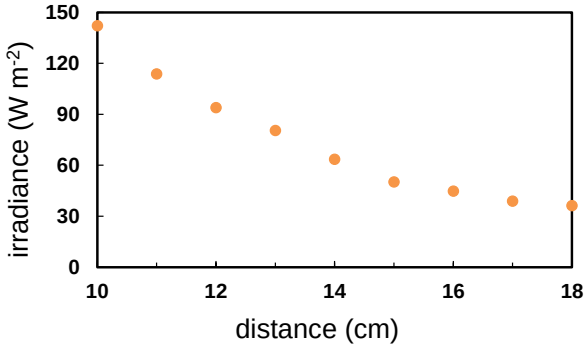

Figure 7.4 – Decay of the irradiance as a function of the distance to the lamp.

Ideal windows allow the optical beams to pass from one environment to another without changing the wavelength distribution, so the contribution of each emission line intensity to the total irradiance was calculated in percentage for each spectrum at a fixed distance and the results are plotted in Figure 7.5.

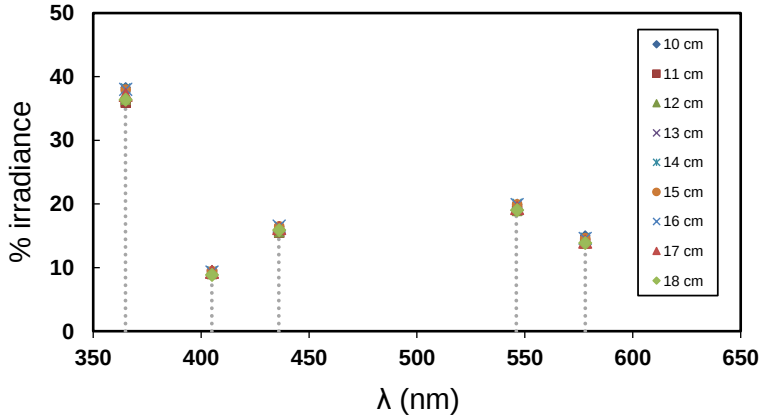

Figure 7.5 – Contribution of the intensity of each particular emission line on the total irradiance for different distances.

In fact, for the presented system, the wavelength distribution is maintained independent of the total irradiance in the range of the measured distances. The highest contribution for the total intensity is given by the line at 365 nm with ca. 40% for the total intensity, working under near-UV to visible light conditions. For the assessment of pure visible light activity of photocatalysts, the line at 365 nm must be totally eliminated with optical filters.

7.1.2.2 Effect of the optical elements on the emitted spectrum

Optical elements are of great importance to manage the irradiating light in order to simulate the required conditions to be studied in photocatalytic reactions. Working at a fixed distance from the lamp requires focusing the light beam in the surface of interest that is the exposed face of the borosilicate reactor. For that purpose, a biconvex lens, which has the property of converging the incident light with a positive focal length, has been introduced. This lens has great optical transmittance, higher than 90% for wavelengths upper than 350 nm and a positive focal distance of 20 cm.

As previously mentioned, the study of visible active photocatalysts requires the management of the optical conditions to obtain a light beam reaching the reactor with

wavelengths greater than 400 nm. Two long pass filters (LP) were used to create these conditions and the optical transmittance of both is represented in Figure 7.6.

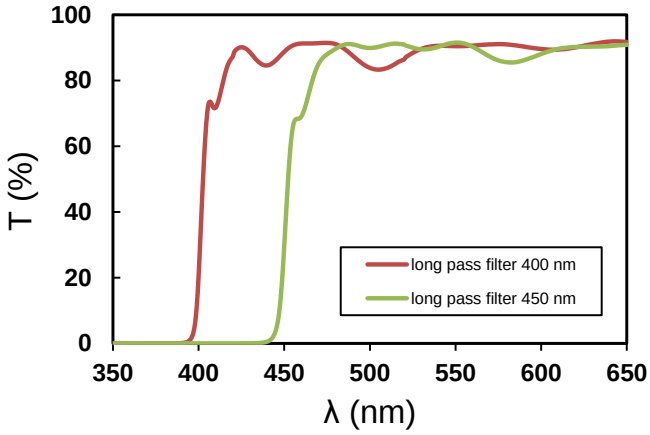

Figure 7.6 – UV-Vis transmittance of long pass filters.

The long pass filter at 400 nm cuts the emission line at 365 nm and using the long pass filter at 450 nm only 546 and 578 nm emission lines will be used in photocatalytic reactions. With these optical accessories adequate conditions are created to test visible light active catalysts.

To confirm the expected working conditions in photocatalytic experiments, the light spectra reaching the inside of the borosilicate reactor, fixed and centred at 17 cm from the irradiating source when the light beam is intersected by the different optical elements, were collected and are represented in Figure 6.2. To mention the different tested configurations an abbreviated form will be used hereafter, as an example, OW_BL_LP400_R stands for the light beam being intersected by the optical window, followed by the biconvex lens and the long pass filter for 400 nm with the photo-reactor (R) centred at a fixed distance with reference to the lamp. The BL was fixed just next to the optical window to avoid light dispersion, focusing the light beam, and the optical filters were disposed right in front of the BL followed by the photocatalytic reactor which was centred at a distance of 17 cm to the lamp.

The presence of the optical window (OW_R) slightly reduces de intensity of the emitted spectrum reaching the inside of the photo-reactor (R). Conversely, the effect of the BL (OW_BL_R) clearly increases the absolute irradiance which is the result of being focusing the light beam over the photo-reactor volume.

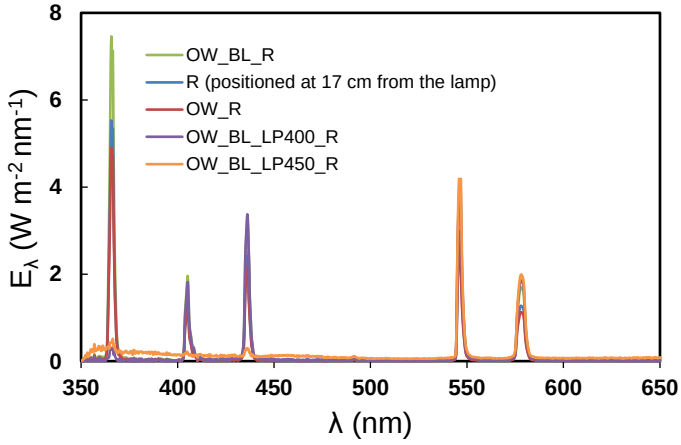

Figure 7.7 – Effect of the different optical elements on the light spectra reaching the inside of the photo-reactor
(OW – optical window, BL – biconvex lens, LP – long pass filters, R – photo-reactor).

The configuration here represented by the OW_R curve corresponds to the one in light pink in Figure 6.1 for the distance of 17 cm. As expected, the line at 365 and those at 405 and 436 nm are blocked when the filter of 400 or 450 nm are used, respectively.

Given the advantages on using the BL which focus the light beam on a given surface area therefore maximizing the irradiance at a fixed position located inside the focal distance, the configuration in use hereafter is OW_BL_R. The contribution of each peak for the total irradiance of the spectrum obtained with this configuration is in accordance with the results obtained for the spectra recorded without the biconvex lens represented in Figure 7.5, confirming that this optical element does not affect the wavelength distribution of the original light beam.

7.1.3 Photocatalytic experiments

Preliminary photocatalytic experiments were performed with the benchmark P25 in powder form over 7 mL of 20 mg L^{-1} caffeine solutions. Except for the experiments of catalyst load optimization, the concentration in use was of 1.0 g L^{-1}. The experimental results were discussed based on the pseudo-first order kinetic constant, *k,* obtained by non-linear regression fitting to the experimental data. Degradation profiles were expressed in caffeine concentration (C) normalized to the initial concentration C_0 (C/C_0). Marquardt-Levenberg algorithm was used to seek the values of the parameters that minimize the sum of the squared differences between observed and predicted values of the dependent variable (tolerance 1 x 10^{-10}). Standard error of

estimated *k* and the respective regression coefficient of the model (r^2) are shown in Table 7.1 and Table 7.2 indicating in general good fitting of the model to the experimental data.

7.1.3.1 Effect of the optical elements on the photocatalytic activity of P25 over caffeine solutions

The modification on the emitted light spectrum with optical accessories was described in the previous Section 7.1.2.2 and is now evaluated through experimental results on caffeine degradation. In Figure 7.8 are represented the degradation profiles for different configurations with the optical elements biconvex lens and the long pass filter for 400 nm. For the placement of the long pass filters after the biconvex lens, the closest position for the reactor with reference to the lamp is centred at 17 cm. In order to have comparable results, all the reactions were performed with the reactor fixed at this position.

Accordingly to what was expected, the usage of the long pass filter LP400 nullifies the photo-activity of the benchmark P25, since the drawback of these bare TiO_2 catalysts resides on the absence of visible light absorption, which is the major fraction of sun light reaching the earth's surface, of relevance for real photocatalytic applications at industrial scale. Hereupon, the described system is adequate to identify potential industrial catalysts with pure visible light response.

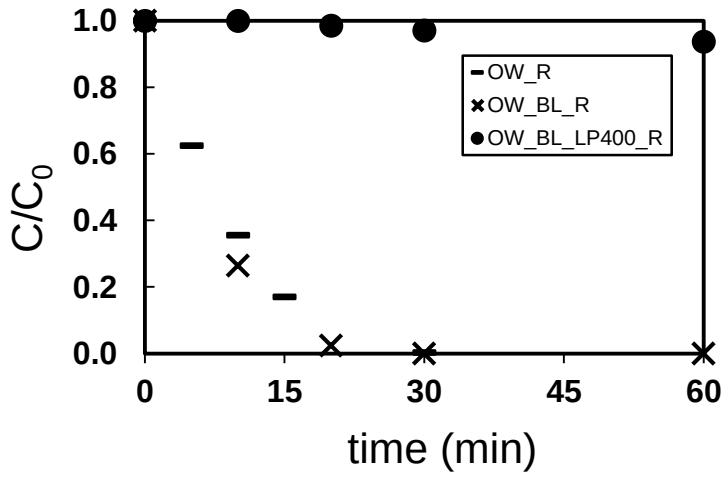

Figure 7.8 – Effect of the optical accessories on the photocatalytic activity of P25 suspensions for caffeine degradation.

Regarding the effect of the biconvex lens, an increase on the measured absolute irradiance of ca. 67%, from 39 to 65 W m^{-2}, resulted in a raise of 32% in photocatalytic activity for the configuration using the biconvex lens (from k = 0.107 ± 0.006 min^{-1} for OW_R to k = 0.141 ± 0.008 min^{-1} for OW_BL_R configuration), which means that at the described conditions the photon flux is not a limiting step, as not all the irradiated photons are being used in the photocatalytic process. The usage of a non-optimized catalyst load can be one of the reasons for the incapacity on the generation of more oxidative radicals in proportion with the photons fed to the system so the study of this parameter is needed to proceed with future photocatalytic experiments.

7.1.3.2 Optimization of the P25 powder catalyst load on the degradation of aqueous caffeine

The optimum catalyst dosage to be used on slurry photocatalytic reactions depends always on the geometry and working conditions of each photo-reactor, ranging normally within 0.2 to 2.5 g L^{-1} for TiO_2 in slurry batch reactors [1, 9, 10]. In a true heterogeneous catalytic regime the initial rates of reaction are found to be directly proportional to the mass of catalyst until reach a certain limit above which they start to become independent on the catalyst load. For higher amounts of catalyst the screening effect, due to particles in excess, masks part of photosensitive surface decreasing the penetration depth of light. Optimal catalyst load is then defined as the maximum mass of catalyst in which all the particles are totally illuminated, ensuring total absorption of efficient photons [11].

As crucial parameter to establish optimized operating conditions, the catalyst load of P25 suspensions was studied in a range of 0.05 to 2.0 g L^{-1} on caffeine degradation of 20 ppm solutions with an initial volume of 7 mL during 30 min of irradiation in a configuration of OW_BL_R, the reactor positioned at 17 cm. The obtained results are gathered in Figure 7.9 and resumed in Table 7.1 in terms of the pseudo first order kinetic constants.

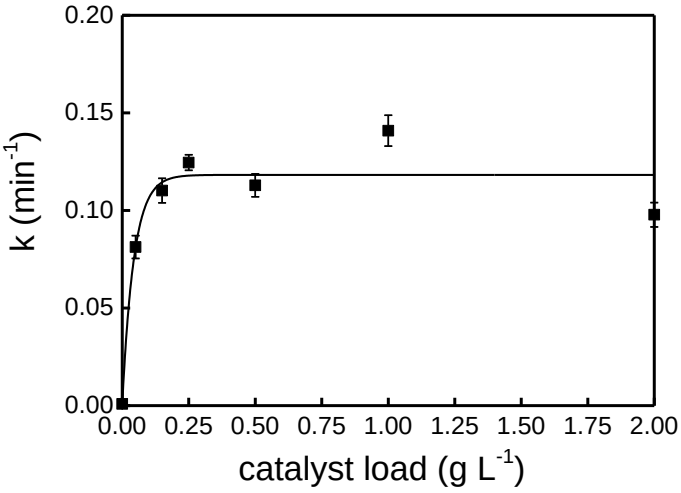

Figure 7.9 – Pseudo-first order kinetic constant of caffeine photo-degradation for different catalyst loads of P25 suspensions.

For catalyst loads bellow 0.25 g L^{-1} the kinetic constant increased progressively with the amount of catalyst in suspension. As the amount of catalyst increases in suspension above 0.50 g L^{-1}, the kinetic constant oscillates around 0.124 min^{-1} reached at 0.25 g L^{-1}.

Table 7.1 – Pseudo-first order kinetic constants (*k*) and respective standard errors for the photolytic and photocatalytic degradation of caffeine using different catalyst loads of P25. The regression coefficients (r^2) are also presented.

Catalyst load (g L^{-1})	*k* (10^{-2} min^{-1})	r^2
0.00 (photolysis)	0.896 ± 0.007	0.950
0.05	8.13 ± 0.59	0.986
0.15	11.0 ± 0.6	0.993
0.25	12.4 ± 0.4	0.998
0.5	11.3 ± 0.6	0.994
1.00	14.1 ± 0.8	0.997
2.00	9.78 ± 0.62	0.990

Since the highest photocatalytic activity was observed for a catalyst load of 1.0 g L^{-1}, this was the load considered for further experiments, the same used as default in the

previous studies. The fall of the kinetic constant for a load of 2.0 g L^{-1} may be eventually ascribed to the abovementioned screening effects.

7.1.3.3 Optimization of the reactor position relative to the biconvex lens

As previously mentioned, irradiance decreases inversely with the square of the distance from the light source and in order to have the highest amount of photons irradiating the photo-reactor it was supposed to place it the nearest as possible to the lamp. It is reported in literature that the reaction rate is directly proportional to the radiant flux, confirming the participation of the photo induced electrons and holes in the reaction mechanism. However, above a certain limit the reaction rate starts to be proportional to the square root of the radiant flux [5, 9-11]. It is remarked that optimal light power utilization corresponds to the domain where the reaction rate is proportional to the radiant flux. Above that limit the rate of electron-hole formation becomes greater than the photocatalytic rate, which favors the electron-hole recombination. The usage of the optical lens was proven to increase the system photocatalytic efficiency, as discussed in the previous Section 7.1.3.1, by focusing the light beam over the photo-reactor leading to a more efficiency on photons absorption. Thus, reactor position was optimized in relation to the distance with the biconvex lens, as illustrated in Figure 7.10. Maximum usage of the light photon flux also depends on ensuring irradiation over the entire photo-reactor volume for maximum catalyst photo-activity.

Different possibilities of positioning the photocatalytic reactor inside the focal distance of the biconvex lens are represented in Figure 7.10. Given the dimensions of the biconvex lens of 4 cm in diameter and knowing the focal distance as being positive 20 cm, at 10 cm from the biconvex lens the light beam is focused in a surface with 2 cm in diameter which overlaps with the round section of the photocatalytic reactor exposed to the light beam. The length of the cylindrical reactor is of 3.5 cm, as shown in Figure 2.4 a in Section 2.2.2 of Chapter 2.

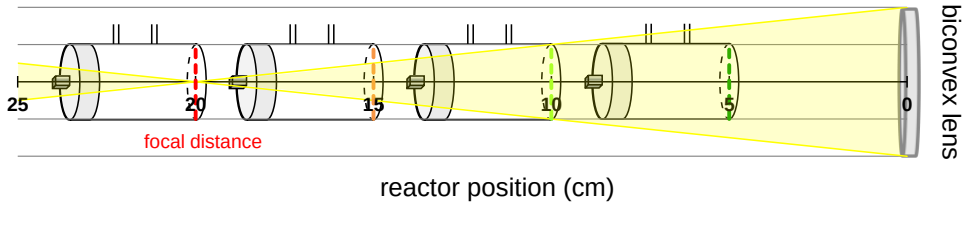

Figure 7.10 – Schematic representation of the incidence of the light beam on the photocatalytic reactor at different distances from the biconvex lens.

As represented, the reactor volume is fully irradiated when the exposed face is placed at 5 cm from the biconvex lens. For longer distances, the fraction is progressively lower being minimum when the reactor is placed between 15 and 25 cm from the biconvex lens. For a higher yield of the irradiated light on photocatalytic reactions, it is expected that the conditions are attained with a configuration where the reactor is positioned between a distance of 5 and 10 cm from the biconvex lens to ensure irradiation over the whole reactor volume and minimize the light fraction which is not focused on the reactor, as happens for closer distances.

Photocatalytic experiments were performed at different configurations with the reactor exposed face positioned at 5, 6.5, 10, 15 and 20 cm from the biconvex lens. A catalyst load of 1.0 g L^{-1} was used in an initial volume of 7 mL of 20 mg L^{-1} caffeine suspensions irradiated during 30 min in a configuration of OW_BL_R, varying the reactor position with relation to the biconvex lens. The obtained results are represented in terms of the pseudo-first order kinetic constant *k* in Figure 7.11 and the discrete values are resumed in Table 7.2. A configuration of OW_BL_R with the reactor fixed at distances lower than 5 cm was not possible to run due to physical limitations on the approximation of the biconvex lens and the reactor holders.

The irradiated spectra reaching the inside of the photocatalytic reactor for the different configurations studied were collected and the absolute irradiance is represented together in Figure 7.11 and also gathered in Table 7.2.

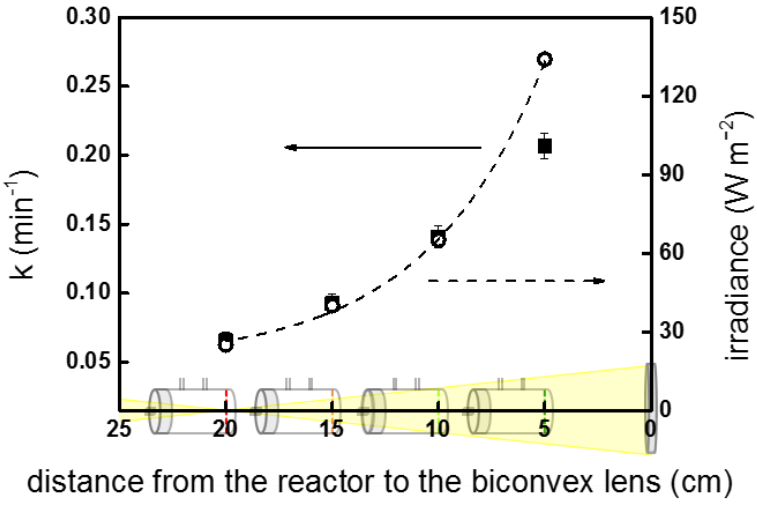

Figure 7.11 – Decay of the kinetic constant on caffeine degradation with the distance from the photo-reactor to the biconvex lens (black squares: pseudo-first order kinetic constants – left axis; open circles: absolute irradiance – right axis).

As expected, the photo-efficiency of the catalyst decayed with the distance to the biconvex lens, and at a distance of 5 cm the kinetic constant is the maximum (0.207 min^{-1}), decreasing almost 70% (0.066 min^{-1}) for a distance of 20 cm.

Table 7.2 – Pseudo-first order kinetic constants (*k*) and respective standard errors for the photocatalytic degradation of caffeine using P25 suspensions with the reactor positioned at different distances from the biconvex lens. Regression coefficients (r^2) and the absolute irradiance for each configuration is also presented.

Distance to the BL (cm)	*k* (10^{-2} min^{-1})	r^2	Irradiance (W m^{-2})
5	20.7 ± 0.9	0.997	134
6.5	16.0 ± 1.4	0.988	105
10	14.1 ± 0.8	0.997	65
15	9.26 ± 0.68	0.987	40
20	6.57 ± 0.58	0.978	25

In the range of 10 to 20 cm distance, there is proportionality between the absolute irradiance and the kinetic constant, as the experimental points are overlapped in Figure 7.11. However, for closer distances the raise in the absolute irradiance is higher than the gain on the photo-activity of the catalyst. This behaviour reflects that at these conditions not all the photons irradiated over the photocatalyst in the solution are consumed for the production of oxidative radicals. An intermediate position of 6.5 cm ensuring irradiation over the total inner volume of the reactor for maximum photo-activity was also tested in order to set the point from which there is no more proportionality and the results are gathered in Table 7.2. However, at these conditions there is a portion of light which is still irradiated outside the reactor volume and so the proportionality is no longer verified, as the experimental points for the absolute irradiance and the respective kinetic constant did not overlap (not represented).

The optimum light power utilization is defined in the domain where these parameters follow a proportionality [9, 11], which is observed in the range of 10 and 20 cm from the biconvex lens with maximum photocatalyst activity for closer distances. For the new setup and the studied conditions, the optimized reactor position is considered to be at a fixed distance of 10 cm from the exposed reactor face to the biconvex lens (corresponding to a distance of the reactor centred at 17 cm from the lamp) with maximum photo-activity and minimizing the amount of photons which are not used in the photocatalytic system. This configuration allows for the use of the optical filters

intersecting the light beam between the bifocal lens and the photo-reactor, so experimental data in the presence or in the absence of the filters can be comparable if the optimum HPK_OW_BL_R@17cm configuration is used.

7.2 Conclusions

The assembling and validation of a new setup was succeeded to improve some drawbacks identified in the photocatalytic system used in the previous Chapter 6 with the same cylindrical reactor, mainly regarding the efficiency on light usage for photocatalytic studies due to an inadequacy of the dimensions between the lamp and the photo-reactor. The arc of the HPK125W lamp is on scale with the small cylindrical photocatalytic reactor and is enclosed in an aluminum box to allow stabilizing the lamp intensity during the dark phase while adsorption-desorption equilibrium is established or to create cycles of illuminated and dark periods during reaction. An optical window separates the environment of the lamp from the photocatalytic reactor, without changes on the emitted beam regarding wavelength distribution. Optical accessories can be incorporated at very well defined settings and the light beam focused on the photo-reactor using a biconvex lens in the wavelength range of interest by using optical filters.

The absolute irradiance decreases inversely with the square of distance with the highest contribution from the line at 365 nm with ca. 40% for the total intensity, working under near-UV to visible light conditions. A long pass filter at 400 nm cuts the emission line at 365 nm and visible light conditions can be created to test visible active catalysts. The use of the biconvex lens maximizes the light irradiance over a given surface area fixed inside the focal distance and therefore a configuration of type HPK_OW_BL_R was set for the photocatalytic experiments, corresponding to the light intersected by the optical window immediately followed by the biconvex lens and with the photo-reactor positioned at a fixed distance.

Results on the photo-degradation of a caffeine solution with powder P25 in suspensions showed a raise in 32% of the photo-activity in terms of the kinetic constant for an increase on the absolute irradiance of ca. 67% when using the biconvex lens. The activity of P25 catalyst was nullified with the application of the long pass filter at 400 nm in a configuration of HPK_OW_BL_LP400_R since bare TiO_2 materials are not photocatalytically active under visible light conditions.

Within the focal distance of the biconvex lens, the position of the reactor with relation to this optical accessory was adjusted for optimal light power utilization, which is defined in the domain where the absolute irradiance and the photo-activity, here in terms of the kinetic constant, follow proportionality. At the studied conditions, the optimal reactor position with relation to the biconvex lens was found to be with the exposed reactor face at a fixed distance of 10 cm, corresponding to have the photocatalytic reactor centred at 17 cm from the lamp, represented by the configuration HPK_OW_BL_R@17cm. These settings come out with maximum photo-activity minimizing the amount of photons which are not used in the photocatalytic mechanism. This configuration also allows the use of the optical filters placed between the biconvex lens and the photocatalytic reactor so comparable results can be obtained for the optimized conditions.

By simulating similar irradiance conditions in a specific configuration, the new system was compared with the previous one described in Section 2.2.2 of Chapter 2 through the photocatalytic degradation of a caffeine solution with P25 deposited in the form of film and the results were in conformity.

The developed setup is available to study photocatalytic degradation in aqueous systems either with suspensions or with supported catalysts under different irradiating conditions with optimized usage of the emitted light.

7.3 Experimental section

A high-pressure mercury vapour lamp HPK125W (Heraeus Noblelight) was used. The transmittance of the borosilicate reactor reaches ca. 90% for $\lambda > 340$ nm, with a cut-off of the main UV bands lower than 300 nm. An optical window with reference 210-1403 (EKSPLA) is used to allow the beam radiation to pass from the inside of the aluminium box where the lamp is placed to the outside environment avoiding external interferences and with high optical transmittance. For an optimized use of the beam energy, making up for the light scattering outside the aluminium box, a biconvex lens with reference 111-1418 (EKSPLA) is placed before the small cylindrical reactor to converge the beam into the surface area of interest for the photocatalytic process (see Figure 7.2 in Section 7.1.1). Long pass optical filters are also available to provide conditions of visible light for wavelengths higher than 400 nm or 450 nm (LP400 or LP450) with reference 64-697 and 64-698 (Edmund Optics), respectively, which are of interest to discriminate pure visible active catalysts as a

good industrial promise for real applications under solar conditions. Light transmittance of the optic accessories was recorded by UV-vis spectroscopy.

The commercial benchmark TiO_2 powder from Evonik Degussa Corporation (P25) consisting in a mixture of rutile and anatase phases, also tested in Chapter 6, was used in preliminary photocatalytic experiments using this new setup.

7.3.1 Assessment of the irradiated spectra

The light spectra were collected with a UV-vis spectroradiometer USB2000+ (OceanOptics, USA). It is important to note that when the data is collected a permanent oscillation is observed due to the properties of a light beam so the recorded data is affected by the unavoidable wave effect. Though it can be balanced by adjusting the acquisition time and scans to average parameters on the acquiring moment, for a representative average of the absolute irradiance. In comparison considerations, small differences must be however discussed given the inherent abovementioned wave effect. Excepting when particular conditions are mentioned, all the spectra were collected in the presence of the optical window. At the time of acquisition the optical fiber was centered inside the photo-reactor.

7.3.2 Photocatalytic experiments

Caffeine photo-degradation experiments were conducted either over catalyst powder suspensions or in supported films in a small cylindrical borosilicate reactor irradiated by a high-pressure mercury vapor lamp HPK125, following the experimental procedure described in Appendix B.1.

For suspensions, the catalyst load was optimized for a caffeine solution (20 mg L^{-1}) initial volume of 7 mL, with concentrations between 0.05 and 2.0 g L^{-1}. The solution was saturated in air during reaction to provide oxygen molecules involved in the photocatalytic mechanism. Preliminary tests were conducted to establish the period of dark absorption, which is sufficient with 15 min since no adsorption was observed at the defined concentrations. The same period of time is needed to reach a constant irradiance from the lamp and at this moment the optical window is opened (see Figure 7.2 in Section 7.1.1) and the reactor starts to be irradiated ($t = 0$; $C = C_0$). An experiment in the absence of catalyst was also performed as blank in order to calculate the contribution from direct photolysis which is practically null. Reactions with supported catalysts in the form of films deposited in thin glass slides were also

performed at similar irradiating conditions to those referred in Chapter 6 with the immersion lamp TQ150.

Samples were periodically withdrawn, centrifuged and analyzed by High Performance Liquid Chromatography (HPLC) with a mobile phase consisting on ultra-pure water and methanol. Caffeine concentration was determined at the maximum absorption wavelength (274 nm). This absorbance was found to be linear over the whole considered range (a maximum relative standard deviation of 2%).

7.4 References

[1] Kowalska E, Rau S. Photoreactors for Wastewater Treatment: A Review. Recent Pat Engin. 2010; 4 (3):242-66.

[2] Chong MN, Jin B, Chow CWK, Saint C. Recent developments in photocatalytic water treatment technology: A review. Water Res. 2010; 44 (10):2997-3027.

[3] Ray AK, Beenackers AACM. Development of a new photocatalytic reactor for water purification. Catal Today. 1998; 40 (1):73-83.

[4] Van Gerven T, Mul G, Moulijn J, Stankiewicz A. A review of intensification of photocatalytic processes. Chem Eng Process. 2007; 46 (9 SPEC. ISS.):781-9.

[5] Gogate PR, Pandit AB. A review of imperative technologies for wastewater treatment I: Oxidation technologies at ambient conditions. Adv Environ Res. 2004; 8 (3-4):501-51.

[6] Bosc F, Ayral A, Albouy P-A, Guizard C. A Simple Route for Low-Temperature Synthesis of Mesoporous and Nanocrystalline Anatase Thin Films. Chem Mater. 2003; 15 (12):2463-8.

[7] Dionysiou DD, Burbano AA, Suidan MT, Baudin I, Laîné J-M. Effect of Oxygen in a Thin-Film Rotating Disk Photocatalytic Reactor. Environ Sci Technol. 2002; 36 (17):3834-43.

[8] Langlet M, Kim A, Audier M, Guillard C, Herrmann JM. Transparent photocatalytic films deposited on polymer substrates from sol–gel processed titania sols. Thin Solid Films. 2003; 429 (1–2):13-21.

[9] Herrmann JM. Heterogeneous photocatalysis: state of the art and present applications In honor of Pr. R.L. Burwell Jr. (1912–2003), Former Head of Ipatieff

Laboratories, Northwestern University, Evanston (Ill). Top Catal. 2005; 34 (1-4):49-65.

[10] Thakur RS, Chaudhary R, Singh C. Fundamentals and applications of the photocatalytic treatment for the removal of industrial organic pollutants and effects of operational parameters: A review. J Renew Sustain Energy. 2010; 2 (4):042701.

[11] Herrmann J-M. Heterogeneous photocatalysis: fundamentals and applications to the removal of various types of aqueous pollutants. Catal Today. 1999; 53 (1):115-29.

Part VI

Final conclusions and future work

8 Final conclusions

Given the lack on visible light absorbance by pure TiO_2 photocatalysts, the incorporation of a carbon phase was performed using different carbon nanotubes which were pre-treated with nitric acid for the creation of oxygen functionalities to improve the mixing quality between the semiconductor and the carbon materials. Photocatalytic tests were performed on the degradation of aqueous caffeine using different types of TiO_2 powders and the respective composites synthesized by a simple hydration-dehydration methodology. A clear synergy was observed when using a particular commercial TiO_2 catalyst from Sigma-Aldrich and functionalized MWCNTs with a composite photo-activity overcoming the one attained with the benchmark P25 when supported in glass slides and used in the photocatalytic experiments in the form of films. A customized photocatalytic setup was developed to perform photocatalytic studies with an optimal usage of the emitted light by using different optical accessories at very well defined settings in suspensions or supported catalysts applications. The main conclusions drawn based on the overall experimental data are here summarized.

8.1 SWCNTs functionalization by hydrothermal oxidation

The surface chemistry of SWCNTs was finely tailored by a HNO_3 hydrothermal method and the degree of oxygen functionalization correlated with HNO_3 concentration through a mathematical function, either for the total amount of groups released as CO and CO_2 or even for each particular oxygen functionality, after deconvolution of the TPD-MS recorded spectra. The obtained mathematical functions allow the prediction of the functionalization degree for each material at fixed HNO_3 concentrations. Operating temperature and HNO_3 concentration were identified as the key parameters in the modification of the surface chemistry, suggesting that the activation energy is controlling the functionalization process.

For the rapid assessment of the amount on high acidic carboxylic groups, which are of particular interest on the synthesis of composites with TiO_2 materials for photocatalytic applications, water vapor adsorption-desorption was also applied and the results correlated with those obtained with TPD-MS.

Raman spectroscopy on the functionalized SWCNTs reveals linear proportionality of the defect-activated Raman mode intensity with the amount of surface groups determined by TPD-MS and water adsorption-desorption measurements, allowing quantitative correlations of the Raman results with the functionalization process. Formation of amorphous carbon, which depends on the aggressiveness of the oxidative conditions, was identified through water adsorption-desorption and Raman measurements on thermally treated SWCNTs samples in air and argon atmosphere. It was however concluded that a large fraction of the carboxylic groups formed upon acidification remains attached on the SWCNTs surface rather than on the generated carbonaceous fragments.

Porosity modifications were related with the aggressiveness of the oxidation conditions in a way that the mesopore volume, originated from the packing of the nanotube bundles, correlates inversely with the acidity of the treatment solution. The micropore volume, corresponding to the interstitial space between individual nanotubes, is shifted toward lower sizes. Both phenomena unveil more efficient packing/organization of the nanotube bundles and of individual CNTs with the introduction of oxygen functional groups.

Functionalization of SWCNTs can be effectively controlled and quantified and the optimum conditions defined in relation to the desired physicochemical properties and pore structure characteristics for specific applications.

8.2 MWCNTs functionalization by hydrothermal oxidation

The significantly lower costs for mass production of MWCNTs and the predictably higher resistance for the post effects of oxidation treatments were the motivation to reproduce the study of the controlled functionalization through hydrothermal HNO_3 oxidation over two types of commercially available materials grown by catalytic chemical vapor deposition with largely different morphological characteristics (diameter and length). As observed in the previous study for SWCNTs, the hydrothermal treatment results in the progressive introduction of oxygen functionalities on MWCNTs surface correlated mathematically with the HNO_3 concentration. Oxygen functionalities concentration and thermal stability was found to be determined by morphologic characteristics of the CNTs, namely diameter and length, as well as by the crystallinity and purity of the pristine materials.

With increasing HNO_3 concentration, Raman spectroscopy showed a progressive narrowing and reduction on the intensity of the defect activated MWCNTs Raman bands, as result of the oxidation of the external carbon layers through hydrothermal treatment. On the contrary, higher amounts of amorphous carbon were identified for the MWCNTs treated under boiling acidic conditions, while producing comparable amounts of oxygen functionalities consuming higher amounts of the oxidizing agent.

Pore structure analysis revealed different modifications depending on the morphologic characteristics of the MWCNTs. For the short and thin tubes, a more efficient packing and reorganization of the tube's bundles resulted in a shift of the mean pore size from the macro to the mesopore area, at variance with what happened for the longer and thicker tubes where a small increase of the total pore volume was the more pronounced effect.

In a comparable analysis over SWCNTs and MWCNTs studies with different morphologies oxidized through hydrothermal and boiling HNO_3 conditions, it was possible to conclude that diameter and length do dictate the degree of surface functionalization over CNTs, with higher stability and favored generation of carboxylic acids for MWCNTs, in particular for smaller and thinner tubes. Hydrothermal oxidation is a consistent and reliable methodology for CNTs pre-treatment when precise surface requirements are known and needed for specific applications. However, boiling acid oxidation is conducted at much lower temperatures than those required for the creation of comparable amounts of oxygen functionalities with hydrothermal treatment, at which the carboxylic groups starts to release, thus ensuring the effective attachment of higher amounts of these groups which are of

interest for further synthesis of CNT composite materials to be applied on photocatalytic studies.

8.3 TiO_2/CNT composites for photocatalytic degradation of caffeine aqueous solutions

After having selected the type of CNTs and the adequate pre-treatment to further prepare photocatalytic composites with enhanced activity in the near-UV to visible region of the spectrum, three different types of TiO_2 powders were used in photo-degradation studies, one synthesized by a modified sol-gel method (SG) and two commercial others obtained from Evonik Degussa Corporation (P25) and Sigma-Aldrich (SA), in combination with MWCNTs functionalized through the nitric acid boiling oxidation using a simple hydration-dehydration preparation method.

The surface area of TiO_2 materials was increased after the inclusion of the carbon phase, in proportion with the CNTs loading and especially in the case of composites prepared with functionalized CNTs, based on N_2 adsorption isotherms calculations. Electron microscopy clarified the difference on the interaction between phases, being very weak in the case of SG based composites with an observed segregation of phases with big TiO_2 agglomerates. Good distribution of TiO_2 particles along the walls of the CNTs was registered in the case of P25 and SA based composites, in particular a developed interaction was shown for composites with the bigger SA nanoparticles around which the CNTs were seen to be rolled up.

Despite the highest activity in caffeine photo-degradation observed for bare P25 catalyst, SA was the one which really took benefit with the addition of the carbon phase, in accordance with characterization results, especially when functionalized CNTs were used increasing its photo-efficiency progressively with the load of CNTs. In fact, the photocatalytic mechanism seems to undergo a different pathway when SA based catalysts are used in caffeine degradation with free radicals produced by photoexcited electrons determining the highest activity for SA/CNTf-20, at variance with a reaction mechanism governed by the generated holes in the case of all other P25 and SG based catalysts.

With the motivation of seeking for a potential catalyst on visible applications at industrial scale, the activity of catalysts in film form deposited on thin glass slides was compared for P25 and the SA/CNTf-20 catalysts, with a ca. 50% higher photo-activity for the latter in comparison to the benchmark P25. Further studies on the degradation

of methylene blue also confirmed the highest activity of SA/CNTf-20 composite film with relation to the one of bare P25.

Raman spectroscopic complementary studies showed however that there was no evidence of a real interphase for the composites prepared using the hydration-dehydration methodology and that the photocatalytic results were simply correlated with the quality of mixing between the semiconductor and the carbon phases, which dictated the need to test composites prepared through other methodologies. Sol-gel synthesis of TiO_2 based composites including the carbon phase previously functionalized during the ageing of the sol with a more consistent interphase did show higher photo-activity than the benchmark P25 in the form of films for methylene photo-degradation.

The obtained results showed promising routes to develop potential photocatalysts to be applied at industrial scale in the form of films overcoming the customary lead of the well-known P25 on the list of photocatalysts.

8.4 Assembling and validation of a customized photocatalytic system for water remediation studies using caffeine as model compound

In the final stage of this work a new assembling was set to perform photocatalytic studies and validated through optical characterization and with the first results on caffeine degradation with the benchmark P25 catalyst in powder or film form. The new photocatalytic system was developed with the purpose of improving some of the lacks identified in the system where the first results were obtained (Chapter 6), in particular the inefficient usage of the light due to inadequate dimensions of the arc of the immersion lamp in comparison with those of the photocatalytic reactor.

A high pressure mercury vapour lamp with five main emission lines between 350 and 600 nm, with an arc in scale with the small cylindrical reactor, was enclosed inside an aluminum box in an environment separated from the photo-reactor, communicated through an optical window with high transmittance and no appreciable changes on the emitted beam regarding wavelength distribution. A small window on the aluminum box itself allows alternating between illuminated and dark cycles with the intensity lamp perfectly stabilized due to having explicit separated environments.

The light beam can be directly focused on the reactor exposed surface in a specific wavelength range of interest for the photocatalytic studies through the incorporation of optical accessories like a biconvex lens and optical filters at very well defined

settings. The configuration on photocatalytic experiments was set as using the biconvex lens positioned immediately next to the optical window since its effect maximizes the intensity of the emitted lines, raising in 32% the photo-activity of powder P25 on caffeine degradation in comparison with a configuration with no use of the biconvex lens. The application of the long pass filter at 400 nm nullified the activity of bare P25, so the conditions are created to finely discriminate truly visible active photocatalysts.

Optimum catalyst load was found to be 1.0 g L^{-1} and the reactor position was set to work at 10 cm from the biconvex lens corresponding to a configuration with the photo-reactor centred at 17 cm from the irradiation source. The criterion was based on the proportionality between the variation in absolute irradiance and the photo-activity, which implies optimal light power utilization, ensuring maximum photo-activity and minimizing the amount of photons which are not used in the photocatalytic mechanism.

The assembling of this customized setup allows performing photocatalytic studies in aqueous systems using powdered or immobilized catalysts with optimized usage of the emitted light, having the possibility of varying different parameters with accuracy and evaluating their effects in the activity of the synthesized materials.

9 Future Work

Suggestions to progress on this line of investigations are here presented based on the conclusions drawn through the overall work presented in this document, on the experience of the research group where the work was developed and on other reported scientific studies already published in related literature.

9.1 Surface modification of CNTs

In the present work, liquid phase HNO_3 oxidation was chosen as functionalization methodology to include oxygen functionalities on the surface of the CNTs because it requires simple means to be carried out resulting in a satisfactory density of surface groups. Other oxidants can be explored both in liquid and gas phase for different acidic strength conditions and find the most adequate treatment to each particular morphology of the CNTs in use, either SWCNTs or MWCNTs with variable diameters and lengths. Liquid oxidants commonly tested are HNO_3, H_2SO_4, H_2O_2 and in some cases are used in combination of more than one single oxidant, as is the case of piranha solutions consisting in a mixture of H_2SO_4 and H_2O_2 with high acidic strength. Oxygen functionalization of CNTs in gas phase has the advantage of no residual acid wastes and can be performed under flow of HNO_3 vapour, O_2 or O_3 and even enhanced through UV irradiation.

Criterion to choose the most adequate functionalization method and respective conditions must lay on the creation of the surface groups of interest with high thermal stability and minimum amounts of amorphous carbon at the nanotubes surface, in accordance to the previously discussed characterization results over treated CNTs through TPD-MS, Raman spectroscopy and thermal analysis.

9.2 TiO_2/CNT composites with visible response on photocatalytic water treatment studies

Promising results were achieved with SA/CNTf-20 composite films showing highest performance than those prepared with the benchmark P25 in oxidative photo-degradation of different organics under near-UV to visible irradiation. Though, Raman investigations unveil the lack on a real electronic interphase between the semiconductor and the carbon phases for composites prepared through the applied hydration-dehydration method. Further investigations should be developed on the composite synthesis aiming the creation of an effective interphase evidenced by Raman characterization.

Preparation methods involving the inclusion of the carbon phase during the formation of the TiO_2 matrix and concomitant functionalization of the CNTs could improve the creation of an intimate electronic interphase with enhanced photo-activity in the visible region. A first approach was anticipated in the group with the preparation of TiO_2/CNT composites through a modified sol-gel method in acidic media and the

results overcame those abovementioned obtained with the SA/CNTf-20 composite, showing that this procedure is a good starting point to begin with. Different parameters with presumable influence on the quality of the prepared composites can be studied like the temperature and time of ageing and calcination.

As concluded during the progress of this work, namely for the hydrothermal functionalization method, the successful creation of oxygen functionalities on the CNTs surface is clearly activated by temperature. An improved methodology is here proposed involving the concomitant CNTs functionalization and TiO_2 lattice formation through a hydrothermal process in acidic media to be carried out in an autoclave with controlled temperature and pressure conditions. Different TiO_2 precursors and oxidants can be explored, either liquid or gaseous agents, in a broad range of temperatures and pressures. Other similar carbon phases can also be studied like graphene oxide which has already shown good photocatalytic results in combination with TiO_2 for visible light response.

Given the exponential functions found to correlate the amount of oxygen surface groups with the concentration of HNO_3, for the hydrothermal functionalization method presented in this work, the photo-activity of the composites prepared through the here suggested hydrothermal method should be checked for an analogue correlation with the oxidant concentration.

After selected a composite with a good interphase between TiO_2 and the carbon phase, the catalyst should be tested in powder and film form under both UV and visible irradiation and compared with the reference benchmark P25 in the oxidative photo-degradation of different single organic molecules, mixtures to mimic real effluents an in an advanced phase for industrial effluents remediation with representative pollutants concentrations.

9.3 Customized photocatalytic setup

The assembling and validation of a customized photocatalytic system for water remediation studies at laboratory scale was accomplished. Powdered or immobilized catalysts developed towards visible response, to make up for the low fraction of UV light at the earth's surface, can be further tested in this system using long pass filters ensuring visible light conditions with an optimization usage of the light beam. Further investigations on the catalyst activity and stability are suggested to be performed in continuous mode. The solution to be treated can be continuously pumped from a

reservoir placed outside the black tunnel which covers the photo-reactor while illuminated. Reutilization of the supported catalysts should be experienced seeking for the lifetime of the catalyst and the release of catalyst particles into the solution, which can be monitored through UV-Vis spectroscopy. Mechanical resistance of the catalyst films is also an important issue on the sequence of these investigation.

In the case of particular studies requiring monochromatic irradiance, for instance when monitoring the concentration of a particular organic within a mixture is needed, bandpass filters can be applied. In fact, photo-degradation of mixtures and real effluents are expected to be carried out in this new customized system.

Appendix

Appendix A. MWCNTs functionalization by hydrothermal oxidation

Appendix A.1 Identification and quantification of oxygen groups for NC3100 MWCNTs

In Figure A.1 are represented the deconvolution curves for each oxygen group created at the surface of NC3100 after hydrothermal oxidation, which results are commented in Section 5.1.1 of Chapter 5.

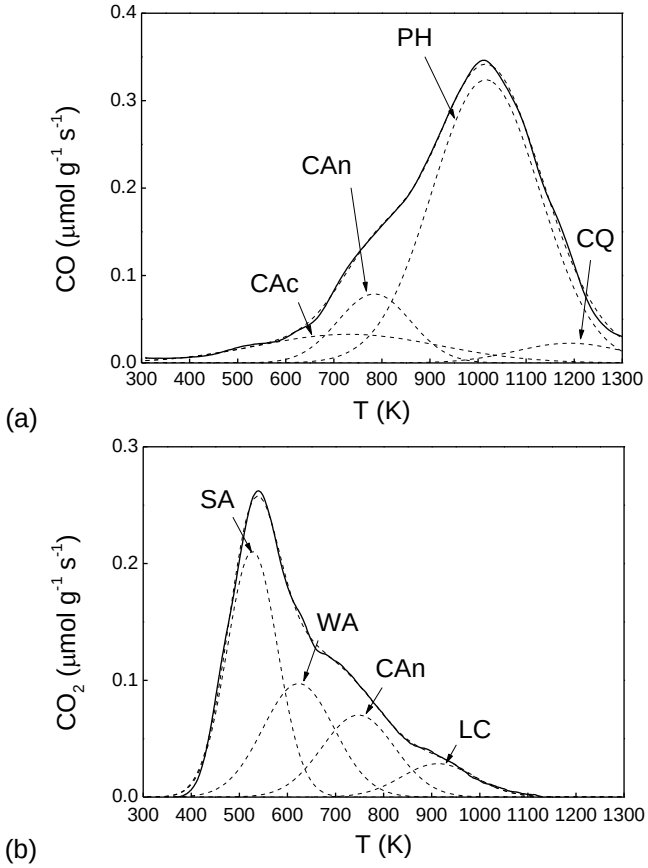

Figure A.1 - Deconvolution of TPD spectra for NC3100 treated with [HNO_3] = 7.0 mol L^{-1} at boiling temperature: groups released as (a) CO and (b) CO_2 (PH - phenols; CAn - carboxylic anhydrides; CQ - carbonyl quinones; LC - lactones; CAc - carboxylic acids; SA - strong acidic CAc; WA - weakly acidic CAc).

Appendix A.2 Raman spectroscopy analysis of the oxidizing effects on MWCNTs microstructure

Deconvolution through multi-peak fitting analysis of the Raman spectra at 514 nm is shown in Figure A.2 for the acid treated NTX3 MWCNTs in comparison with their pristine analogues. Comments on these results are included in Section 5.1.3 of Chapter 5.

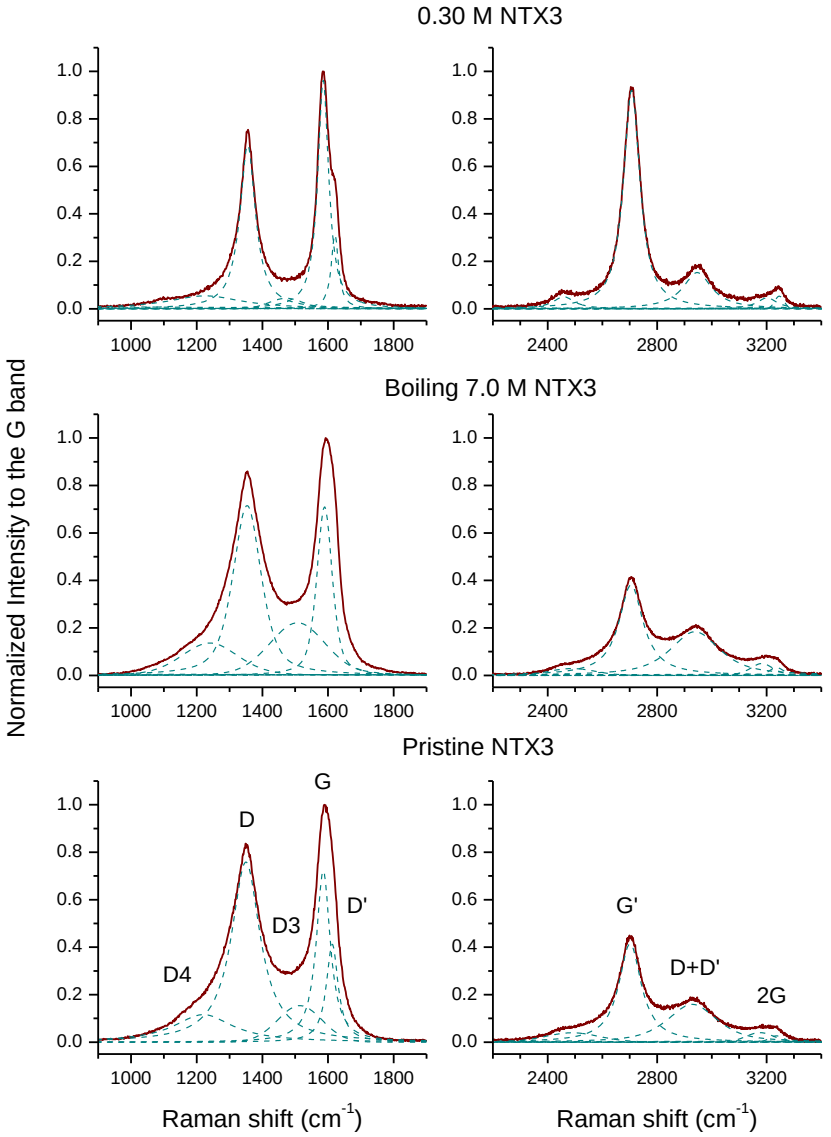

Figure A.2 - Multi-peak fitting analysis of the Raman spectra for the hydrothermally (0.30 mol L^{-1}) and boiling (7.0 mol L^{-1}) acid treated NTX3 MWCNTs in comparison with the pristine samples at 514.5 nm.

Thin NC3100 MWCNTs hydrothermally functionalized with [HNO_3] = 0.30 mol L^{-1} and further exposed to isothermal oxidation in air at different temperatures show the following Raman spectra represented in Figure A.3, which are analysed in Section 5.1.3 of Chapter 5.

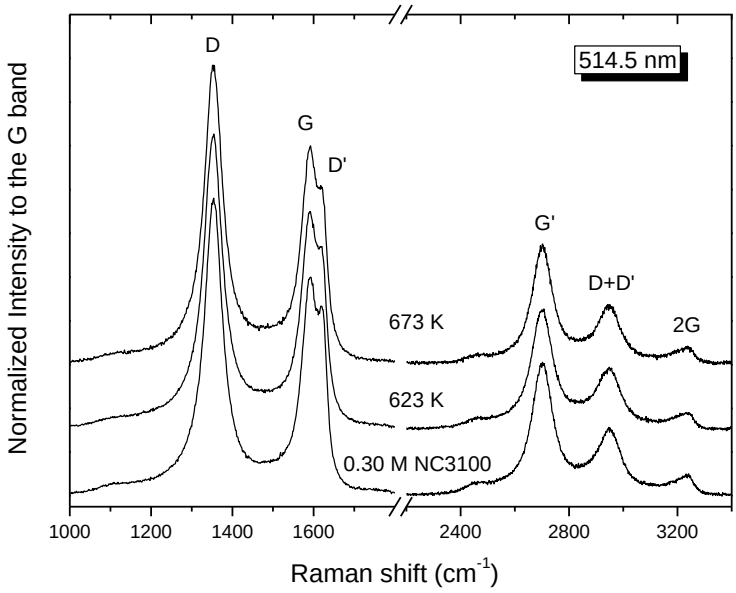

Figure A.3 - Raman spectra of the hydrothermally functionalized NC3100 MWCNTs at [HNO_3] = 0.30 mol L^{-1} after isothermal oxidation at 623 and 673 K.

Appendix B. Assembling and validation of a customized photocatalytic system for water remediation studies using caffeine as model compound

Appendix B.1 User manual for the customized photocatalytic setup

In a typical experiment, the user should follow the suggested experimental procedure to perform photocatalytic oxidative degradation of organic pollutants in aqueous solutions using powdered or immobilized catalysts:

1. Prepare the solution of the organic to be degraded in a volumetric flask.

2. Place the catalyst powder and the magnetic bar inside the cylindrical reactor. In case of catalyst films, use the tweezers to place the thin glass slide in the bottom of the reactor cover with the surface where the catalyst was deposited on turned upside and fix it with a Viton® O-ring. Close the reactor after grease the glass cover and seal it with Parafilm®.

3. Fill the reactor with 7 mL of the organic solution using a syringe and close the top opening near the cover with Parafilm®.

4. Place the reactor centered on its support over the magnetic stirrer with the cover in the opposite side of the lamp, according to what is represented in Figure 7.2.

5. Insert the needle connected to the air pump, after being plugged on, in the top opening previously closed with Parafilm® to feed the solution with O_2.

6. Turn on the magnetic stirrer set in a level to prevent bubbling outside the sampling opening. The air flow is regulated for 200 cm^3 min^{-1} but it can be further tuned with a Hoffman clamp to avoid throwing liquid outside the photo-reactor. In case of powder catalysts, regulating the speed of stirring must ensure a stable suspension.

7. Start counting the time for the dark phase (adsorption time should be determined for each catalyst and organic pollutant, typically 15 or 30 min).

8. The lamp should be turned on by pulsing the button in the power supply (outside the aluminum box) 10 minutes before ending the dark phase to get the intensity stabilized. The fume hood should be working every time the lamp is turned on avoiding accumulation of O_3 generation.

9. To block the light beam from reaching users eyes and skin, lean the black tunnel on the aluminum box.

10. After completed the dark phase, take the first sample by displacing the black tunnel, which corresponds to the initial concentration after adsorption (C_0), used on conversion calculations.

11. Open the window of the aluminum box to start irradiating the reactor and start to count the time for the photocatalytic reaction regime.

12. Using the glasses for UV protection, take samples regularly by the free top opening of the reactor. After sampling, always lean on back the black tunnel on the aluminum box to avoid injuries caused by the emitted radiation.

13. At the end of the reaction time, close the window of the aluminum box and switch off the lamp by pulsing the button in the power supply. The fume hood must be working for at least 10 minutes more to eliminate the ozone produced during the lamp operating.

14. Turn off the stirring and take off the syringe of the air feed. Unplug the air pump.

15. Open the reactor carefully and clean the grinding of the cover with a paper embedded in acetone to remove the grease. In case of requiring the powder catalyst recovering, use a paper filter to separate it from the solution. In case of the film catalysts, use the tweezers to remove the thin glass slide after taking off the Viton® O-ring. Dry the catalysts overnight at 110 ºC before storing.

16. Clean the photo-reactor with distilled water.

NOTES

N0. Do not get directly exposed to the HPK125W lamp. The lamp should only be switched on inside the aluminum box placed inside the fume hood and light exposure through the optical window should be always carried out using protection glasses.

N1. The set up should always be fixed with the four elements aligned: the photo-reactor, the biconvex lens or other optical accessories and the optical window in relation to the arc of the lamp (see Figure 7.2).

N2. Cover the top of the aluminum box with a perforated aluminum foil for light protection and allow the dissipated heat produced by the lamp to be released.

N3. Samples should have to be withdrawn more regularly during the first period of the photocatalytic reaction to provide more information about the kinetic profile for a better further fitting to mathematic models.

N4. If samples are powder suspensions centrifugation is required to HPLC or UV-Vis spectrophotometry analysis. The sampling volume should be no more than 700 µL if centrifugation is required, for catalyst suspensions, and no more than 600 µL if operating with catalyst films. Maximum of 5 samples are recommended.

N5. The placement of the biconvex lens was set just leaned on the aluminum box next to the optical window, through which the light beam is irradiated, for focusing the beam over the photo-reactor minimizing the loose of energy by light scattering. Studies were performed to set the position of the photo-reactor and the configuration was optimized to be centered at a distance of 17 cm from the lamp. The distance at which the reactor is placed always refers to be measured from the center of the reactor to the center of the lamp arc. The placement of every optical accessory should be considered with reference to the irradiation source, defined as fixed at 0 cm (see Figure 7.2), and mentioned as e.g. HPK_OW_BL_R@17 cm for the optimized configuration. At the referred conditions, the irradiance reaching the inside of the photo-reactor is ca. 65 W m^{-2}.

Appendix B.2 Comparison of photocatalytic results at similar irradiance conditions obtained with TQ and HPK lamps

To compare the photocatalytic systems with TQ and HPK lamps and the small cylindrical reactor, caffeine degradation with the benchmark P25 supported in glass slides was performed in the new system, at the same conditions described in Section 6.1.2.4 of Chapter 6. To mimic the absolute irradiance at which the reaction occurred spectral conditions were compared. At the same distance from the irradiation source, the absolute irradiance recorded for HPK is always higher than that of the TQ lamp, as shown in Figure B.1. However, in the new setup, due to the housing of the lamp in a separated environment inside the aluminium box (see Section 7.1.1 on Chapter 7), the placement of the reactor cannot be done at the same distance that was performed with the TQ lamp. The closest position for the photo-reactor in the new system is at 12 cm from the lamp and, as shown in Figure B.1, the irradiance for that conditions is ca. 90 W m^{-2}. Therefore the biconvex lens was used to make up for the difference in the irradiance.

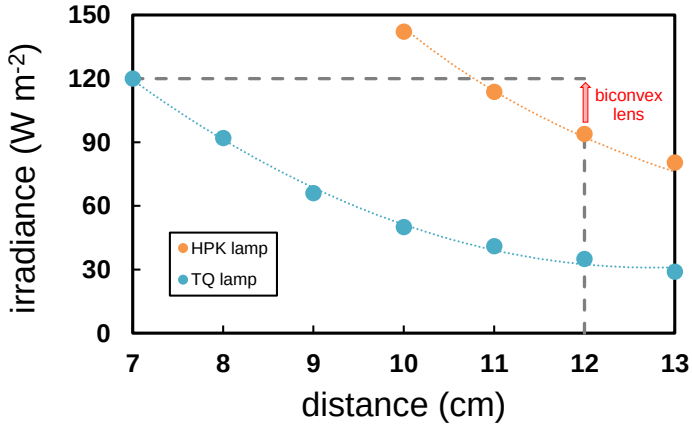

Figure B.1 – Irradiance for TQ and HPK lamps varying with the distance.

The configuration of OW_BL_R@12cm was found to have a spectrum comparable to that obtained with the TQ lamp for the experimental conditions at which the reaction was performed in Chapter 6, corresponding to a distance from the photo-reactor to

the lamp of 7 cm. Both spectra are represented in Figure B.2 with an irradiance around the mean value of 125 ± 10 W m^{-2}.

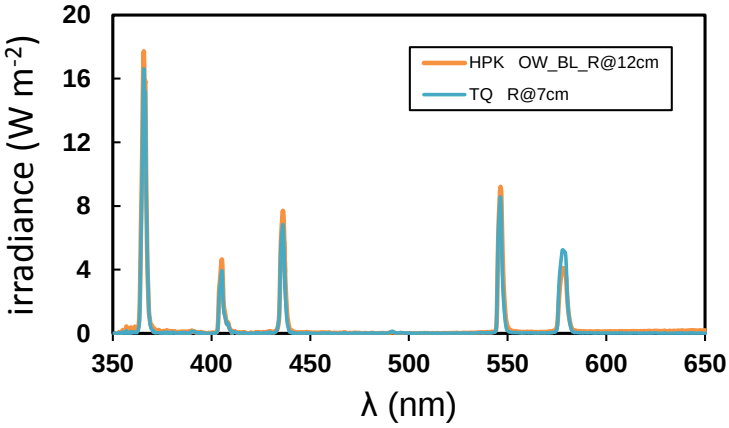

Figure B.2 – HPK and TQ spectra with a similar irradiance.

Photocatalytic degradation of caffeine over a P25 film was then performed in the new system with an OW_BL_R@12cm configuration for the same conditions of C_0 = 50 mg L^{-1} irradiated during 180 min and the results are plotted in Figure B.3.

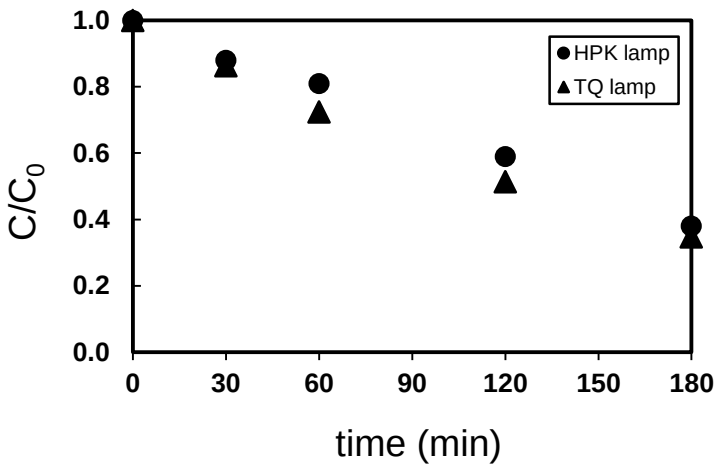

Figure B.3 – Caffeine degradation profiles using P25 films irradiated with TQ and HPK lamps.

In fact, photo-degradation profiles are comparable for the same irradiance conditions. The new system has the advantage of using a lamp with an appropriate scale for the

small photocatalytic reactor, housed in a closed box with an optical window which separates the environment of the lamp from the reactor without affecting the emitted beam on wavelength distribution. The lamp intensity can be then stabilized inside the box with the window closed and create dark and illuminated cycles by opening or closing the optical window allowing the reactor to be in dark or irradiated conditions. Different optical accessories can be incorporated at very well defined settings to optimize the incidence of the light beam in the photocatalytic reactor with the spectral ranges required for the objectives of each particular study.

List of Publications

Papers in international scientific periodicals with referees

Likodimos, V., Steriotis, T.A., Papageorgiou , S.K., Romanos, G. E., **Marques, R.R.N.**, Rocha, R.P., Faria, J.L., Pereira, M.F.R., Figueiredo, J.L., Silva, A.M.T., Falaras, P. Controlled surface functionalization of multiwall carbon nanotubes by HNO_3 hydrothermal oxidation. Carbon 69 (2014) 311.

Sampaio, M.J., **Marques, R.R.N.**, Tavares, P.B., Faria, J.L., Silva, A.M.T., Silva, C.G. Tailoring the properties of immobilized titanium dioxide/carbon nanotube composites for photocatalytic water treatment. Journal of Environmental Chemical Engineering 1 (2013) 945.

Miranda, S.M., Romanos, G.Em., Likodimos, V., **Marques, R.R.N.**, Favvas, E.P., Katsaros, F.K., Stefanopoulos, K.L., Vilar, V.J.P., Faria, J.L., Falaras, P., Silva, A.M.T. Pore structure, interface properties and photocatalytic efficiency of hydration/dehydration derived TiO_2/CNT composites. Applied Catalysis B: Environmental 147 (2014) 65.

Marques, R.R.N., Carrapiço, P.M., Dražić, G., Silva, C.G., Faria, J.L., Silva, A.M.T. Photocatalytic degradation of caffeine: Developing solutions for emerging pollutants. Catalysis Today 209 (2013) 108.

Silva, C.G., Monteiro, J., **Marques, R.R.N.**, Silva, A.M.T., Martínez, C., Canle L., M. and Faria, J.L. Photochemical and photocatalytic degradation of *trans*-resveratrol. Photochemical and Photobiological Sciences 12 (2013) 638.

Romanos, G.E., Likodimos, V., **Marques, R.R.N.**, Steriotis, T.A., Papageorgiou, S.K., Faria, J.L., Figueiredo, J.L., Silva, A.M.T., Falaras, P. Controlling and Quantifying Oxygen Functionalities on Hydrothermally and Thermally Treated Single-Wall Carbon Nanotubes. The Journal of Physical Chemistry C 115 (2011) 8534.

Sampaio, M.J., Silva, C.G., **Marques, R.R.N.**, Silva, A.M.T., Faria, J.L. Carbon nanotube-TiO_2 thin films for photocatalytic applications. Catalysis Today 161 (2011) 91.

Marques, R.R.N., Machado, B.F., Faria, J.L., Silva, A.M.T. Controlled generation of oxygen functionalities on the surface of single-walled carbon nanotubes by HNO_3 hydrothermal oxidation. Carbon 48 (2010) 1515.